

Image Analysis and Machine Learning Techniques for Digital Histopathological Images

by

Salah Mohammed Awad AL-Heejawi

A thesis submitted in partial fulfillment of the requirements for the degree of

Doctor of Philosophy

in

Digital Signal and Image Processing

Department of Electrical and Computer Engineering  
University of Alberta

© Salah Mohammed Awad AL-Heejawi, 2021

## **Abstract**

The histopathological examination of tissue biopsies is used as the gold standard by pathologists for diagnosing skin cancers, such as melanoma. Traditionally, the histopathological slides are examined by clinicians under a microscope. With recent advances in digital imaging and scanning, a glass slide biopsy can now be digitized at high magnifications to create a high resolution digital whole slide image (WSI), which facilitates pathologists for disease identification by analyzing a WSI image on a computer monitor. However, the amount of data produced by a whole slide digital scanner, which can exceed billions of pixels for a WSI, manual analysis of an image can take significant amount of time. More importantly, the manual analysis by clinicians is typically subjective and often prone to intra- and inter-observer variability. The main goal of this dissertation is to develop image analysis and machine learning algorithms that can aid towards building a Computer-Aided Image Analysis (CAIA) system for digital skin histopathological images. These systems would automatically extract meaningful features from the WSI and perform classification and grading to help pathologists to obtain prompt and accurate diagnosis.

In this dissertation, we propose four CAIA systems to grade and detect melanoma based on histopathological image analysis. The proliferative index is a useful indicator for cancer grading. First, a technique is proposed for efficient segmentation of the lymph nodes in a lymph node WSI (obtained using stains such as H&E, MART-1, and Ki-67) and estimates the rate of cell growth by detecting the actively proliferative nuclei using classical machine learning techniques. Secondly, a novel Convolutional Neural Network (CNN) architecture is developed for efficient segmentation of nuclei regions and a seed detection technique to accurately detect the number of nuclei. These two techniques together can be used to obtain an accurate estimation of the proliferation index. Thirdly, a CAIA system is proposed where the nuclei are segmented using a CNN architecture,

and a hand-crafted feature-based technique is used to detect the melanoma nuclei on H&E-stained lymph node WSIs. Finally, a CNN-based technique is proposed for automated detection of the melanoma regions on H&E-stained skin histopathological images. Experimental results show significant performance improvement in the detection and grading of melanoma over state-of-the-art techniques.

## Preface

- Chapter 3 of this thesis has been published as {Salah Alheejawi, Hongming Xu, Richard Berendt, Naresh Jha, and Mrinal Mandal, “Novel lymph node segmentation and proliferation index measurement for skin melanoma biopsy images” Computerized Medical Imaging and Graphics, Volume 73, Pages 19-29, 2019}. I was responsible for the experiment design, implementation, signal processing, data collection and analysis, and manuscript composition. Hongming Xu helped in the implementation process. Dr. Richard Berendt, and Dr. Naresh Jha provided the medical data used in the manuscript, ground truth results and medicine specific expertise. Prof. Mrinal Mandal was the supervisory author and was involved with concept formation and manuscript composition. This chapter proposes an automated technique to segment the lymph node regions on histopathological images obtained with various stains such as H&E, MART-1, S-100, CD-45 and Ki-67. The technique then determines the melanoma regions on a Ki-67-stained image to calculate the proliferation index. A few Regions of Interests with high PI values for grading by the pathologists.
- Chapter 4 of this thesis has been accepted in Computerized Medical Imaging and Graphics Journal as {Salah Alheejawi, Richard Berendt, Naresh Jha, Santi Maiti, and Mrinal Mandal, “Automated Proliferation Index Calculation for Skin Melanoma Biopsy Images using Machine Learning”, Computerized Medical Imaging and Graphics (accepted), 2021}. I was responsible for the experiment design and implementation, signal processing, data collection, and manuscript composition. Dr. Richard Berendt, and Dr. Naresh Jha provided the medical data used in the manuscript, ground truth results and medicine specific expertise. Prof. Santi Maiti helped in the implementation process. Prof. Mrinal Mandal was the supervisory author and was involved with concept formation and manuscript composition. This chapter proposes an automated technique to calculate the Proliferative index values inside the tumor regions using a CNN based algorithm. An efficient CNN architecture was proposed to segment the nuclei.
- Chapter 5 of this thesis has been published as {Salah Alheejawi, Richard Berendt, Naresh Jha and Mrinal Mandal, “Melanoma Cell Detection in Lymph Nodes Histopathological Images using Deep Learning”, Signal & Image Processing: An International Journal (SIPIJ) Vol.11, No.4, August 2020}. I was responsible for the experiment design, implementation, signal processing, data collection and analysis, and manuscript composition. Dr. Richard Berendt, and Dr. Naresh Jha provided the medical data used in the manuscript, ground truth results and



medicine specific expertise. Prof. Mrinal Mandal was the supervisory author and was involved with concept formation and manuscript composition. This chapter proposes a technique to segment the nuclei on H&E-stained lymph node image and classify the nuclei into melanoma and non-melanoma nuclei.

- Chapter 6 of this thesis has been submitted to a Journal and is currently under review. I was responsible for the experiment design, implementation, signal processing, data collection and analysis, and manuscript composition. Dr. Richard Berendt, and Dr. Naresh Jha provided the medical data used in the manuscript, ground truth results and medicine specific expertise. Prof. Mrinal Mandal was the supervisory author and was involved with concept formation and manuscript composition. This chapter proposes an automated technique to detect the melanoma regions on H&E-stained skin histopathological images. The technique uses an efficient CNN architecture for nuclei segmentation followed by a module to detect the malignant melanoma regions.

The medical data used in the thesis work is collected from the Cross Cancer Institute, University of Alberta, Edmonton, Canada in accordance with the protocol for the examination of specimens with skin melanoma. The approval of this study was granted by the Health Research Ethics Board of Alberta (HREBA) - Cancer Committee (Ethics ID: HERBA.CC-14-0088\_REN6).

*“This thesis is dedicated to the memory of my father  
Mohamed Awad Alheejwai”*

## **Acknowledgements**

I would like to express my sincere gratitude to my supervisor, Prof. Mrinal Mandal for his continuous support, encouragement, and guidance throughout my graduate studies. All my achievements have benefited from his knowledge, and inspiration. It would not have been possible to write this thesis without his help. These years which I have been under their supervision will be remembered as one of my “life honor”.

I am deeply indebted to Dr. Richard Berendt and Dr. Naresh Jha who have been my research collaborator during the past five years, for their valuable guidance and suggestions during our collaborative research. I learned and gained enormously from their knowledge and experience. I would also like to thank the members of my defense committee, for taking their precious time to review my thesis and giving valuable suggestions for my research. I am deeply grateful to my supervisory committee members: Dr. Jie Han, and Dr. Mahdi Tavakoli, who provided valuable suggestions and comments during the course of my PhD. I would also like to thank Dr. Edmond Lou and Dr. Khan Wahid for examining my thesis.

I would also like to thank the Ministry of Higher Education and Scientific Research (MOHESR), Iraq, for awarding me the scholarship to support my study at University of Alberta. Much respect to my labmates, classmates, and friends. Dr. Huiquan Wang, Mr. Raju Machupalli, Dr. Ameera Mohamad Awad, Dr. Kareem Salloomi, Ms. Sanaa Al-Sumaidae, Ms. Lina Liu, and Dr. Hongming Xu and many others. They made my days meaningful and happy. The years I have spent at the University of Alberta is an unforgettable period of learning and working experience.

Heartiest thanks to my sisters, and thanks to my brothers Ahmed and Haider. Last but far from the least, my heartiest love and thanks to my parents, thank you for your tremendous love, devotion and encouragement throughout my life, for which mere words cannot express my gratitude.

# Contents

Abstract .....	ii
Preface .....	iv
Acknowledgements .....	vii
Contents.....	viii
List of Tables .....	xi
List of Figures .....	xii
Abbreviations .....	xix
<b>1. Introduction .....</b>	<b>1</b>
1.1. Skin Cancer and Diagnosis .....	1
1.2. Histopathology Imaging .....	2
1.3. Melanoma Diagnosis and Grading in Skin .....	4
1.3.1. Skin Structure .....	5
1.3.2. Histopathological Examination for Skin Tissue .....	6
1.4. Melanoma Diagnosis and Grading in Lymph Node .....	6
1.4.1. Lymph node Structure .....	6
1.4.2. Histopathological Examination for Lymph Node Tissue .....	7
1.5. Problem Statements and Motivation .....	7
1.6. Organization of the Thesis .....	9
<b>2. Literature Review .....</b>	<b>10</b>
2.1. Generic Automated CAIs in Histopathology .....	10
2.1.1. Segmentation and ROIs Detections .....	11
2.1.2. Features Extractions .....	12
2.1.3. Classification .....	14
2.1.4. Performance Evaluation Metrics .....	15
2.2. Existing Grading CAIs in histopathological images .....	15
<b>3. Novel lymph Node Segmentation and Proliferation Index Measurement</b>	

<b>for Skin Melanoma Biopsy Images</b>	<b>18</b>
3.1 Introduction	18
3.2 Data Description	21
3.3 Lymph Node Segmentation	21
3.3.1. Coarse Segmentation	21
3.3.2. Features Extraction	23
3.3.3. Fine Segmentation	28
3.3.4. Segmentation Performance	29
3.4 Proliferation Index Calculation	31
3.4.1. Melanoma Mapping	31
3.4.2. Thresholding	35
3.4.3. SVM Classifier	36
3.4.4. PI Calculation	37
3.4.5. Performance Evaluation	39
3.5 Conclusions	41
<b>4. Automated Proliferation Index Calculation for Skin Melanoma Biopsy Images using Machine Learning</b>	<b>42</b>
4.1. Introduction	42
4.2. Data Description	46
4.3. Proposed Technique	46
4.3.1. Tumor Region Identification	47
4.3.2. CNN-based Segmentation	52
4.3.3. CNN Training	52
4.3.4. CNN Configuration	54
4.3.5. PI Calculation	59
4.4. Performance Evaluation	61
4.5. Conclusions	65
<b>5. Melanoma Cell Detection in Lymph Node Histopathological Images Using Deep Learning</b>	<b>66</b>
5.1. Introduction	66

5.2. Data Description .....	68
5.3. Proposed Technique .....	69
5.3.1. CNN-based Nuclei Segmentation .....	69
5.3.2. Nuclei Classification .....	72
5.4. Results and Discussions .....	73
5.4.1. Segmentation Performance .....	74
5.4.2. Classification performance .....	75
5.5. Conclusions .....	78
<b>6. Detection of Malignant Melanoma in H&amp;E-stained Images</b>	
<b>Using Deep Learning Techniques .....</b>	<b>79</b>
6.1. Introduction .....	79
6.2. Data Description .....	82
6.3. Proposed Technique .....	82
6.3.1. CNN-based Nuclei Segmentation .....	83
6.3.2. Melanoma Region Detection .....	85
6.4. Results and Discussions .....	87
6.4.1. Nuclei Segmentation performance .....	87
6.4.2. Melanoma Segmentation performance .....	90
6.5. Conclusions .....	94
<b>7. Conclusions and Future Research Directions .....</b>	<b>95</b>
7.1. Main Contributions .....	95
7.2. Future Research Directions .....	96
<b>References .....</b>	<b>98</b>
<b>Appendix A .....</b>	<b>108</b>
A.1. Dataset used in Chapter 3 .....	108
A.2. Dataset used in Chapter 4 .....	109
A.3. Datasets used in Chapter 5 and Chapter 6 .....	111

# List of Tables

<b>TABLE 3.1.</b>	<b>PERFORMANCE OF THE PROPOSED TECHNIQUE USING DIFFERENT SVM KERNELS.</b>	<b>29</b>
TABLE 3.2.	PI CALCULATION PARAMETERS.	39
TABLE 3.3.	PI CALCULATION PERFORMANCE OF PROPOSED, AND FCM+KM TECHNIQUES.	41
<b>TABLE 4.1.</b>	<b>DETAILS OF THE PROPOSED ARCHITECTURE WITH 19 CONVOLUTIONAL LAYERS. INPUT IMAGE SIZE: <math>H \times W</math> PIXELS (COLOR).</b>	<b>48</b>
TABLE 4.2.	SEGMENTATION PERFORMANCE OF THE PROPOSED TECHNIQUE.	55
TABLE 4.3.	LAYER CONFIGURATION OF THE DEEP LEARNING TECHNIQUES.	63
TABLE 4.4.	SEGMENTATION PERFORMANCE OF THE PROPOSED TECHNIQUE.	63
TABLE 4.5.	COMPARISON OF PI CALCULATION PERFORMANCE.	64
TABLE 4.6.	TRAINING TIME OF CNN MODELS.	65
<b>TABLE 5.1.</b>	<b>DETAILS OF THE NS-NET ARCHITECTURE WITH 5 CONVOLUTIONAL LAYERS. INPUT IMAGE SIZE: <math>M \times N</math> PIXELS (COLOR). NUMBER OF CLASSES: <math>C</math>.</b>	<b>71</b>
TABLE 5.2.	SEGMENTATION PERFORMANCE OF THE DEEP LEARNING ALGORITHMS AND THE CLASSICAL FEATURE-BASED ALGORITHMS.	74
TABLE 5.3.	PROPERTIES OF CNN ARCHITECTURES USED IN PERFORMANCE EVALUATION.	75
TABLE 5.4.	PERFORMANCE OF THE NUCLEI CLASSIFICATION USING DIFFERENT SVM KERNELS.	76
<b>TABLE 6.1.</b>	<b>CELL TYPES AND FEATURES ON SKIN TISSUE DIAGNOSED WITH MELANOMA.</b>	<b>80</b>
TABLE 6.2.	NUCLEI SEGMENTATION PERFORMANCE ON H&E-STAINED IMAGES.	88
TABLE 6.3.	CONFIGURATION OF THE CNN ARCHITECTURES USED IN PERFORMANCE EVALUATION. NOTE THAT PBS-RESNET DOES PATCH-BASED SEGMENTATION DIRECTLY AND DOES NOT PERFORM NUCLEI SEGMENTATION.	88
TABLE 6.4.	MELANOMA SEGMENTATION PERFORMANCE OF VARIOUS STEPS OF THE MRD MODULE.	91
TABLE 6.5.	MELANOMA REGION DETECTION PERFORMANCE.	93

# List of Figures

<b>Figure 1.1.</b>	<b>Invasive melanoma stages.</b>	<b>2</b>
Figure 1.2.	Examples of Histopathological images viewed with different stains	4
Figure 1.3.	The ABCDE criteria for detecting melanoma (Image Credit: [12]).	4
Figure 1.4.	Anatomy of normal skin (Image Credit: [13]).	5
Figure 1.5.	Lymphatic system (a) Anatomy of a lymph node and (b) the lymphatic system in human body.	7
Figure 1.6.	The melanoma research directions. The yellow blocks represent the previous works, and the blue blocks represent the proposed CAIA systems.	8
<b>Figure 2.1.</b>	<b>General framework of a CAD system.</b>	<b>10</b>
Figure 2.2.	Example of a three-layer of ANN.	14
<b>Figure 3.1.</b>	<b>Sentinel Lymph Nodes (SLN) biopsy stained with S-100 stain. The three lymph nodes are shown with green contour.</b>	<b>19</b>
Figure 3.2.	Schematic of the proposed segmentation technique.	21
Figure 3.3.	Histogram smoothing. a) original image histogram. b) smoothed histogram. MN: Melanoma, LN: Lymph node, OT: other tissue and BG: Background.	22
Figure 3.4.	Coarse pixel classification using thresholding. Light blue, yellow, green and dark blue pixels represent <i>Class 1</i> , <i>Class 2</i> , <i>Class 3</i> and <i>Class 4</i> , respectively.	23
Figure 3.5.	Example of classified image, a) lymph node tissue has massive behave within $G_{x,y}$ . b) lymph node tissue has scattered within $G_{x,y}$ .	23



Figure 3.6.	Schematic to calculate the HFM $\mu$ .	25
Figure 3.7.	The HFM $\mu$ for the classified image $\phi$ that is shown in Figure 3.4.	26
Figure 3.8.	Images obtained by applying morphological operations on the image in shown Figure 3.4 (a) $\mu^b$ obtained using Otsu threshold, (b) $\mu_t^{bf}$ obtained after filling the holes, (c) Initial estimate of lymph node $H$ and (d) $L$ after removing small noisy regions.	27
Figure 3.9.	Masks generated from the image in Figure 3.4. (a) Ground truth mask (b) Mask generated by the proposed technique and (c) comparison of ground truth and segmented mask.	28
Figure 3.10.	Lymph node images with different stains (a) S-100, (b) H&E, (c) Ki-67, and (d) MART-1	30
Figure 3.11.	Segmentation performance of the proposed technique for different image. (a) Sensitivity, (b) Precision, (c) Specificity, and (d) Accuracy.	30
Figure 3.12.	Schematic of the proliferation index PI calculation.	31
Figure 3.13.	Image registration for MART-1 and Ki-67-stained images for the same lymph nodes. (a) overlapped masks $\phi_M$ and $\phi_K$ after registration, (b) image $I'_K$ , and (c) image $I''_K$ .	31
Figure 3.14.	Melanoma mapping process (a) Melanoma mask $\delta$ of MART-1, (b) $\delta$ contour melanoma regions (green color) in $I''_K$ image, (c) $\delta$ contour melanoma regions (green color) in $I''_K$ image, (d) The magnified image of yellow square in $\delta$ , (e) $\delta^*$ contour melanoma regions (green color) in $I''_K$ image and (f) The final melanoma mask.	33
Figure 3.15.	The magnified version of melanoma regions in Ki-67 image (obtained from Figure 3.13(f)).	35

Figure 3.16.	Nuclei mask for all melanoma regions using Otsu threshold.	36
Figure 3.17.	Classified nuclei image for all melanoma regions, where yellow and purple represent the active and passive cells respectively.	37
Figure 3.18.	The PI values for each window (in red contour) for melanoma regions.	38
Figure 3.19.	Intermediate results of the proposed technique (a) The Ki-67-stained image (b) Otsu mask, (c) the nuclei mask and (d) the segmentation results using SVM, where the active and passive nuclei are shown in red and blue, respectively.	40
Figure 3.20.	Performance comparison of the proposed Technique (in green bars) and the FCM+KM [19] technique (in yellow bars). The Ground Truth is shown in blue bars.	40
<b>Figure 4.1.</b>	<b>Histopathological image obtained with Ki-67 stain.</b>	<b>43</b>
Figure 4.2.	Schematic of the proposed segmentation technique.	46
Figure 4.3.	Histopathological image of two lymph nodes (a) MART-1-stained image, where melanoma appears in brown color and (b) Ki-67-stained image, where the green contour is the melanoma mask.	47
Figure 4.4.	Proposed CNN architecture for nuclei segmentation (with 19 convolutional layers). Note that there are three paths after Layer I (first convolutional layer). Path A has 8 convolutional (shown in blue), 4 pooling (yellow) and 4 un-pooling (pink) layers. Path B has 9 convolutional layers. Path C is the residual connection from the output of layer I to the concatenate layer. Paths A, B and C meet at the Concatenate Layer.	49
Figure 4.5.	Example of (a) an original RGB Image (704×1280) and (b) the corresponding classified ground truth image, where the active and passive nuclei appear in red and blue color, respectively.	52

Figure 4.6.	Loss and accuracy plots during the network training process.	54
Figure 4.7.	Comparison of the nuclei segmentation performance using paths A+C (i.e., without path B) and paths A+B+C.	56
Figure 4.8.	Segmentation performance evaluation with different number of layers in path B.	56
Figure 4.9.	Performance evaluation with different size of filters in Path B.	57
Figure 4.10.	Example of the feature maps obtained from path B in the proposed CNN. (a) Ki-67 image. (b) ground truth segmented image, (c)-(f) 12 of the 64 feature maps obtained after Layer-B3. (g) Output of Layer-O. (h) Softmax layer output. A: Active nuclei, P: Passive nuclei, and B: Background feature map.	58
Figure 4.11.	Example of PI calculation of ROIs in the three melanoma regions ( $MR_1$ , $MR_2$ , $MR_3$ ) in a WSI. The three melanoma regions in the WSI are shown with magnification. The regions $MR_1$ and $MR_2$ contains three blocks (with red contours) with the highest PI values: 24.14, 22.22, and 22.09. The other five blocks (with black contours) are also active areas, but the PI values are smaller.	60
Figure 4.12.	Magnified window with the highest PI value ( $PI=24.14$ ) in Figure 4.11. (a) input image (b) Detection results with 252 active and 792 passive nuclei. The ground truth $PI=25.15$ with 252 active and 750 passive nuclei.	61
Figure 4.13.	Subjective comparison of segmentation results. (a) Original test image, (b) The ground truth segmentation mask, (c)-(h) Segmentation results for FCM+KM, Otsu+SVM, PI-SegNet, PI-UNet, PI-DeepLab and the proposed technique, respectively.	62

<b>Figure 5.1.</b>	<b>Example of an H&amp;E-stained lymph node tissue image. The lymph node tissue is contoured in black, and malignant melanoma deposits are contoured in green.</b>	<b>67</b>
Figure 5.2.	Schematic of the proposed melanoma detection technique.	69
Figure 5.3.	The proposed NS-Net architecture for nuclei segmentation.	71
Figure 5.4.	Segmentation results. (a) An input image patch (b) the segmented image patch obtained using the NS-Net architecture.	71
Figure 5.5.	Example of HOG feature extraction for a cell nucleus. (a) An image patch with segmented cell nuclei and overlapped gradient orientation. (b) Blown-up of image of two nuclei (melanoma and other cells). (c) The 1x9 HOGFVn's of the cell nuclei.	73
Figure 5.6.	Subjective comparison of cell nuclei segmentation results (contoured in blue color) (a) original test image, (b)-(f) Segmentation results for Voting+Watershed, gLoG+mRLS, SegNet, U-Net and NS-Net techniques, respectively.	75
Figure 5.7.	Three principal components (PC-1, PC-2, and PC-3) of the 1x54 features.	76
Figure 5.8.	Example of classification results. (a) NS-Net input image, (b) NS-Net segmented output image, (c) Classified image obtained using an SVM classifier, where melanocytes and other cell nuclei are contoured with red and blue colors, respectively.	77
Figure 5.9.	Visual example of nuclei segmentation and classification obtained by the proposed technique). The classified melanoma cells are shown in red color, whereas the non-melanoma cells are shown in blue color.	77
<b>Figure 6.1.</b>	<b>An example of skin tissue image with three regions: epidermis region contoured in green color, whereas melanoma nests and</b>	<b>80</b>

**inflammatory cells are contoured in brown and blue colors, respectively.**

Figure 6.2.	Schematic of the proposed melanoma detection technique.	82
Figure 6.3.	The proposed CNN architecture: INS-Net. Note that the output image presents the melanoma, non-melanoma nuclei, and background in red, blue and white colors, respectively.	84
Figure 6.4.	Example of (a) an Original RGB Image and (b) the corresponding INS-Net (segmented) output. The melanoma nuclei, non-melanoma nuclei, and the background pixels appear in red, blue and white colors, respectively.	85
Figure 6.5.	Example of intermediate output images of the MRD module. Melanoma nuclei mask (a) obtained using the proposed CNN, (b) melanoma nuclei mask (in blue) superimposed on the original H&E image (c) after <i>dilation</i> , (d) after <i>image fill</i> , (e) after <i>erosion</i> , and (f) after <i>area thresholding</i> operations. In Figs. (b)-(f), the intermediate melanoma masks are superimposed on the H&E image to show more insights	86
Figure 6.6.	Subjective comparison of cell nuclei segmentation results (contoured in blue color) (a) original test image, (b)-(g) Segmentation results for Voting+Watershed, gLoG+mRLS, SegNet, U-Net, NS-Net and the proposed INS-Net techniques, respectively.	89
Figure 6.7.	Subjective comparison of nuclei classification results of H&E-stained image shown in Figure 5.1. (a) The ground truth image, nuclei classification results of (b) NS-Net+FC, and (c) the proposed INS-Net.	89
Figure 6.8.	Subjective comparison of MRD results (a) The ground truth image (b) Melanoma detection using NS-Net+FC+MRD technique and (c) Melanoma detection using INS-Net+MRD technique.	90

Figure 6.9.	Subjective comparison of the detected melanoma regions. (a) The ground truth segmentation mask (green contour), melanoma regions detected by (b) PBS-ResNet, (c) NS-Net+FC+MRD, and (d) INS-Net+MRD. The melanoma regions are shown with blue contour. The last row shows the FP (green), TP (green), FN (red) and TN (black) regions.	92
<b>Figure A.1.</b>	<b>Lymph node histopathological tissue image dataset. A total of 39 SLN images from 10 tissue sections (from 10 patients). Note that the WSI images with same color contour belong to the same lymph node tissue, but consecutive sections, stained with different stains (H&amp;E, MART-1, Ki-67, CD-45, and S100).</b>	<b>108</b>
Figure A.2.	Ten pairs of Histopathological Images obtained using the MART-1 and Ki-67 stains.	109
Figure A.3.	Seventy ROI windows, each with size 704x1280 pixels, used for the PI calculation. Note that the seven images in a row belong to the same patient.	110
Figure A.4.	Four pairs of Histopathological Images (WSI) with MART-1 and H&E stains.	111
Figure A.5.	Two hundred ROI windows, each with a size of 1000x1000 pixels, extracted from the four slides in Figure A.3. Note that the first row in each row-pair (inside a black rectangular contour) shows the H&E-stained blocks and the second row shows the corresponding MART-1 blocks.	112
Figure A.6.	The H&E-stained blocks in Fig. A.4 with the corresponding ground truth segmentation masks shown in the first and second rows (inside a black rectangular contour), respectively. Note that the melanoma nuclei, non-melanoma nuclei and background pixels are shown in red, blue, and white color, respectively.	113

# Abbreviations

ACM	Active Contour Model
ANN	Artificial neural networks
CAD	Computer Aided Diagnosis
CAIA	Computer Aided Image Analysis
CNN	Convolutional Neural Network
CMM	Cutaneous Malignant Melanoma
CT	Computed Tomography
DoI	Depth of Invasion
FCM	Fuzzy C-means
FN	False Negative
FP	False positive
gLoG	generalized Laplacian of Gaussian
GMM	Gaussian Mixture Model
H&E	Hematoxylin and Eosin
HFM	High Frequency Measure
HOG	Histogram of Oriented Gradient
IHC	Immunohistochemical
LBP	Local Binary Pattern
MAE	Mean Absolute Error
MART-1	Melanoma Antigen Recognized by T cells 1
ML	Machine Learning
mRLS	multiple Radial Lines Scanning
MRD	Melanoma Regions Detection
NA	Number of the Active Nuclei
NP	Number of the Passive Nuclei

PI	Proliferation Index
ReLU	Rectified Linear Unit
RGB	Red, Green and Blue channels
RMSE	Root Mean Square Error
ROI	Regions of Interest
SLN	Sentinel Lymph Node
SLNB	Sentinel Lymph Nodes Biopsy
SVM	Support Vector Machine
TN	True Negative
TP	True positive
UV	Ultraviolet radiation
WSI	Whole Slide Image



# Chapter 1

## Introduction

Computer-aided analysis and diagnosis through rapidly evolving medical imaging plays an increasingly important role in clinical diagnosis procedures. The objective of this thesis is to propose a methodology for applying computer aided image to grade and detect skin cancer (melanoma). This study is based on histopathological images. In this chapter, a brief background on skin cancer is first presented and then we will briefly present the process of specimen preparation and digital imaging in histopathology. Finally, we present the motivation and objectives of our research.

### 1.1. Skin Cancer and Diagnosis

Cancer is a major health problem around the world, which affects the human body and may result in death. Cancer results in uncontrolled cell growth which may metastasize to different important organs and exacerbate the condition. There are about 200 types of cancer, the most common type of cancer being skin cancer . Skin cancer is divided into three forms: basal cell carcinoma, squamous cell carcinoma and melanoma. Melanoma is a dangerous type of skin cancer, common throughout the world. Skin cancer behaves aggressively and unpredictably metastasizing to any part of the body. As per a recent statistic, about 87,110 people will be diagnosed with invasive melanoma, and about 9,730 are expected to be deceased from it in the United states alone, in 2021[1]. Melanoma starts in melanocyte cells, which is an epidermal cell that produces melanin and located in the basal layer. In a healthy body, melanocyte cells protect the nuclei of keratinocyte cells, which is an epidermal cell, from the sun damage by injecting their cytoplasm with melanosomes. When the ultraviolet radiation (UV), rays emitted by the sun, passes through the keratinocyte cells and is absorbed by the melanocyte DNA, the mechanisms of DNA transcription and replication might block and cause rapid growing in melanocyte cells. Melanoma can be invasive, and doctors can grade the invasive melanoma based on the thickness of the tumor and diagnose if the melanoma cells have spread to lymph nodes or other parts of the body (see Figure1.1). The invasive melanoma can move into different organs either through the lymph vessels or blood vessels. If the melanoma is detected at early stages, it can be cured by a simple

excision [2]. Therefore, an early detection and accurate prognosis of malignant melanoma will definitely help to lower the mortality from this cancer. In the diagnosis of skin melanoma, a few diagnostics tests are generally performed at hospitals. The first medical exam that doctors usually perform is a physical exam and a review of the patient's medical history. The patient with suspicious lesions is then referred to a dermatologist (a doctor specialized in skin diseases), who utilizes advanced techniques (e.g., dermoscopy) to analyze the skin lesions with precision . If a dermatologist determines that a spot might be a melanoma, a sample of skin is removed from the suspicious area and sent to a medical laboratory for histopathological examinations by pathologists. Histopathological examination is a process of the microscopic examination of nuclei morphology and tissue distributions for disease diagnosis. The diagnosis from histopathology image is the gold standard for almost all types of cancers, including skin melanoma [3].

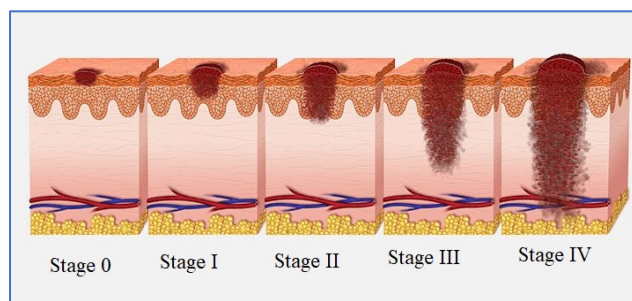


Figure 1.1. Invasive melanoma stages.

## 1.2. Histopathology Imaging

Histopathology refers to the microscopic examination of tissue to study the manifestations of the disease [4]. In order to identify cytological and morphological features that indicate the existence of cancer, pathologists observe histological slides under the microscope and examine tissue components at different scales to make a judgement based on their personal experience and knowledge. In order to utilize a microscope for examination, slide preparation is required prior to diagnosis examination. First, a biopsy sample is excised from a suspicious lesion. Second, fixation by some chemical fixatives (e.g., formalin) is performed to stop the enzyme activity, and preserve the cells and their morphological and architectural structures. Third, water is removed from the tissue, and some chemical agent (e.g., paraffin) that solidifies the tissue is embedded into the specimen to allow the thin layer to be sectionally to be cut. Fourth, sectioning where the embedded tissue sample is cut into thin sections (e.g.,  $4\mu\text{m}$  for light microscope) by a steel knife mounted in

a microtome. Fifth the thin sections are mounted to a glass slide and stained with one or more microscopical stains [5]. Since cells and other extracellular structures making up most tissue specimens are colourless, staining is applied to reveal cellular components and provide contrast to the tissue [6, 7]. In clinical histology, the most-widely used stain is a combination of Hematoxylin and Eosin (H&E) [8]. Hematoxylin is an alkaline stain with deep purple or blue color, and eosin is an acidic stain with a red color. With H&E staining, the chromatin in cell nuclei are stained with blue shade, while the cytoplasm and other connective tissues are stained with different shades of pink (see Figure 1.2(a)).

Although H&E stains provide a good contrast between cellular and extracellular structures, they are not specific to certain types of nuclei antigens relevant for melanoma diagnosis. Immunohistochemical (IHC) stains are widely used for staining biopsy slides in histopathology, which uses antibodies to stain particular antigens (e.g., proteins). IHC stains such as MART-1, PD-L1 and Ki-67 are typically used to identify specific types of nuclei characteristics in the tissue specimen. The MART-1 is commonly used to highlight the melanocytes in skin histopathological images, where melanocytes are observed as brown color and other types of cell nuclei are observed as blue color (see Figure 1.2 (b)). The Ki-67 stain is used to grade the melanoma by measuring the Proliferative Index (PI), where the proliferating cell appears in deep brown color. Melanoma and some other cancers (e.g., breast and lung cancer) also use PD-L1 stain to grade the melanoma by staining the tumor cell membranes with dark brown color. After staining, the tissue specimens are covered with a glass (or plastic) cover slip to hold the specimen in place. Usually, pathologists view the slides with the specimen under a microscope, and make the diagnosis based on a series of observation features (e.g., cell type and distribution). By utilizing these different specific stains, physicians can diagnose a tumor as benign or malignant, and determining the stage of a tumor. With recent development in digital tissue slide scanners (for more see in [9]), glass slides of tissue specimens can now be digitized at high magnification to generate the Whole Slide Images (WSIs) [10]. Pathologists examine the digitized tissue slides at different scales using computer softwares. Figure 1.2 (a)-(d) shows an example of skin images stained with H&E, MART-1, Ki-67, and PD-L1, respectively.

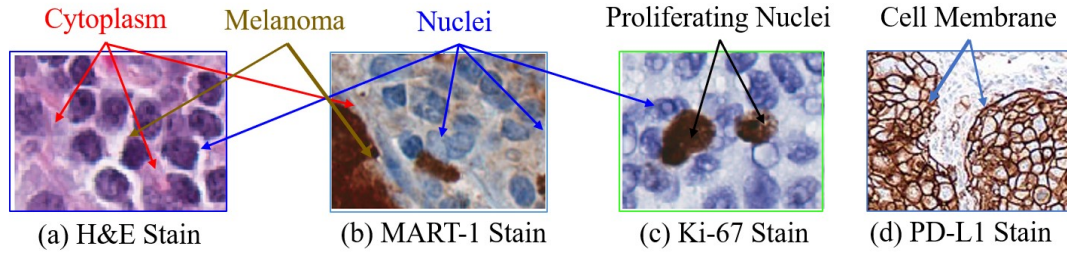


Figure 1.2. Examples of Histopathological images with different stains.

### 1.3. Melanoma Diagnosis and Grading in Skin

In the first stage, dermatologists usually examine a patient's skin externally by applying the ABCDE criteria, where they look for these signs: Asymmetry, irregular Borders, more than one or uneven distribution of Color, or a large (greater than 6mm) Diameter. Finally, pay attention to the Evolution of the moles (see Figure 1.3) [11]. Several techniques have been developed, e.g., epiluminescence microscopy [2] and confocal microscopy [25] for diagnosing melanoma.

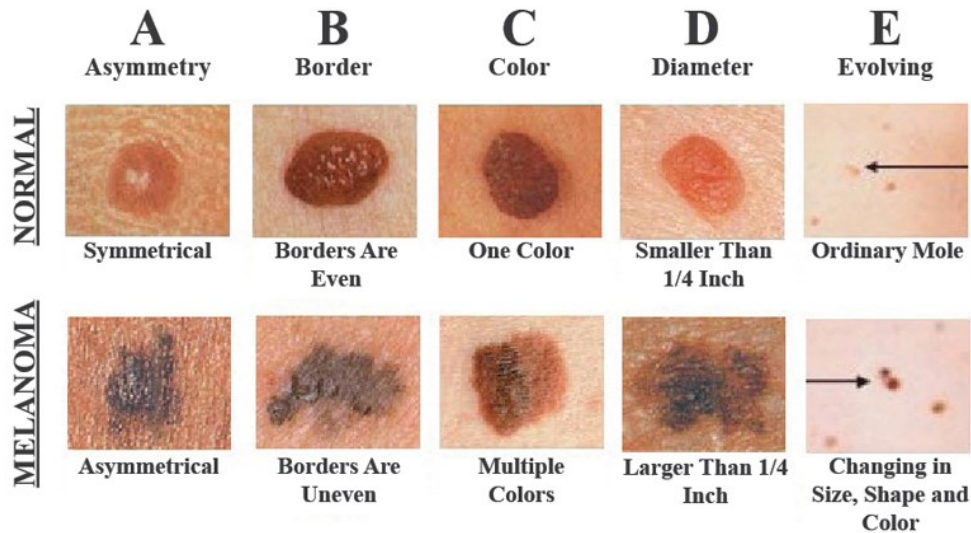


Figure 1.3. The ABCDE criteria for detecting melanoma (Image Credit: [12]).

To move further in diagnosing, the histopathological examination is a convenient tool to distinguish between the skin melanoma and melanocytic nevus. In the following, we will first briefly explain the typical structures of human skin, and then illustrate how to diagnose and grade skin melanoma from histopathological images.

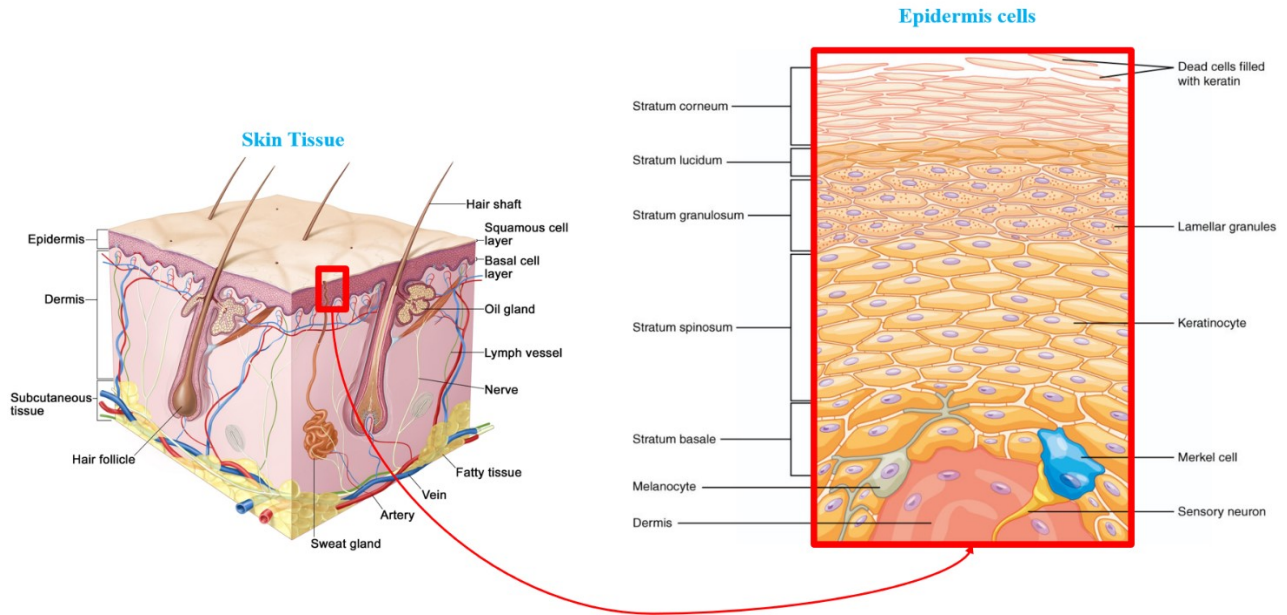


Figure 1.4. Anatomy of normal skin (Image Credit: [13]).

### 1.3.1. Skin Structure

The skin is the biggest organ in the human body, and it is the outer layer, a membrane covering the surface of the body. Human skin has many functions, including thermo regulation and environmental protection [14]. The skin consists of three main layers: epidermis, dermis, and subcutaneous tissue, each layer provides a distinct role in the overall function of the skin as an organ. Figure 1.4 shows the anatomy of normal skin. Each of the 3 skin layers are described below.

- a) **Epidermis layer:** The Epidermis layer is the outermost layer of the skin, protecting protects the body from the infections and from environmental pathogens. This layer can be divided into five sub-layers: Stratum Basale, Stratum Spinosum, Stratum Granulosum, Stratum Lucidum, and Stratum Corneum (see Figure 1.4). The epidermis contains four types of cells: Keratinocytes, Melanocytes, Langerhans and Merkel Cell. The keratinocytes constitute 90% from the epidermis layer, where the melanocytes have a low population and constitute 8% from the Basale layer. The average thickness of the epidermis layer is  $0.1\text{ mm}$  and it is varying from region to another in the body.
- b) **Dermis layer:** The Dermis layer is the inner layer of skin, located underneath the epidermis and above the subcutaneous tissues. This layer usually contains blood vessels, lymph vessels, hair follicles, and few glands and it is divided into two layers: papillary dermis and reticular

dermis. The average thickness of dermis is 0.35 mm. The dermis cells are divided into three types: fibroblasts, macrophages, and mast cells.

- c) **Subcutaneous tissue:** The Subcutaneous tissue is the innermost layer of human skin, which blends indistinctly with the dermis. It contains loose connective tissue and lobules of fat that hold large blood vessels.

### **1.3.2. Histopathological Examination for Skin Tissue**

The inevitability of the diagnosis step is done by examination of the digitized skin tissue by Pathologists. This is done by staining the suspected melanoma region using different stains such as H&E, MART-1, S-100, PD-L1, CD-45 and Ki-67. After melanoma diagnosis, pathologists grade the melanoma by measuring the Breslow thickness (depth of invasion), PD-L1 score and Proliferation Index (PI), in order to effectively plan the patient's treatment. The Breslow thickness is defined as the maximum distance between malignant cells and the top of the granular layer [15]. The PD-L1 score is a percentage of the tumor nuclei that their membrane is stained with PD-L1 stain to the total number of nuclei. On the other hand, the proliferation index is defined by measuring the percentage of proliferative nuclei (see Figure1.2).

## **1.4. Melanoma Diagnosis and Grading in Lymph Node**

Once melanoma is diagnosed by analyzing skin epidermis/dermis layer, the doctors typically do a lymph node biopsy to determine if melanoma has invaded the lymphatic system [16,17]. The lymph node structure is described below, and Figure 1.5, shows how the melanoma is diagnosed and graded from lymph node histopathological images.

### **1.4.1. Lymph Node Structure**

Besides the cardiovascular system, the human body contains a lymphatic system that consists of a network of vessels, that collect and purify the drained lymph from the tissue (see Figure1.5 (b)). The lymph is defined as a fluid containing infection-fighting white blood cells and it is returned to the bloodstream through the right subclavian vein. The lymph is purified by passing through lymph nodes, which are small bean-shaped glands with an average size of 1cm the size varying based on the location and age. These lymph nodes are found in clusters approximately 500-700 count spread throughout the human body, as shown in Figure1.5 (a). The anatomy of lymph node structure



consists of capsule, cortex and medulla, and it has B and T lymphocytes, and other white blood cells [18-19].

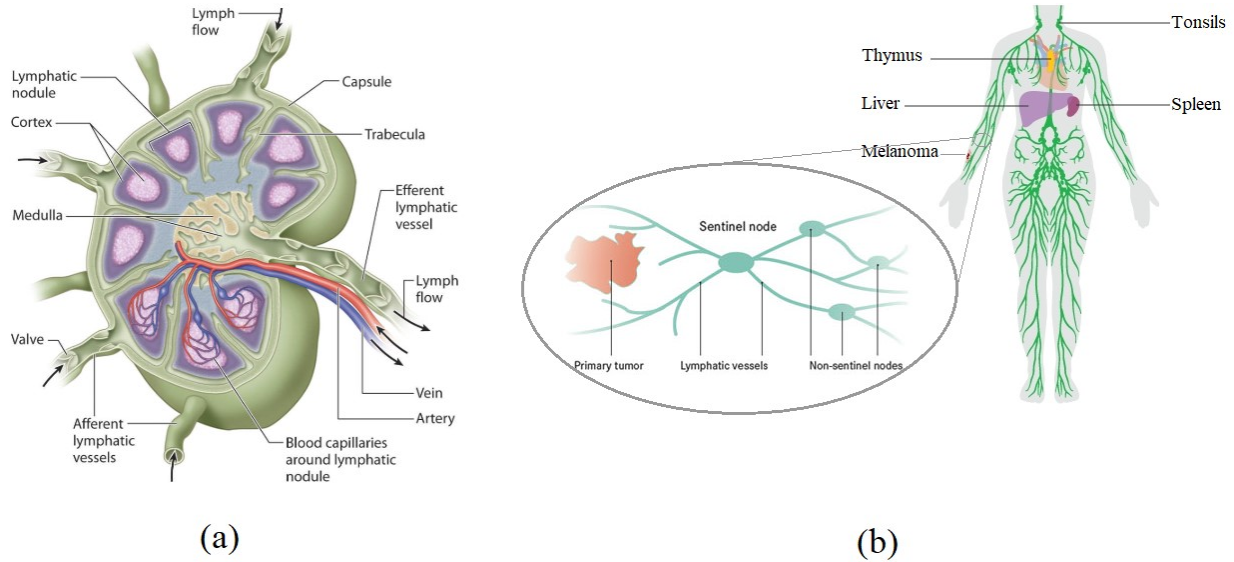


Figure 1.5. Lymphatic system (a) Anatomy of a lymph node and (b) the lymphatic system in human body.

#### 1.4.2. Histopathological Examination for Lymph Node Tissue

When it is suspected that melanoma has invaded epidermis/dermis, doctors typically excise a section of the Sentinel Lymph Nodes (SLNs) and examine them for grading melanoma [20-22]. The sentinel nodes are defined as first lymph nodes where the tumor drains into them through lymph vessels (see the magnified region of melanoma in Figure 1.5 (b)). Typically, histopathologist slices the SLNs into biopsies and stains them with varying stains. The pathologists analyze the melanoma and measure the PI values in digitized biopsies. The PI is considered as the most important factor for grading the melanoma in the lymph nodes images [23-24].

### 1.5. Problem Statements and Motivation

Manual analysis of histopathological images is labor-intensive, time consuming, and suffers from intra/inter-observer variability. Therefore, CAIA systems are being increasingly used in the medical community. Since the histopathological examination of a skin WSI by pathologists provides the gold standard for the diagnosis [26], the melanoma research and associated CAIA systems have thrived. Figure 1.6 shows different research directions on melanoma, where the yellow blocks show the existing works, and the blue blocks shows the CAIA systems proposed in

this thesis. The previous works [16, 17, 26, 27] primarily focused on the detection and grading of melanoma on the skin WSI.

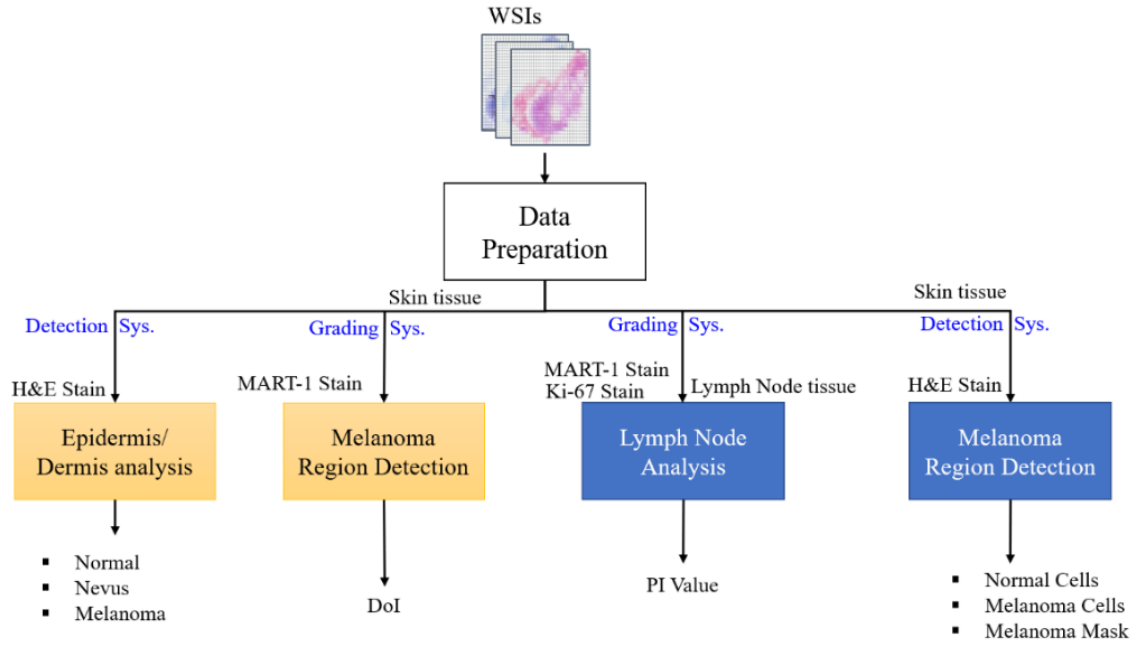


Figure 1.6. The melanoma research directions. The yellow blocks represent the previous works, and the blue blocks represent the proposed CAIA systems.

The main objective of this thesis is to develop robust and efficient image analysis and machine learning techniques for the purpose of detecting and grading the melanoma regions. In this thesis, four CAIA systems are proposed to grade and detect melanoma in histopathological images. Two CAIA systems have been developed to calculate the proliferation indices on the melanoma regions on Ki-67 WSI. The implementation of the developed CAIA systems are implemented using image processing and machine learning based techniques.

A major problem with the melanoma detection is that malignant melanoma is difficult to detect in H&E-stained images. To alleviate this problem, doctors sometimes use an immunohistochemical stain, known as MART-1, that is very specific to melanoma. Therefore, two CAIA systems have been developed to detect malignant melanoma regions on H&E stained WSI. The detection CAIA systems are implemented by utilizing two approaches: classical image processing approach and hybrid machine learning approach.

In this research, we used different stains, such as H&E, MART-1, and Ki-67, to grade and detect melanoma in skin and lymph node tissue as shown in the blue blocks in Figure 1.6. The grading



and detection of melanoma regions are very important to the pathologists for making the treatment plans for patients. Note that the H&E stain, a widely used stain in histopathology, provides the cellular structure of the cells, whereas the MART-1 is a special stain used to detect the melanoma regions (stained as brown) in a biopsy slide. The Ki-67-stain is a special stain used to detect the cells with mitotic activities. With this stain, the proliferative cells are stained as black (see Figure 1.2).

## **1.6. Organization of the Thesis**

The thesis is organized as follows: Chapter 2 presents a broad literature review on image processing techniques used for histology analysis as well as existing skin/lymph image analysis techniques. In Chapter 3, we present the first proposed CAIA system to grade melanoma by calculating the Proliferation Index (PI) on lymph node tissue. The proposed CAIA system includes a novel lymph node segmentation technique for histopathological images and a feature-based method to calculate the PI values in melanoma regions. Chapter 4 presents the second CAIA system to calculate the PI values using a novel CNN architecture and machine learning algorithm. Chapter 5 presents the third CAIA system to segment and classify the nuclei on H&E-stained images of lymph node tissue. The proposed CAIA system uses a feature vector extracted from each nucleus and classify them into melanoma and non-melanoma nuclei using an SVM classifier. Chapter 6 presents the fourth CAIA system to detect and segment melanoma regions in H&E-stained images. The proposed CAIA system includes a novel CNN architecture to segment melanoma nuclei in H&E-stained images, and a post processing technique to generate the melanoma regions. Finally, the conclusions and future research directions are presented in Chapter 7.

# Chapter 2

## Literature Review

In this chapter we present a brief overview of computer-aided image analysis techniques for histopathological images. The literature review covers a range of commonly used image processing algorithms related to regions of interest (ROIs) segmentation, features extraction and classification. The state of the arts related to WSIs analysis with different types of cancer including skin cancer.

### 2.1. Generic Automated CAIs in Histopathology

The purpose of a CAD system is to process the input images and result a useful information (e.g., depth, population or shape of suspected lesions) for diagnosis, which may serve as a “second opinion” to assist expert pathologist in interpreting medical images so that the efficiency and accuracy of diagnosis could be improved [28,29]. Figure 2.1 shows the general framework of a typical CAD system. It includes four major steps: segmentation, features extraction, classification and performance evaluation, which are reviewed in the following sections.

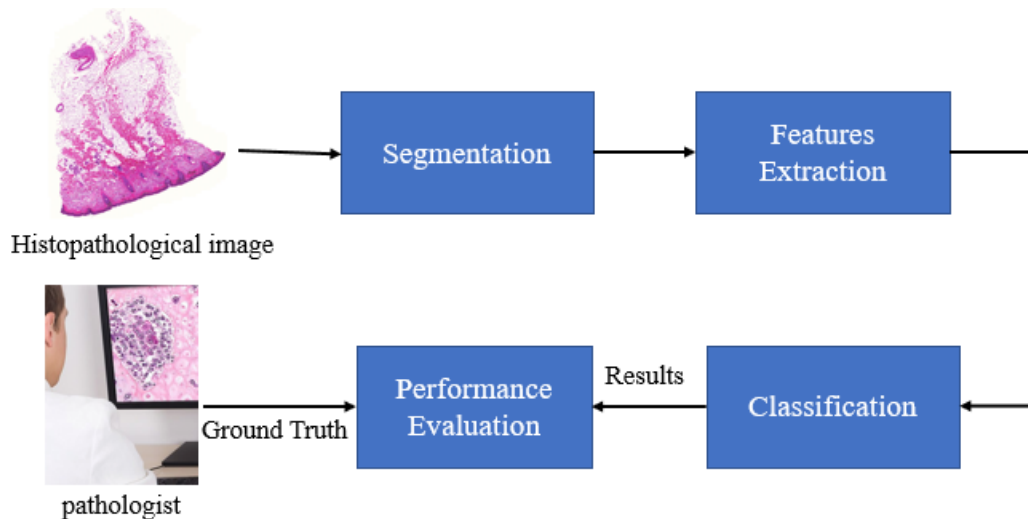


Figure 2.1. General framework of a CAD system.

### 2.1.1. Segmentation and ROIs detections

In most automated CADs, segmentation of regions of interest (ROI) is an important step before any subsequent quantitative analysis, such as features extraction and classification for lesion identification. This step reduces the computational time of processing the entire WSI and improves the subsequent quantitative analysis from interfacing with other unwanted regions in the WSI. This section reviews some basic techniques in segmentation that are widely used in histopathological images.

#### Thresholding

Thresholding is a primarily tool that has been widely used by researchers to segment the region of interest in medical images [27, 29-31]. The segmentation is usually performed on the pixel intensity of the image and dividing the image regions into groups of pixels as following:

$$I'(x,y) = \begin{cases} \text{Class1} & \text{if } \tau \leq I(x,y) \\ \text{Class2} & \text{if } \tau > I(x,y) \end{cases} \quad (2.1)$$

where  $I'(x,y)$  is the segmented pixel at the coordinated  $(x,y)$ ,  $I$  is the input image and  $\tau$  is the intensity threshold. Ahmady *et al.* [29] proposed a thresholding technique for nuclei segmentation in H&E-stained images. The technique Performa multiple levels of Otsu thresholds [30,31], then choosing the highest threshold to segment the image. Lu *et al.* [27] proposed to use adaptive threshold for non overlapping blocks. Selection of thresholds is then performed to avoid the under-segment nuclei regions using prior knowledge about nuclei size and shape.

#### Active Contour Models (ACMs)

The Active Contour Model is originally introduced by Katz, Terzopoulos and Witkin [32-34] and it is being used in different algorithms such as objects tracking, shape recognition, segmentation, edge detection. The common idea of these algorithms is to evolve an initial continuous curve in a 2-D plane to delineate structures in an image. The evolution of the ACMs is subject to constraints from the given image by seeking to minimize an energy function based on gradient or intensity information. Several researchers have used the ACMs and level sets for ROIs segmentation in histopathological images [35,36]. Fatakdawala *et al.* [37] used Geodesic Active Contour (GAC) to segment the nuclei in histopathological images of Breast Cancer after using an initial mask obtained by a Gaussian mixture module that was used for nuclei detection. Hafiane *et al.* [38] proposed to use glandular structure characterization with multiple level set active contours to

segment the nuclei in the in histopathological images of Prostate Cancer. Although these techniques are reported to provide a good performance, the results are very sensitive to the initialization mask and local intensity variations in images. In addition, the ACMs and level sets have a high computational complexity.

## **Clustering**

Clustering is a process of grouping data into a number of clusters, where the data in the same group (i.e, a cluster) are more alike to each other than those in other clusters. There are many clustering algorithms that have been used in image segmentation such as K-means Fuzzy C-means and Mean-shift. Many research Chapters used K-means in nuclei segmentation [16,39-42]. Sertel *et al.* [43] proposed a technique for follicular lymphoma grading, which used K-means clustering algorithm on the histopathological images of Follicular Lymphoma cancer to segment nuclei, cytoplasm and extracellular material based on La\*b\* color space. Xu *et al.* [44] used the Mean-shift algorithm to cluster the elected points obtained by the voting algorithm. The voting algorithm is applied on the nuclei boundary (obtained by initial segmentation) to estimate the candidate nuclei seed. Edulapuram *et al.* [45] proposed a technique for nuclei segmentation using fuzzy c-mean and level set active contour model for uterine cervix biopsy images.

### **2.1.2. Features Extraction**

Feature extraction is a very important step to analysing an image and defining the important objects. There have been many published researches for features extraction in the histopathological images. Some of these features are related to texture, morphology and architecture of segmented ROIs.

#### **Textural features**

In histopathological images, texture features can analyze different tissue regions with different kinds of nuclei. Here are some texture features that have been used widely in the literature:

1. RGB features: present the red, green and blue intensity values of pixel.
2. First-order Textures: present the histogram intensity which includes the mean, standard deviation, smoothness, third moment, uniformity and entropy.
3. Histograms of Oriented Gradient (HOG) present the appearance of an object using the distribution of local intensity gradients and edge direction.

4. Filter features: present edges in different directions, high frequency component and blob structure using wavelet transform, Gaussian filters, Law's filters and Gabor filters.
5. Haralick texture features: present the homogeneity of pixel intensity with neighbourhood pixels using the gray level co-occurrence matrix.
6. Local Binary Patterns (LBP) present the pixel value relation with neighbourhood pixels in a certain window.

Feature extraction is a way to represent the object in different platforms which can help us to understand and to segment, detect, classify or track the RoI. Dataret *et al.* [46] used the color features (RGB values) combined with five Law's filters features, followed then by Hierarchical Self-Organizing Map (HSOM) to cluster the tissue components (Prostate cancer microscopy images) into glands, epithelia, stroma and nuclei. Wei *et al.* [47] proposed to detect Cervical Cancer using First order features followed then by K-means classifier. Ojansivu *et al.* [48] proposed to use LBP features and Local Phase Quantization LPQ features, followed by Support Vector Classifier SVM to detect cancer morphology in breast cancer microscopy images. Korkmaz *et al.* [49] used LBP and HOG features and features selection techniques, then the obtained features are classified using Artificial neural networks (ANN) for detecting stomach cancer.

### **Morphological features**

During the manual observation of WSI, doctors usually describe many tissues or nuclei characteristics in terms of morphological features. The morphological features play a significant role in describing the lesion. In the following, we list the widely used morphological features:

1. Regional features are related to area, perimeter and center.
2. Convex hull features are derived from the convex hull [50] of ROI. These features may include the solidity, convex deficiency, convex area and concavity.
3. Elliptical features are derived from the best fitted ellipse [51] of ROI. These features may include the major and minor axis and the ratio between them, eccentricity, orientation, and ellipticity.

The morphological features are usually combined with other features (e.g., textural features) for disease diagnosis and grading. The typical applications include follicular lymphoma grading [43], cervical intraepithelial neoplasia diagnosis [52] and melanocytic histology classification [53].

### 2.1.3. Classification

After feature extraction, a candidate region can be classified into lesion or non-lesion using machine learning models. In this section, four widely used models are reviewed.

#### Support Vector Machine (SVM)

SVM is widely used in most of the applications starting from hand-written character recognition to tumor detection because of the high performance even with noisy dataset. The SVM model can be trained with  $k$ -class, features vector  $\{f_1, f_2, \dots, f_n\}$  and their labels  $\{L_1, L_2, \dots, L_n\}$ . SVM will create a best hyperplane that can separate these labeled feature vectors with maximum margin by achieving the following equation.

$$\begin{aligned} \min_{w,b} \quad & \frac{1}{2} \|w\|^2 \\ \text{s.t.} \quad & (w^T f_i + b) L_i \leq 1, \quad i = 1, \dots, n \end{aligned}$$

Where  $w$  is the normal vector to the hyperplane,  $f_i$  is the  $i$ th features vector and  $L_i$  is its label. Then finding  $w$  which give a hyperplane as  $w^T F + b = 0$  by solving the above quadratic programming problem [54,55]. SVM classifiers can also be used to separate un-separable data by increasing the dimensionality with different kernels.

#### Artificial Neural Network (ANN)

Inspired by biological neuron function. The ANN consist of collections of artificial neurons (nodes) and are connected with each other through weighted connections [56-58]. The typical

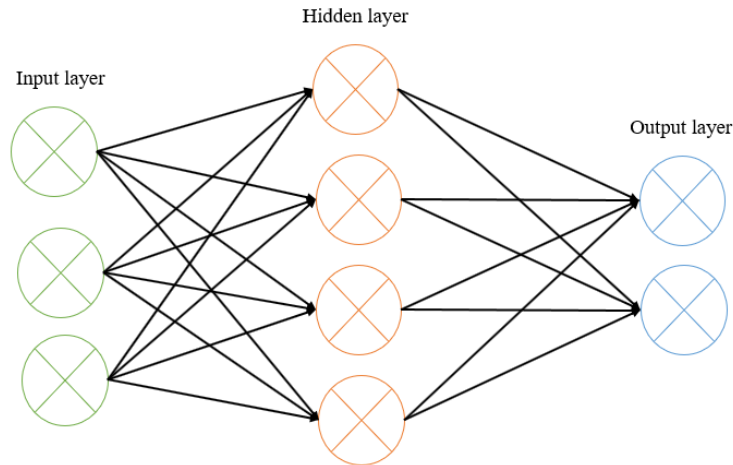


Figure 2.2. Example of a three-layer of ANN.

architecture of an ANN starts from an input layer (features) connected to the first collection of neurons (hidden layer) and another collection of neurons (output layer). Figure 2.2 shows an

example of ANN, and it is a three-layer feed-forward network. These weight connections can determine the input features class; therefore, backpropagation learning algorithm is used to update the weights connections by minimizing and optimizing the error between the desired output and actual output.

#### 2.1.4. Performance Evaluation Metrics

Most of the techniques are evaluated using different types of measures (e.g., recall, precision and etc.). The purpose of evaluation is to determine the performance and robustness of a CAD system compared to the ground truth. The evaluation usually applied on the testing data, when the data is divided into testing and training in machine learning algorithms. The objective evaluation of a binary classification system, is calculated using the commonly used measures such as *Recall*, *Precision*, *Specificity*, *Accuracy*, and *F-Score* as follows:

$$Recall = \frac{TP}{TP + FN} \times 100\%$$

$$Precision = \frac{TP}{TP + FP} \times 100\%$$

$$Specificity = \frac{TN}{TN + FP} \times 100\%$$

$$Accuracy = \frac{TP + TN}{TP + FP + FN + TN} \times 100\%$$

$$F - Score = \frac{2 \times Recall \times Precision}{Recall + Precision} \times 100\%$$

where  $TP$ ,  $TN$ ,  $FN$  and  $FP$  denote the number of true positives, true negatives, false negatives and false positives, respectively. The F-score (also known as BF score and Dice score) is the harmonic mean of the recall and precision and it is used to show the similarity of the predicted and ground truth boundaries [59]. The evaluation can be extended for a number of classes by calculating the performance evaluation for each class individually.

## 2.2. Existing Grading CADs in histopathological images

Several techniques have been proposed in the literature to calculate the PI for different tumor regions such as pancreatic neuroendocrine, breast carcinoma and melanoma on lymph nodes. Grala *et al.* [60] proposed a technique based on thresholding, watershed and morphological operations

for nuclei recognition in breast cancer images. The Support Vector Machine (SVM) is then used to classify the RGB nuclei pixels into passive/active nuclei, and the PI value is calculated. Akakin *et al.* [61] used watershed segmentation and Laplacian-of-Gaussian filtering for nuclei detection, and SVM as active/passive nuclei classifier. The PI value was calculated by measuring the active nuclei ratio. Al-Lahham *et al.* [62] proposed a technique, where K-mean was used to classify the input image pixels ( $L^*a^*b^*$  color-space) into three classes: background, passive and active nuclei followed by PI calculation. Mungle *et al.* [63] proposed a technique to measure the PI in a Ki-67-stained breast biopsy image using fuzzy C-means (FCM) and K-means (KM). The FCM segments the nuclei using a fuzzy threshold and the KM is used to classify the masked nuclei into passive and active nuclei.

The deep learning algorithms using CNN have recently been used successfully in medical image analysis. It has been shown to provide high performance with low computational complexity in many applications. There are different architectures of CNN models for different tasks such as classification or segmentation. Ciresan *et al.* [65] proposed a CNN-based technique to segment neuron membranes in electron microscopy images. The CNN contains four convolutional layers followed by two fully connected layers. The segmentation is performed by classifying each pixel individually based on a square area surrounding the pixel. Although the technique provides good segmentation results, it has a high computational complexity as each pixel is classified separately. Long *et al.* [66] proposed a low complexity CNN based technique for object segmentation. Like most CNN architectures, it includes several convolutional layers, a few(max) pooling layers and fully connected layers. However, this technique has one learnable upsampling layer instead of fully connected layers. The learnable up-sampling layer helps to reconstruct the class probability map (for all pixels) with the same size as the input image. The class probability is then thresholded to obtain the segmented image. Although, this technique has a low complexity, some information is lost around the boundaries/edges. Basrinarayanan *et al.* [67] proposed the SegNet architecture for efficient object segmentation. The technique uses a number of up-sampling layers which are compatible with the number of max pooling layers. Furthermore, the SegNet transfers the max pooling indices into upsampling layers to reduce the blurriness around the boundaries/edges. The experimental results show a good performance of SegNet for object segmentation in terms of the computational time and error rate. For PI calculations using deep learning, Monjoy *et al.* [64] proposed a technique to measure the PI value for breast cancer. The technique used Gamma



mixture model (GMM) with Expectation-Maximization algorithm to detect the nuclei seeds, and image patches around isolated nuclei seeds are then classified into passive/active nuclei using a CNN classifier. After the CNN classifier, the PI is calculated for these images' patches of the dense area with active nuclei, which is provided by doctors. The GMM based nuclei detection algorithm typically has a high computational complexity and also does not work well on the nuclei clusters.

# Chapter 3

## Novel Lymph Node Segmentation and Proliferation Index Measurement for Skin Melanoma Biopsy Images

The lymphatic system is the immune system of the human body, and includes networks of vessels spread over the body, lymph nodes, and lymph fluid. The lymph nodes are considered as purification units that collect the lymph fluid from the lymph vessels. Since the lymph nodes collect the cancer cells that escape from a malignant tumor and try to spread to the rest of the body, the lymph node analysis is important for grading many types of skin and breast cancers. In this Chapter, we propose a Computer Aided Diagnosis (CAD) method that segments the lymph nodes and melanoma regions in a biopsy image and measures the proliferation index. The proposed method contains two stages. First, an automated technique is used to segment the lymph nodes in a biopsy image based on histogram and high frequency features. In the second stage, the proliferation index for the melanoma regions is calculated by comparing the number of active and passive nuclei. Experimental results on 76 different lymph node images show that the proposed segmentation technique can robustly segment the lymph nodes with more than 90% accuracy. The proposed proliferation index calculation has low complexity and has an average error rate less than 1.5%.

### 3.1. Introduction

Melanoma is a dangerous type of skin cancer, spread around the world, though it is less common compared to Lung cancer, Prostate cancer, Breast cancer, etc [1,68]. Melanoma is caused by the aggressive growth of melanocytes typically found around the epidermis-dermis junction. Due to excessive exposure to ultraviolet radiation, the nucleus DNA of melanocytes may be damaged causing abnormal growth. Melanoma shows aggressive and unpredictable behaviour which can spread to any part of the body. As per a recent statistic, about 87,110 people could have been diagnosed with invasive melanoma, and about 9,730 would have died from it in the United states alone in 2017 [69]. Once melanoma is diagnosed by analysing skin epidermis/dermis layer, the doctors typically do a lymph node biopsy to determine if melanoma has invaded the lymphatic system [16,17]. The melanoma passes to lymph nodes through the lymph vessels, after invading

the epidermis/dermis layer. It is important to diagnose and grade the melanoma in Sentinel Lymph Nodes (SLN), because it is the stage where melanoma can spread to different organs in the body through the lymph vessels [20]. The diagnosis is done by removing the Sentinel Lymph Nodes Biopsy (SLNB) [21,22]. The SLNB is sliced into very thin layers that are placed on a glass slide with histology stains for examination under a microscope by pathologists (see Figure 3.1). Traditionally, pathologists examine a SLNB slide under a microscope and a diagnosis is made based on their personal experience and knowledge, which are sometimes subjective and are prone to intra- and inter-observer variability [28,70]. With technological advances in digital imaging and computer hardware, the biopsy image can be digitized and analysed using automated image analysis techniques. The automated computer-aided image analysis can provide fast diagnosis, and reliable and reproducible objective results [52]. However, computer aided analysis of the biopsy images, face many challenges such as the blurry appearance due the slicing process of the tissue, the low contrast for some parts of the tissue and sectioning artifacts (e.g., missing and folding in some parts of the tissue) [71,72].

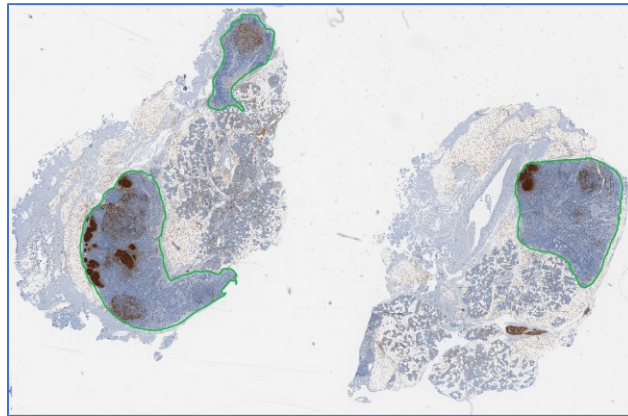


Figure 3. 1. Sentinel Lymph Nodes (SLN) biopsy stained with S-100 stain. The three lymph nodes are shown with green contour.

To the author's knowledge, no technique has appeared in the literature for automated lymph node segmentation of biopsy image. However, a few techniques have been proposed in the literature, for SLN segmentation in the Computed Tomography (CT) and ultrasound for breast cancer. These images have different characteristics compared to lymph node biopsy for detecting the skin cancer. Steger et al [73] proposed a lymph node segmentation technique in CT slices using gradient, intensity and shape information. Zhang et al [74] proposed a lymph node segmentation technique in ultrasound image by using a Convolutional Neural Network. The proliferation index (PI) is a

very important diagnostic and prognostic factor for cancer diagnosis. The proliferation index is measured by estimating the ratio of the numbers of active nuclei and all nuclei [23]. It is known that Ki-67 protein is present during all active phases of a cell cycle (G1, S, G2, and mitosis), but is absent in resting passive phase (G0) [24]. A special Ki-67 stain is typically used to stain this protein and identify the active nuclei [75]. In a Ki-67-stained image, the nuclei appear with two colors: the active nuclei appear dark brown and passive nuclei appear blue. Mungle et al. [63] proposed a technique to measure the PI in a Ki-67-stained breast biopsy image. In this technique, a pathologist manually identifies a few windows of tumor regions with high concentration of active nuclei. A Fuzzy C-means (FCM) based thresholding technique is used to separate the nuclei from the background. K-means clustering technique is then used to classify active and passive nuclei pixels. By comparing the areas of active and passive nuclei, the PI value is calculated. This technique requires input from a pathologist to identify the dense active nuclei regions. The FCM-based thresholding and K-means clustering, being iterative, have high computational complexity. In addition, the unsupervised K-means clustering technique does not perform well to classify the active and passive nuclei. In this Chapter, we propose a fully automated method to segment the lymph node tissues and measure the PI in biopsy images. The biopsy images may be stained with different histology stains such as Hematoxylin and Eosin (H&E), MART-1, S-100, CD-45 and Ki-67 stains [76]. For lymph node segmentation, the proposed technique segments lymph nodes using histogram and high-frequency local features. For PI calculation, it is assumed that a lymph node biopsy is stained with both MART-1 and Ki-67. The MART-1 stain is used to identify the melanoma regions by detecting a special protein called MART-1 that exists on the surface of melanocytes and the Ki-67 stain is used to detect the proliferative activity of the lymph node nuclei. In the proposed technique, the melanoma regions obtained from MART-1 images are mapped onto the corresponding Ki-67 image to automatically identify the melanoma regions in the Ki-67 image. Active and passive nuclei in the melanoma regions are then detected using Otsu thresholding and SVM classification. By comparing the number of active and passive nuclei, the PI value is calculated. The organization of the Chapter is as follows. Section 3.2. describes the dataset; Section 3.3. describes the lymph node segmentation technique in detail, followed by the PI calculation in Section 3.4. The conclusion is presented in Section 3.5.

### 3.2. Data Description

In this study, all lymph node histopathological images are collected from the Cross Cancer Institute, University of Alberta in accordance with the protocol for the examination of specimens with skin melanoma. The histological sections of lymph node tissues are about 4  $\mu\text{m}$  thick and are stained with different stains such as H&E, MART-1, S100, CD-45 and Ki-67 stain. The digital images were captured under 40X magnification on Aperio Scanscope CS scanning system (0.25  $\mu\text{m}/\text{pixel}$  resolution) with default calibration and illuminance settings (based on Aperio service notes). The proposed technique has been evaluated on a database of 39 whole slide images (WSI) with 88 lymph nodes. There were 9 images stained with H&E, 9 images with MART-1, 5 images with CD-45, 7 images with S-100, and 9 images with Ki-67 (more detail about the images can be found in Appendix A.1). The ground truth (segmented LN) images were obtained by manual segmentation by doctors. Figure 3. 1 shows the lymph nodes stained with S-100 stain and they are manually contoured by green contour.

### 3.3. Lymph Node Segmentation

The schematic of lymph node and melanoma segmentation is shown in Figure 3.2, which consists of three modules: Coarse Segmentation, Features Extraction, and Fine Segmentation. In the following we provide details of each module.

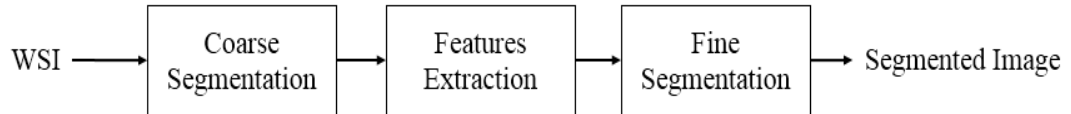


Figure 3.2. Schematic of the proposed segmentation technique.

#### 3.3.1. Coarse Segmentation

Most SLN images consist of four regions: melanoma metastasis (dark brown pixels), lymph node tissues, other tissues (e.g., remains of dermis, fat, parts of other lymph tissues, etc) and white background (which is not part of the actual biopsy tissue). In this module, a coarse segmentation is performed using the histogram of the image. This module calculates the required thresholds to classify the image into these four classes: *Class 1* (Melanoma), *Class 2* (Lymph node tissue), *Class 3* (Other tissue) and *Class 4* (Background). The steps are as follows:

1. Down sample the input image to reduce the data rate. For a 40x resolution input image, a down sampling factor of 8 is used in this Chapter. Assume that the down-sampled image is of size  $M \times N$ .
2. Convert the down-sampled RGB image into a gray image  $I(x, y)$ .
3. Calculate the histogram  $h(p)$ ,  $0 \leq p \leq 255$  of the image  $I$  (see the magnified part of Figure 3.3(a), which includes several local minima). The histogram is smoothed by using a median filter. The smoothing may be applied a few times, until three local minima values are obtained on the smoothed  $h(p)$ .
4. Determine the three  $p$  values at the local minima on the smoothed  $h(p)$  and denote them as  $\tau_1, \tau_2$  and  $\tau_3$  (see Figure 3.3). These values are to be used as thresholds for classification.
5. Classify the image pixels  $I(x, y)$ ,  $1 \leq x \leq M$  (rows),  $1 \leq y \leq N$  (columns) using thresholding into four classes as follows:

$$\varphi(x, y) = \begin{cases} \text{Class1} & \text{if } 0 \leq I(x, y) < \tau_1 \\ \text{Class2} & \text{if } \tau_1 \leq I(x, y) < \tau_2 \\ \text{Class3} & \text{if } \tau_2 \leq I(x, y) \leq \tau_3 \\ \text{Class4} & \text{if } \tau_3 \leq I(x, y) \leq 255 \end{cases} \quad (3.1)$$

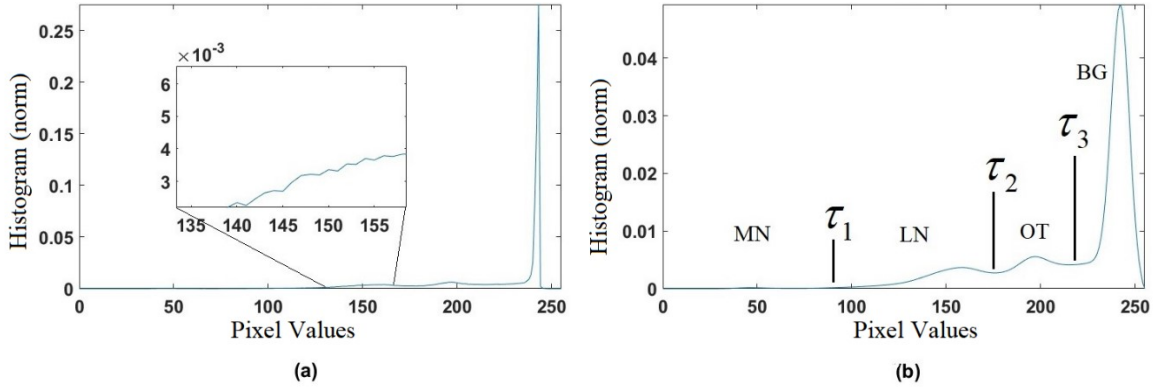


Figure 3.3. Histogram smoothing. a) original image histogram. b) smoothed histogram. MN: Melanoma, LN: Lymph node, OT: other tissue and BG: Background.

Note that, the pixel values of these four classes, typically vary between  $[0-100]$ ,  $[70-160]$ ,  $[120-200]$ , and  $[190-255]$ . Figure 3.3 (b) shows the smoothed histogram corresponding to the image shown in Figure 3.1, with  $\tau_1 = 80$ ,  $\tau_2 = 168$  and  $\tau_3 = 203$ . Figure 3.4 shows the coarse segmentation image obtained after thresholding.

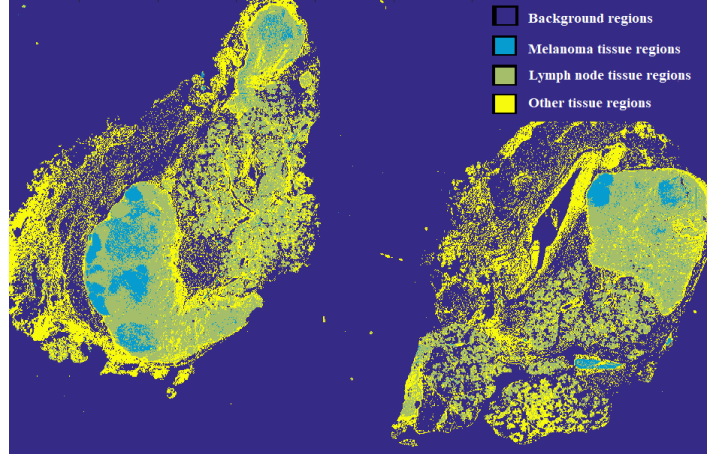


Figure 3.4. Coarse pixel classification using thresholding. Light blue, yellow, green and dark blue pixels represent *Class 1*, *Class 2*, *Class 3* and *Class 4*, respectively.

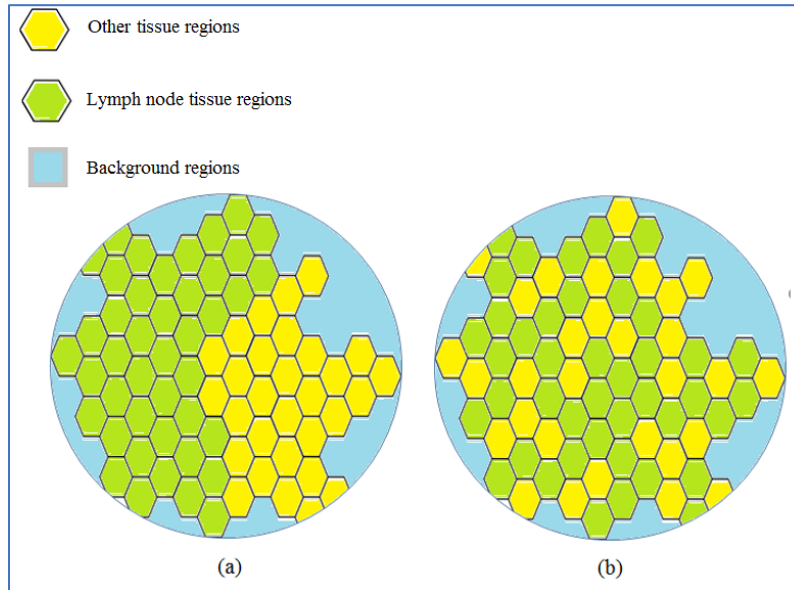


Figure 3.5. Example of classified image, a) lymph node tissue has massive behave within  $G_{x,y}$ . b) lymph node tissue has scattered within  $G_{x,y}$ .

### 3.3.2. Features Extraction

In this section, we extract the features from the coarse classified image  $\varphi$ , which will be used for fine segmentation in section 3.3.3. A circular neighborhood  $G_{x,y}$  with radius  $r$  is defined for each classified pixel at coordinate  $(x, y)$ . The neighborhood  $G_{x,y}$  includes  $2\pi r^2$  pixels. Let the number of pixels belonging to *Class 1*, *Class 2*, *Class 3* and *Class 4* within the neighborhood  $G_{x,y}$ , be

denoted by  $v_1, v_2, v_3$  and  $v_4$ , respectively. The normalized feature vector  $\mathcal{V}$  corresponding to the pixel at  $(x, y)$  is defined as follows:

$$\mathcal{V}(x, y) = [v_{1,n}, v_{2,n}, v_{3,n}, v_{4,n}] \quad (3.2)$$

$$\text{where } v_{i,n} = \frac{v_i}{2\pi r^2}, \quad i = 1, \dots, 4.$$

In Figure 3.5 (a), the *Class 2* pixels are clustered together, and hence is more likely to be a lymph node tissue compared to Figure 3.5 (b), where the *Class 2* pixels are scattered. Therefore, we consider using a high frequency measure for  $G_{x,y}$  and use it as a feature to distinguish the scatteredness. The proposed frequency feature is also important to detect the other tissue regions, which are filled with holes and few parts of lymph node tissue. The following steps are used to calculate the High Frequency Measure (HFM) for each coarse classified pixel at coordinate  $(x, y)$ :

1. Consider the pixel  $(x, y)$  as the origin of its neighborhood  $G_{x,y}$ . For simplicity we denote  $G_{x,y}$  as  $G$ .
2. Unfold  $G$  matrix by converting it from polar coordinates into cartesian coordinates by arranging  $p$  radial lines (of length  $2r+1$ ) of  $G$  matrix which passes through the origin with angle  $m\pi/p$ ,  $0 \leq m \leq p-1$ . Arrange these radial lines as 2-D rectangular matrix  $\tilde{G}$  of size  $p \times (2r+1)$ , as follows:

$$\tilde{G} = \begin{bmatrix} \tilde{G}(1,1) & \cdots & \tilde{G}(1,2r+1) \\ \vdots & \ddots & \vdots \\ \tilde{G}(p,1) & \cdots & \tilde{G}(p,2r+1) \end{bmatrix}$$

3. Calculate the 2-D- Discrete Fourier Transform (DFT) of  $\tilde{G}$ .

$$G'(q, k) = \sum_{m=1}^p \sum_{n=1}^{2r+1} \tilde{G}(m, n) e^{-\frac{j2\pi kn}{2r+1}} e^{-\frac{j2\pi qm}{p}} \quad (3.3)$$

$$1 \leq q < p, \quad 1 \leq k < 2r+1$$

4. Calculate the HFM  $\mu$  as follows:

$$\mu(x, y) = \sum_{q=\frac{p}{4}}^{\frac{3p}{4}} \sum_{k=\frac{2r+1}{4}}^{\frac{3(2r+1)}{4}} \|G'(q, k)\| \quad (3.4)$$

where  $\|G'\|$  is the magnitude of  $G'$ , and the indices  $[\frac{p}{4} : \frac{3p}{4}, \frac{2r+1}{4} : \frac{3(2r+1)}{4}]$  are considered to represent the high frequency coefficients. Repeat steps 1-4 for all pixels in the image  $\varphi$  and calculate  $\mu$ .



Figure 3.6 shows the overall schematic of the  $\mu$  calculation. Figure 3.7 shows the HFM  $\mu$  corresponding to the image  $\varphi$  shown in Figure 3.4. The HFM shows three contrast regions: black, gray and white representing background, lymph nodes regions and other tissue regions, respectively.

The HFM  $\mu$  is not directly used in the proposed method. We apply a threshold on  $\mu$  and generate a binary HFM image  $\mu^b$  as follows:

$$\mu^b(x, y) = \begin{cases} 0 & \text{if } \mu(x, y) \leq \tau_{otsu} \\ 1 & \text{if } \mu(x, y) > \tau_{otsu} \end{cases} \quad (3.5)$$

where  $\tau_{otsu}$  is the Otsu threshold calculated by analyzing the pdf of  $\mu$ .

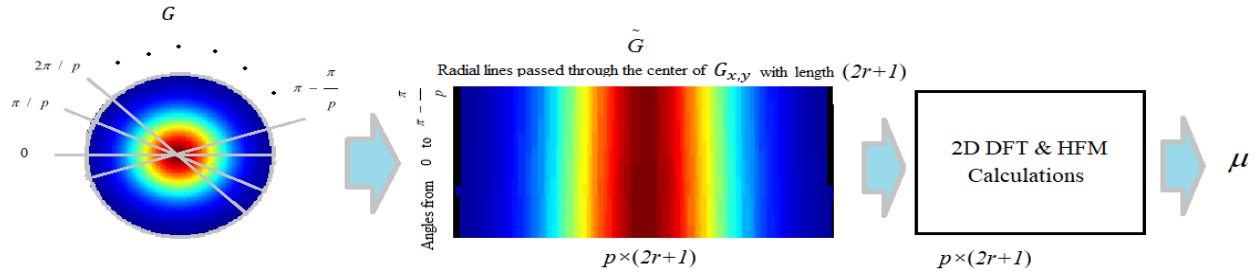


Figure 3.6. Schematic to calculate the HFM  $\mu$ .

Figure 3.8 (a) shows the binary HFM  $\mu^b$  obtained by thresholding Figure 3.7. Note that the white pixels correspond to the other tissue (OT) regions whereas the black pixels denote the LN as well as the background. It would be helpful to distinguish the LN from the background region. The binary HFM also includes many small noisy (white) regions. Therefore, we propose to generate another binary HFM feature which will coarse segment the HFM image into LN and non-LN regions. This is obtained using the following steps.

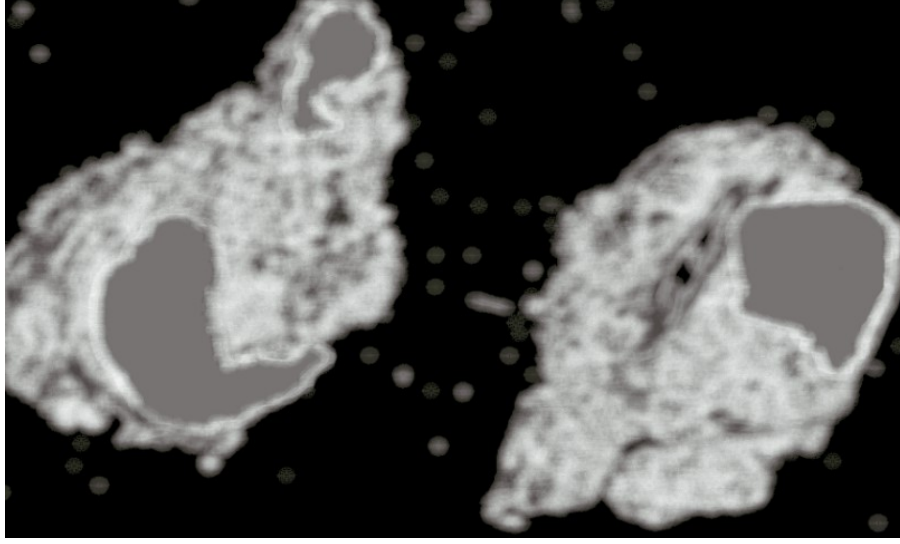


Figure 3.7. The HFM  $\mu$  for the classified image  $\varphi$  that is shown in Figure 3.4.

- (i) Note that the LNs appear as holes in the white background (consisting of OT regions). In the first step, we estimate the entire hole regions (i.e., all dark pixels surrounded by white pixels) in the image. In order to do this, the holes in  $\mu^b$  are filled by dilation using the following iterative equation.

$$\mu_k^{hf} = (\mu_{k-1}^{hf} \oplus S_1) \cap (\sim \mu^b) \quad k = 1, 2, 3, 4, \dots \quad (3.6)$$

where the initial hole-filled image  $\mu_0^{hf} = \mu^b$ . Note that  $\mu_k^{hf}$  is the hole-filled image after  $k$ -th iteration. The initial dilation with the structuring element  $S_1$  starts inside the black holes, and the iteration is terminated when  $\mu_k^{hf} = \mu_{k-1}^{hf}$  at  $k = \ell$  (the last iteration). In this Chapter, we have used the following structural element. Figure 3.8 (b) is an example of the hole-filled image.

$$S_1 = \begin{bmatrix} 0 & 1 & 0 \\ 1 & 1 & 1 \\ 0 & 1 & 0 \end{bmatrix}$$

- (ii) The hole regions filled up by Eq (3.6) is calculated as:

$$H = \mu_\ell^{hf} - \mu^b \quad (3.7)$$

Note that the hole filling might fill some background regions. Figure 3.8 (c) shows  $H$  obtained from Figure 3.8 (b).

- (iii) It is observed that  $H$  contains many noisy areas. An 8-connectivity analysis is applied on  $H$  to determine the number and the size of the disconnected regions. We remove the regions with small areas that satisfies the following criterion:

$$area(R) < \tau_{area} * A_m \quad (3.8)$$

where  $R$  is a disconnected region,  $A_m$  is the largest size of the disconnected areas in  $H$ , and  $\tau_{area}$  is a predetermined area thresholds parameter. The set of disconnected regions satisfying Eq. (3.8) is our initial estimate of the LN obtained from the HFM. Let these disconnected regions be denoted by  $L$ , and the number of regions be denoted by  $N_L$ .

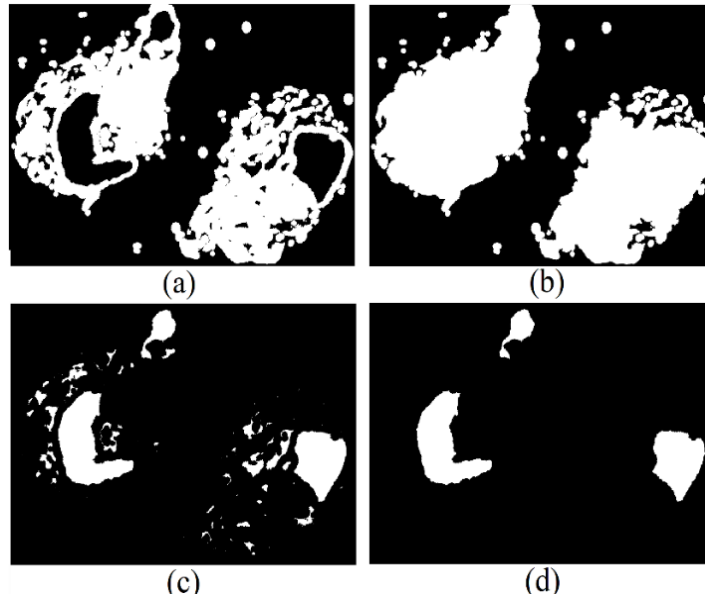


Figure 3.8. Images obtained by applying morphological operations on the image in shown Figure 3.4 (a)  $\mu^b$  obtained using Otsu threshold, (b)  $\mu_q^{hf}$  obtained after filling the holes, (c) Initial estimate of lymph node  $H$  and (d)  $L$  after removing small noisy regions.

The final feature vector for each pixel in the input image  $I$ , is obtained by combining the three features as follows:

$$f = \{v, \mu^b, L\} \quad (3.9)$$

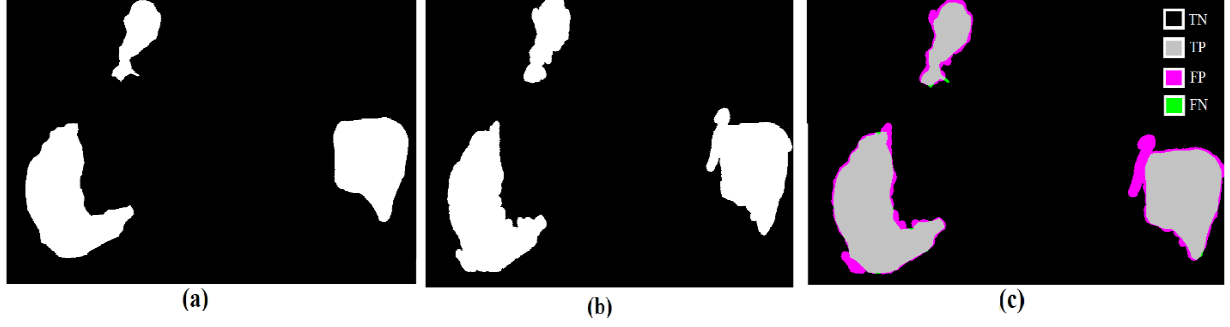


Figure 3.9. Masks generated from the image in Figure 3.4. (a) Ground truth mask (b) Mask generated by the proposed technique and (c) comparison of ground truth and segmented mask.

### 3.3.3. Fine Segmentation

In this section, the feature vector  $f$  (with dimension 6) for each pixel in the image  $\varphi$ , is classified using a Support Vector Machine (SVM). The fine segmentation is done by training the SVM model with binary classification. Let us assume that there are  $k$  training feature vectors  $\{f_1, f_2, \dots, f_k\}$  corresponding to  $k$  pixels which are selected from the training images. The SVM model is trained using these selected  $k$  feature vectors and the corresponding labels  $\{y_1, y_2, \dots, y_k\}$ . Note that, these labels are obtained from the ground truth information and each feature vector is labeled as (1) for lymph node tissue or (-1) for non-lymph node tissue. The SVM estimates the best hyperplane  $P$  to separate these labeled feature vectors with maximum margin by minimizing the following cost function:

$$\begin{aligned} \min_{w,b} \quad & \frac{1}{2} \|w\|^2 \\ \text{s.t.} \quad & (w^T f_j + b)y_j \geq 1, \quad j = 1, \dots, k \end{aligned} \quad (3.10)$$

where  $w$  is the normal vector to the hyperplane  $P$ ,  $f_j$  is the  $j$ th feature vector and  $y_j$  its label. The above quadratic programming problem is solved by using Lagrange Multipliers with inequality constraints to find  $w$  and  $b$  [54,55]. The hyperplane  $P$  is defined by  $w^T u + b = 0$ , where  $u$  is a point on the hyperplane  $P$ . Note that an SVM classifier can also be used to separate un-separable data by increasing the dimensionality with different kernels. During testing, the SVM model is used to classify a pixel into two classes: LN tissue and non-LN tissue. Using the classification, the LN mask  $\phi$  is calculated as follows:

$$\phi(x, y) = \begin{cases} 1 & \text{for } LN_{tissue} \\ 0 & \text{for } non - LN_{tissue} \end{cases} \quad (3.11)$$

### 3.3.4. Segmentation Performance

The proposed technique is evaluated with respect to objective measures such as Sensitivity, Precision, Specificity and Accuracy. Figure 3.9. compares the segmented LN mask  $\phi$  obtained by the proposed technique and the ground truth mask. It is observed that the LNs obtained by the proposed technique is very close to that of the ground truth. The performance of the proposed technique was evaluated using three SVM kernels: Linear, Polynomial and Gaussian kernel. Table 3.1. shows the performance comparison for different SVM kernels on our dataset. It is observed that the Gaussian kernel provides the best performance in terms of Sensitivity, Precision, Specificity and Accuracy. Therefore, all the results are obtained using the Gaussian kernel. Figure 3.10. shows examples of segmented Lymph nodes slides with different stains along with their ground truth masks. It is observed the segmented lymph nodes by proposed technique are very close to the ground truth mask. Figure 3.11. shows the Sensitivity, Precision, Specificity and Accuracy for each of the 39 images in the database. It is observed that the proposed technique provides an average sensitivity, precision, specificity, and accuracy of 95.33%, 90.12%, 93.52% and 95.03% respectively. In other words, the LN segmented performance is very good for most images. There are a few images where the sensitivity is somewhat low. For example, Figure 3.11. shows the WSI index 21, 24 and 36 have sensitivity around (80%). Visual inspection reveals that the low sensitivity mainly arises because of the WSI artifacts such as tissue folding, slide imperfections, lighting inconsistencies, and improper calibration of imaging equipment.

TABLE 3.1 PERFORMANCE OF THE PROPOSED TECHNIQUE USING DIFFERENT SVM KERNELS.

Kernels	Sensitivity	Precision	Specificity	Accuracy
Linear	90.30	82.19	91.84	93.43
polynomial	89.56	87.14	92.67	94.20
Gaussian	95.33	90.12	93.52	95.03

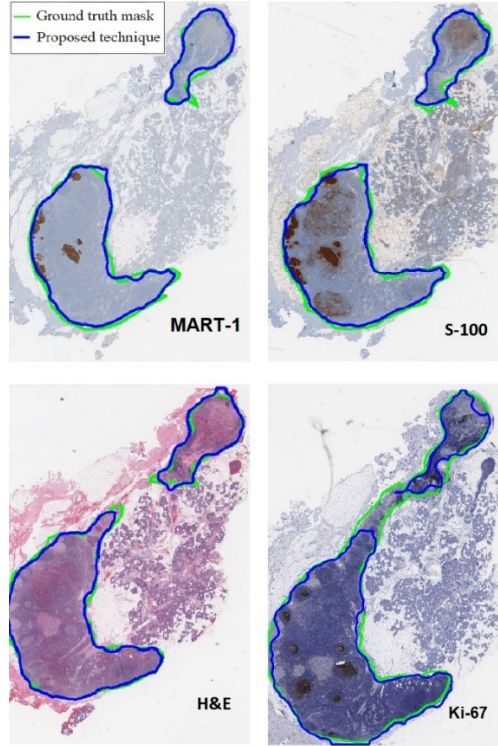


Figure 3.10. Lymph node images with different stains (a) S-100, (b) H&E, (c) Ki-67, and (d) MART-1.

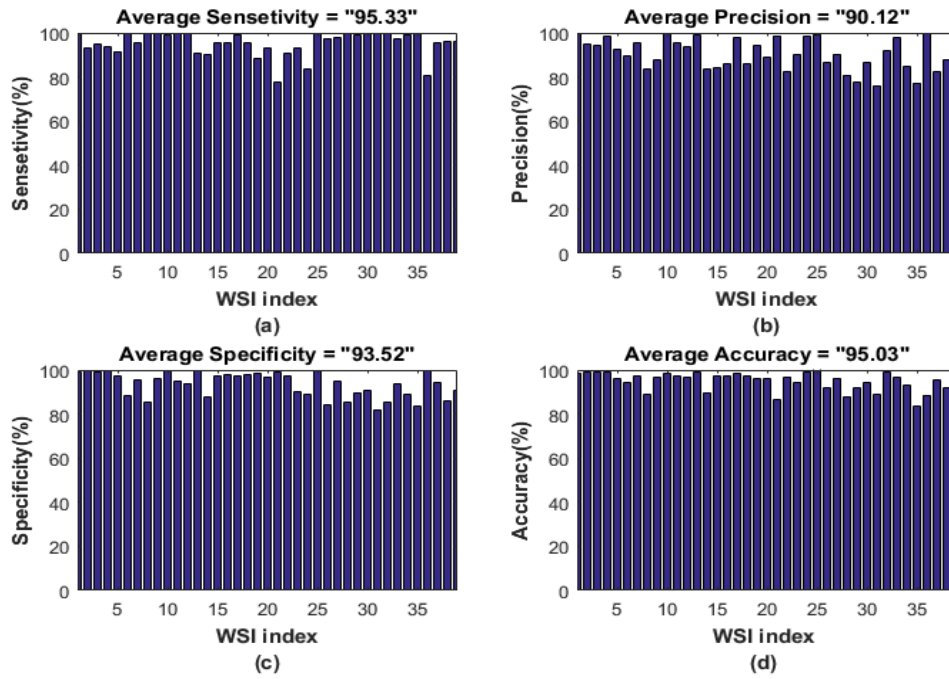


Figure 3.11. Segmentation performance of the proposed technique for different image. (a) Sensitivity, (b) Precision, (c) Specificity, and (d) Accuracy.

### 3.4. Proliferation Index Calculation

In this section we measure the Proliferation Index ( $PI$ ) which is calculated as follows:

$$PI = \frac{NA}{NP + NA} \times 100\% \quad (3.12)$$

where  $NA$  and  $NP$  are the number of the active and passive nuclei, respectively. In this Chapter, we calculate three types of  $PI$  values for melanoma as follows:

- The average  $PI$  value for the entire melanoma region.
- The average  $PI$  value for each individual region.
- The  $PI$  values for a given number (e.g., 3) of windows with size around  $(0.15 \times 0.1) \text{ mm}^2$ .

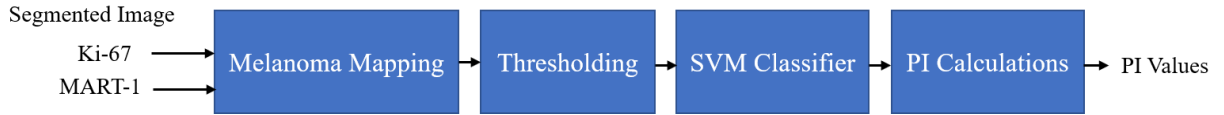


Figure 3.12. Schematic of the proliferation index  $PI$  calculation.

For a lymph node in Ki-67-stained image, we use MART-1-stained image to detect the melanoma regions which appear with brown color. Figure 3. 12 shows the schematic to calculate the  $PI$  values for the melanoma regions. It is observed that, there are four modules for  $PI$  calculations, which are detailed below.

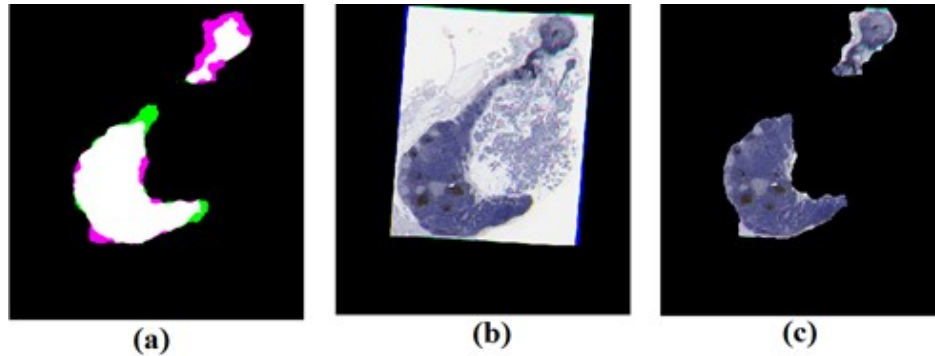


Figure 3.13. Image registration for MART-1 and Ki-67-stained images for the same lymph nodes. (a) overlapped masks  $\phi_M$  and  $\phi_K$  after registration, (b) image  $I'_K$ , and (c) image  $I''_K$ .

#### 3.4.1. Melanoma Mapping

This module takes the segmented MART-1 and Ki-67-stained images (obtained using the technique proposed in section 3.2) as inputs. The melanoma regions of MART-1-stained image are mapped into affine transformed Ki-67-stained images using the following two steps.

Step-1 Ki-67 Transformation: Let the MART-1 and Ki-67-stained images be denoted by  $I_M$  and  $I_K$ , respectively. Let the binary LNs masks of  $I_M$  and  $I_K$  be denoted by  $\phi_M$  and  $\phi_K$ , respectively. Figure 3.10 (a) shows the MART-1 image  $I_M$  and its LN mask  $\phi_M$  (blue contour). On the other hand, Figure 3.10 (d) shows Ki-67 image  $I_K$  and its LN mask  $\phi_K$  (blue contour). In this step, we first register the LN masks  $\phi_M$  and  $\phi_K$  where the mask  $\phi_M$  is kept fixed and the mask  $\phi_K$  is transformed. The registration is achieved by finding the best transformation  $t'$  that will align the lymph node masks  $\phi_M$  with  $\phi_K$  in the same coordinate system. The transformation  $t'$  is obtained by solving the following equation.

$$t' = \arg \max_t (\lambda(\phi_M(X), \phi_K(X))) \quad (3.12)$$

where  $\lambda(\cdot)$  is the mutual information and  $t(x)$  is the affine transformation of the coordinate  $x$ . The mutual information of the two masks  $\phi_M$  and  $\phi_K$  is calculated as follows:

$$\lambda(\phi_M, \phi_K) = e(\phi_M) + e(\phi_K) - e(\phi_M, \phi_K) \quad (3.13)$$

where  $e(\phi_M)$  and  $e(\phi_K)$  are the entropies of mask  $\phi_M$  and  $\phi_K$ , respectively, and  $e(\phi_M, \phi_K)$  is the joint entropy. The entropies are calculated based on the probability density function (PDF) of the pixel values  $[0,1]$  of the entire 2D images  $\phi_M$  and  $\phi_K$ , and the joint entropy is calculated based on the joint PDF of  $\phi_M$  and  $\phi_K$ . Figure 3.13 (a) shows the overlapped masks of  $\phi_M$  (white & purple regions) and  $\phi_K(t'(X))$  (white & green regions). After obtaining the optimal  $t'$ , we apply the affine transformation  $t'(X)$  on  $I_K$  as follows.

$$I'_K = I_K(t'(X)) \quad (3.14)$$

where  $I'_K$  is the affine transformed Ki-67 stained image (see Figure 3.13 (b)). The lymph nodes regions in  $I'_K$  masked by  $\phi_M$  is calculated below:

$$I''_K = I'_K * \phi_M \quad (3.15)$$



where  $I_K''$  is LN regions in the affine transformed Ki-67-stained image  $I_K'$  as shown in Figure 3.14 (c). Note that  $I_K''$  corresponds to the LNs of Ki-67 image that is also registered with the corresponding MART-1 image.

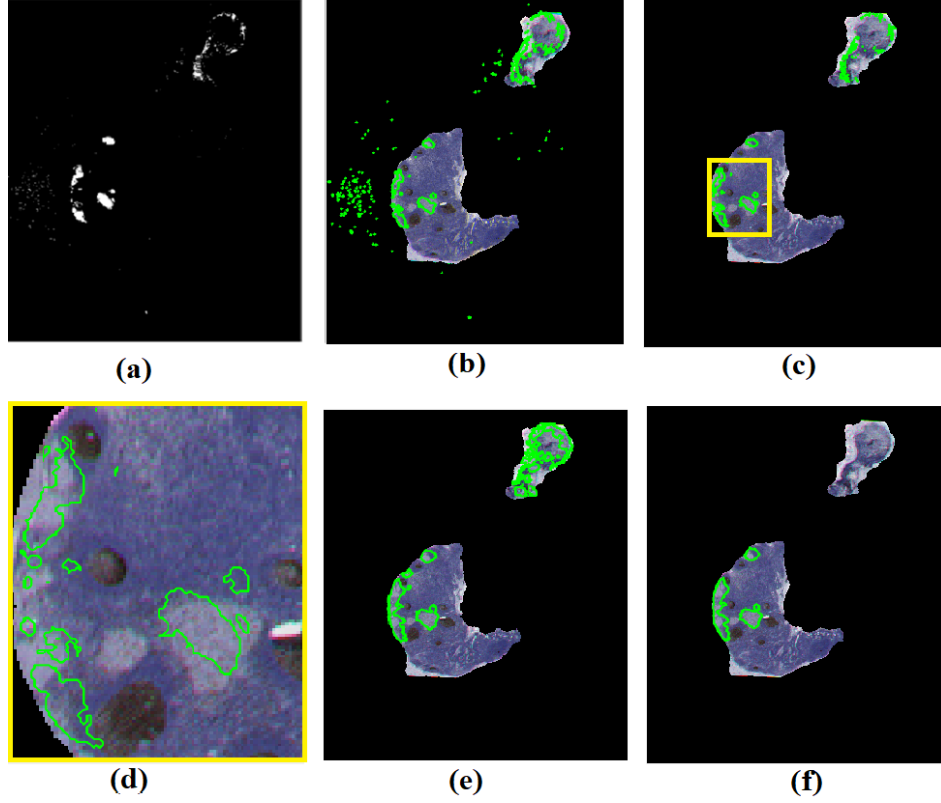


Figure 3.14. Melanoma mapping process (a) Melanoma mask  $\delta$  of MART-1, (b)  $\delta'$  contour melanoma regions (green color) in  $I_K''$  image, (c)  $\delta'$  contour melanoma regions (green color) in  $I_K''$  image, (d) The magnified image of yellow square in  $\delta'$ , (e)  $\delta''$  contour melanoma regions (green color) in  $I_K''$  image and (f) The final melanoma mask.

Step-2 Melanoma Mask: In order to calculate the PI, we also need a mask for the melanoma regions. In this work, the melanoma region mask  $\delta$  is generated (for MART-1 only) as follows:

$$\delta(x, y) = \begin{cases} 1 & \text{for } MN \text{ tissue} \\ 0 & \text{for } non - MN \text{ tissue} \end{cases} \quad (3.16)$$

where  $\delta$  is the *Class 1* pixels obtained from coarse segmentation model (see Eq. 3.1).

Figure 3.14 (a) shows the MN regions  $\delta$  (with green contour) obtained for MART-1 image  $I_M$ . Figure 3.14 (b) shows the mask  $\delta$  superimposed on  $I_K''$ . It is observed that some noisy melanoma areas are outside the lymph nodes. These outside noisy areas are removed using the LN mask  $\phi_M$ , and the de-noised mask is shown in Figure 3.14 (c). A magnified version of the yellow square in

Figure 3.14 (c) is shown in Figure 3.14 (d), and it is observed that there are small, disconnected MN regions inside the LN regions. We apply the following steps to connect these small regions and refine the MN mask  $\delta$ :

1. An Active Contour Model (ACM) is applied on the melanoma contour to merge the small, disconnected regions and make the melanoma mask smoother. The refinement of melanoma contour is driven by two forces: an internal force that keeps the contour smooth, and an external force that pushes it towards the object contour. The active contour model based on a gradient vector flow (Xu and Prince, 1998 [77]) is used in the proposed system for melanoma contour refinement. The melanoma contour denoted by  $\mathbf{x}(s)$ , is obtained by minimizing  $E$  as defined below:

$$E = \int_0^1 [E_{ext} + E_{int}] ds$$

where  $\mathbf{x}(s) = [x(s), y(s)]$ ,  $s \in (0, 1)$ . The internal energy  $E_{int}$  is calculated as follows:

$$E_{int} = \frac{1}{2} \int_0^1 |\mathbf{x}'(s)|^2 ds$$

where  $\mathbf{x}'(s)$  and  $\mathbf{x}''(s)$  are the first and second derivatives of  $\mathbf{x}(s)$ , respectively, and  $\alpha$  and  $\beta$  are weighting parameters. The external energy  $E_{ext}$  of the contour is calculated as follows:

$$E_{ext} = \int \int [\gamma(u_x^2 + u_y^2 + v_x^2 + v_y^2) + |\nabla f| |k - \nabla f|^2] dx dy \quad (3.17)$$

where  $k = (u(x, y), v(x, y))$  is the gradient vector flow,  $f$  is the gradient of the smoothed image  $I_K''$  as the edge map,  $\{u_x, u_y, v_x, v_y\}$  are the partial derivatives with respect to  $x$  and  $y$ . Figure 3.14 (e) shows the melanoma regions after applying the ACM. Let the obtained melanoma mask be denoted by  $\delta'$ , and the disconnected region in  $\delta'$  be denoted by  $R_i$  ( $i = 1, 2, \dots, N_{DR}$ ) where  $N_{DR}$  is the number of disconnected candidate melanoma regions. It is observed in Figure 3.14 (c) that there is a large number of  $R_i$  ( $N_{DR}=116$ ).

2. The mask  $\delta'$  is a smooth version of the mask  $\delta$ , but there are a few regions of melanoma that expand on lymph melanoma regions due to ACM. In this step, we refine  $\delta'$  by removing regions that are not melanoma. This done as follows: Convert the color image  $I_M$  into a gray intensity image  $I_{gM}$ . Map  $\delta'$  onto  $I_{gM}$ , and calculate the mean intensity of each of the  $N_{DR}$  melanoma regions in  $I_{gM}$ . Note that the melanoma regions are typically brown and have a low mean intensity. Hence, a region  $R_i$  is removed from  $\delta'$  if the corresponding mean intensity satisfies the following.

$$MeanIntensity(R_i) > \tau \quad (3.18)$$

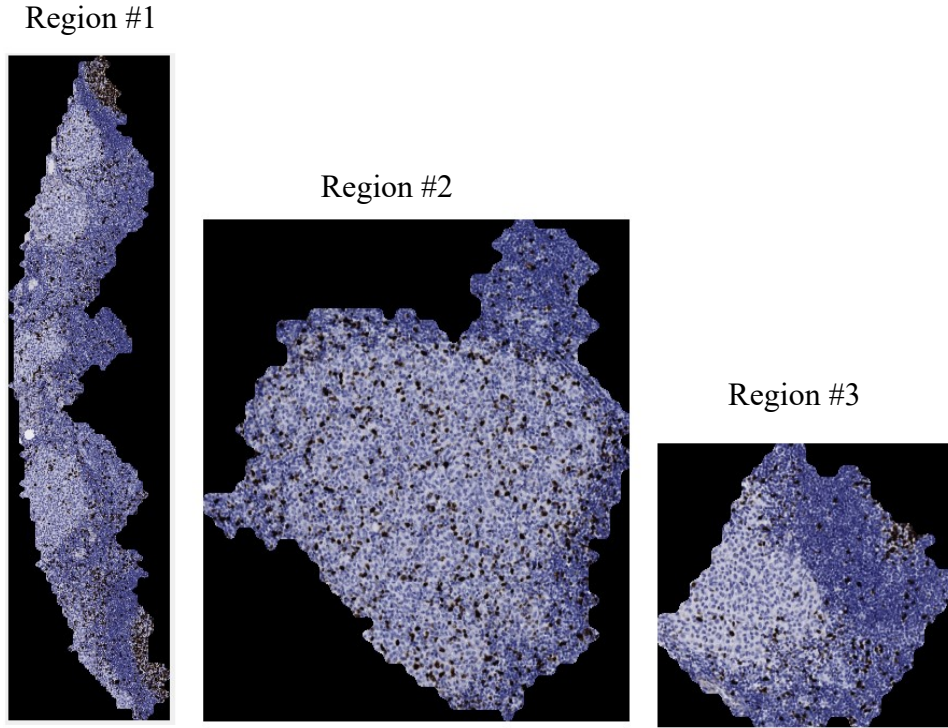


Figure 3.15. The magnified version of melanoma regions in Ki-67 image (obtained from Figure 3.13(f)).

where  $\tau$  is a threshold. Let the final melanoma mask be denoted by  $\delta''$ , and let the number of remaining disconnected regions be denoted by  $N'_{DR}$ . It is observed in Figure 3.15 (f) that there are three final melanoma regions (i.e.,  $N'_{DR} = 3$ ). The magnified version of these regions is shown in Figure 3.15.

### 3.4.2. Thresholding

Figure 3.15 shows the melanoma regions in  $I''_K$ , denoted by  $\mathfrak{R}_i$  ( $i = 1, 2, \dots, N'_{DR}$ ). We now want to segment each of these regions into two classes: nuclei (*Class-1*) and background (*Class-2*). In this

module, we use Otsu thresholding technique to perform the segmentation. A pixel located at  $(x, y)$  in region  $\mathfrak{R}_i$  is classified as follows:

$$\mathfrak{R}_i^n(x, y) = \begin{cases} \mathfrak{R}_i(x, y) & \text{if } \text{gray}(\mathfrak{R}_i(x, y)) \leq \lambda_i \\ 0 & \text{if } \text{gray}(\mathfrak{R}_i(x, y)) > \lambda_i \end{cases} \quad (3.19)$$

where  $\mathfrak{R}_i^n$  is the nuclei image,  $\text{gray}(\mathfrak{R}_i(x, y))$  is the gray intensity of the color pixel  $\mathfrak{R}_i(x, y)$ , and  $\lambda_i$  is the Otsu threshold for  $\text{gray}(\mathfrak{R}_i)$ . Note that in Eq. 3.19, the background pixels with gray value greater than  $\lambda_i$  in  $\mathfrak{R}_i^n$  has been set to zero. Figure 3.16 shows the nuclei image for melanoma regions, where the *background* appears in black (i.e., zero intensity).

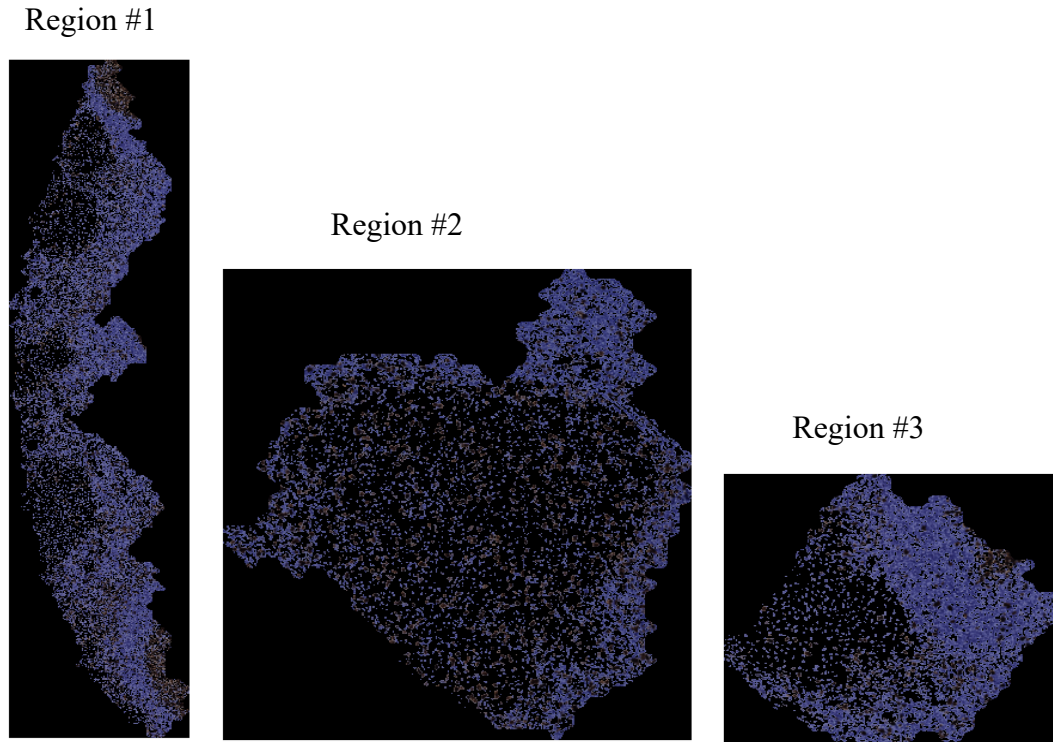


Figure 3.16. Nuclei mask for all melanoma regions using Otsu threshold.

### 3.4.3. SVM Classifier

In this module, we train an SVM model with linear kernel to segment the nuclei regions  $\mathfrak{R}_i^n$  into active nuclei (dark brown pixels) and passive nuclei (blue pixels). The RGB values of a pixel are used as features, and the ground truth classification labels (i.e., active or passive) are manually obtained for each color pixel in  $\mathfrak{R}_i^n$ .

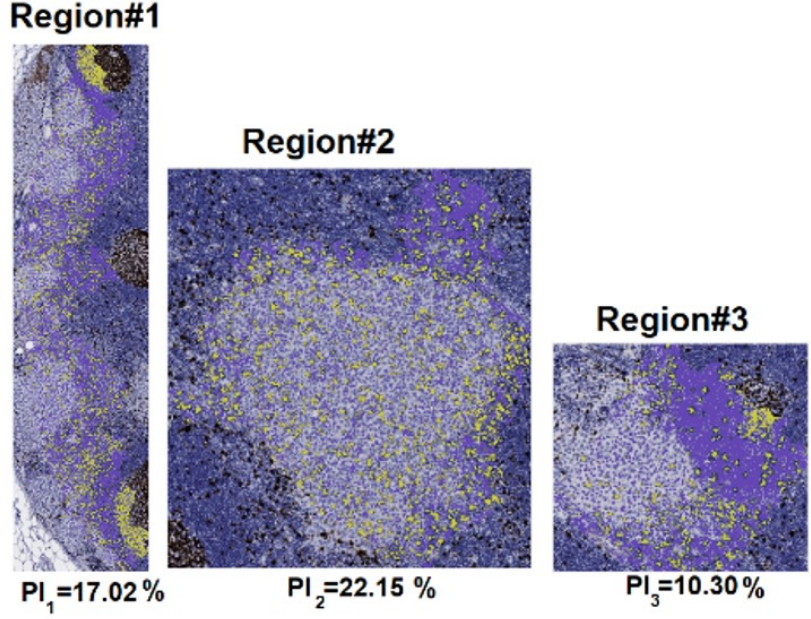


Figure 3.17 Classified nuclei image for all melanoma regions, where yellow and purple represent the active and passive cells respectively.

The SVM model is trained using feature vector and classification label of pixels in the training images. The SVM model estimates the best hyperplane that separates the nuclei into active and passive nuclei. Let the SVM parameters be denoted by  $w$  and  $b$  (see Eq. 3.10). The classification of a nuclei pixel ( $j$ ) is done as follows.

$$pixel(j) = \begin{cases} Active & \text{if } (w^T f_j + b) > 0 \\ Passive & \text{if } (w^T f_j + b) \leq 0 \end{cases} \quad (3.20)$$

where  $f_j$  is the feature vector corresponding pixel  $j$ . Several images were used to train the SVM to estimate the best SVM parameters. Figure 3.17 shows the SVM classification results, where the active and passive nuclei are shown in yellow and purple color, respectively. The SVM model presents a good performance for nuclei classification due to the strong difference between the brown and blue colors in RGB representation.

### 3.4.4. PI Calculation

In the current practice, the pathologists typically calculate the PI values in a few small windows where there is a high concentration of active nuclei. This is primarily because of the difficulty of PI calculation using manual methods. In this work, as the PI is calculated automatically, the following three types of  $PI$  values are calculated to give more information to the pathologists:



- (i) One PI for each individual melanoma region  $\mathfrak{R}_i$ . Let the  $PI$  value of region  $\mathfrak{R}_i$  be denoted by  $PI_i$ .
- (ii) The average  $PI$  value for the entire melanoma region of the lymph node. Let this  $PI$  be denoted by  $PI_E$ .
- (iii) The  $PI$  values for a few windows with the largest concentration of active nuclei. If  $K$  windows are selected, let the  $PI$  be denoted by  $PI_{W,k}$ ,  $k = 1, 2, \dots, K$ .

We first calculate the  $PI_i$  values for all individual melanoma regions  $\mathfrak{R}_i$  using Eq. (10). Figure 3.18 shows the  $PI_i$  value for each of the three individual melanoma regions. For the entire melanoma region, the  $PI_E$  value is calculated as follows:

$$PI_E = \frac{NA_{all}}{NP_{all} + NA_{all}} \times 100\%$$

where  $NA_{all}$  and  $NP_{all}$  are the numbers of the active and passive nuclei, respectively, in the entire melanoma regions. For the lymph node in Figure 3.10 (c), the  $PI_E$  value is obtained as 19.82%. The  $PI_{W,k}$  ( $k = 1, 2, \dots, K$ ), values are calculated for the dense active nuclei window automatically as follows: Figure 3.18 shows three windows in red contour with high  $PI$  values:  $PI_{W,1} = 22.59\%$ ,  $PI_{W,2} = 19.98\%$ ,  $PI_{W,3} = 24.83\%$ .

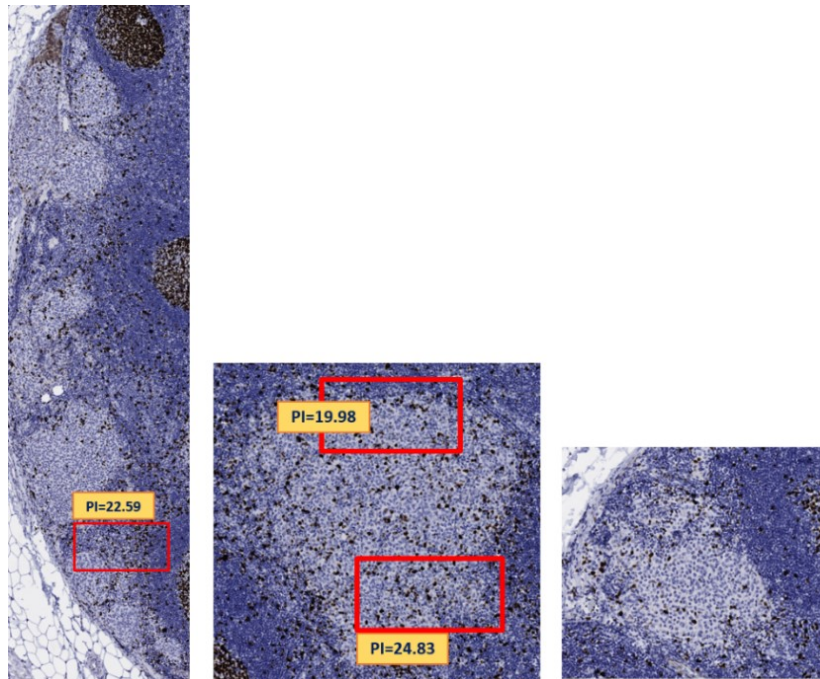


Figure 3.18. The  $PI$  values for each window (in red contour) for melanoma regions.

### 3.4.5. Performance Evaluation

In this section, we evaluate the performance of the nuclei segmentation and PI calculation with following parameters (as shown in Table 3.2).

TABLE 3.2 PI CALCULATION PARAMETERS.

Window size	0.15x0.1 mm <sup>2</sup>
$\tau$ (the normalized melanoma threshold in $\delta'$ )	0.5
$K$ (number of the windows)	3

Figure 3.19 (a) shows a selected window of a Ki-67 image of a lymph node. The thresholded image is shown in Figure 3.19 (b) where the white pixels represent nuclei and black pixels represent the background. The nuclei pixels (both active and passive), obtained using Eq. (3.20), are shown in Figure 3.19 (c). The classified nuclei, obtained using the SVM model, are shown in Figure 3.19 (d), where the active and passive nuclei are represented by red, and blue color (the background pixels are shown in green). It is observed that the active and passive nuclei are efficiently classified to obtain the PI values.

The performance of the proposed technique is compared with the FCM+KM technique proposed by Mungle *et al* [63]. The FCM and K-means functions available in the MATLAB toolbox, with two clusters, were used to evaluate the FCM+KM technique. For FCM, a threshold of 0.5 was used for the nuclei segmentation. After K-means clustering, all active nuclei candidates with an area less than 600 pixels (physical area: 0.125 mm<sup>2</sup>) were considered as noisy areas and not used for PI calculation. The PI calculation is performed using window size of 1920 × 2500 pixels (physical dimension: 0.238 × 0.310 mm<sup>2</sup>) on a Ki-67 image scanned with 20X magnification. Figure 3.20 shows the PI values of 12 image windows, obtained by using the FCM+KM and the proposed techniques, along with the ground truth PI values. Table 3.3. compares the Root Mean Square Error (RMSE), Mean absolute Error (MAE) of the obtained PI values (compared to the ground truth).

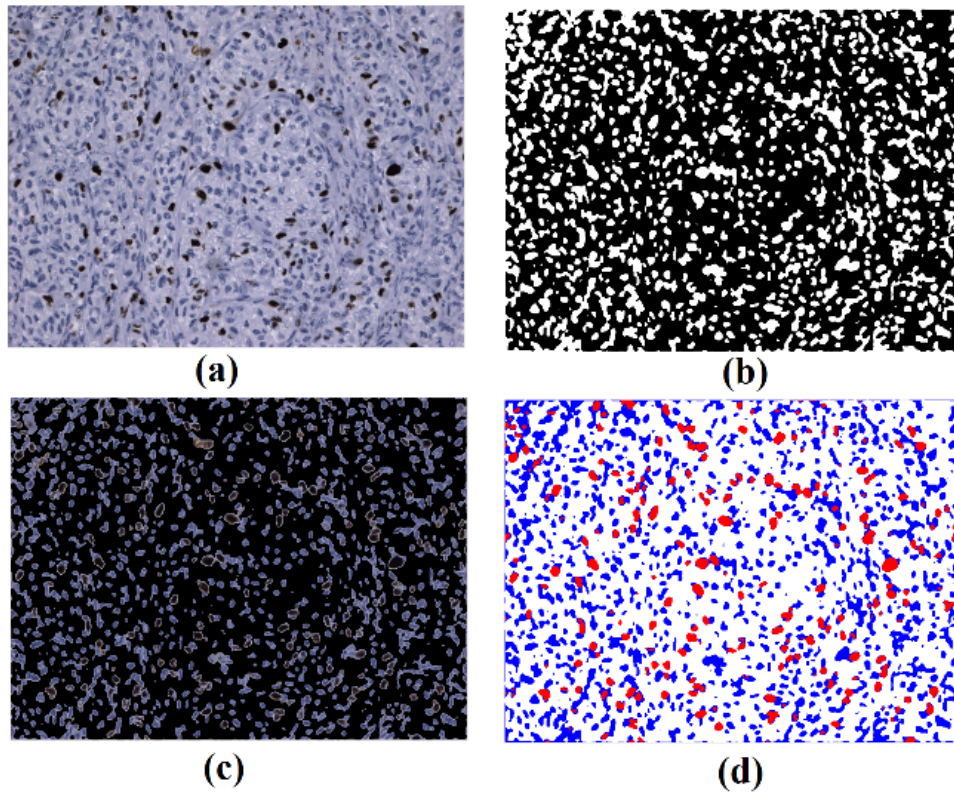


Figure 3.19. Intermediate results of the proposed technique (a) The Ki-67-stained image (b) Otsu mask, (c) the nuclei mask and (d) the segmentation results using SVM, where the active and passive nuclei are shown in red and blue, respectively.

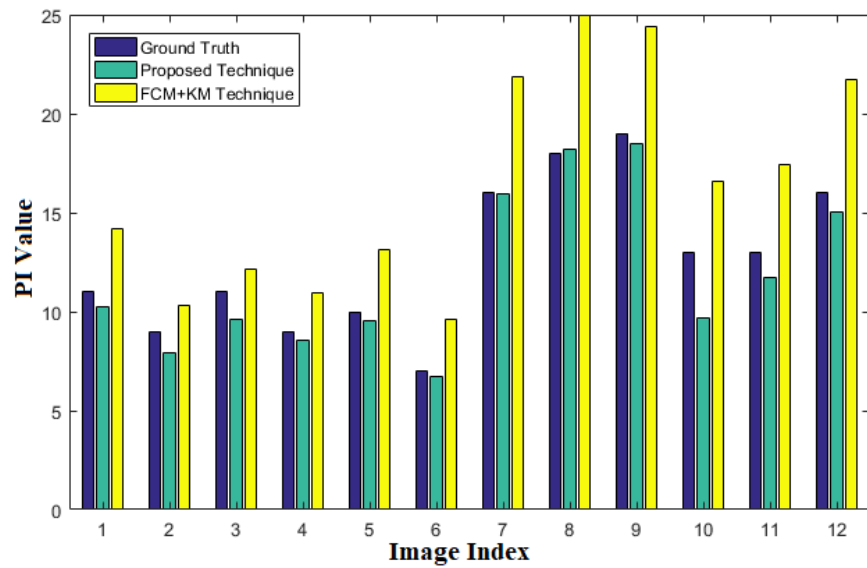


Figure 3.20. Performance comparison of the proposed Technique (in green bars) and the FCM+KM [19] technique (in yellow bars). The Ground Truth is shown in blue bars.



It is observed that the proposed technique provides a superior performance compared to the FCM+KM technique. A possible reason for the superior performance may be that the proposed technique uses supervised SVM classifiers whereas the FCM+KM technique uses the unsupervised K-means method, which may not be very effective.

Table 3.3. also compares the execution time for the proposed technique and the FCM+KM technique. It is observed that the proposed *PI* technique is about 20 times faster compared to the FCM+KM technique.

TABLE 3.3.

PI CALCULATION PERFORMANCE OF PROPOSED AND FCM+KM TECHNIQUES.

Technique	RMSE	MAE	Execution time (in s)
FCM+KM [63]	4.20	3.76	298.20
Proposed PI	1.25	0.89	15.74

### 3.5. Conclusions

This Chapter proposes a fully automated technique for lymph node segmentation and proliferative index calculation in lymph node histopathological images. The technique uses local frequency features and SVM classifier for lymph node segmentation in biopsy images stained with H&E, Ki-67, MART-1, and CD-45. The technique then identifies the melanoma region in the Ki-67 image based on the MART-1 image characteristics of the same lymph node. Thresholding and SVM classification are then used to determine active and passive nuclei. The technique then calculates PI value of the entire melanoma region, individual melanoma region as well as for a few windows with high concentration of active nuclei. Experimental results show that the technique provides an excellent performance in terms of both lymph node segmentation and PI calculation.

# Chapter 4

## Automated Proliferation Index Calculation for Skin Melanoma Biopsy Images using Machine Learning

The Proliferation Index (PI) is an important diagnostic parameter used for staging different types of cancer (e.g., breast, lung and skin). This Chapter presents an automated technique to measure the PI values for skin melanoma images using machine learning algorithms. The proposed technique first analyzes a MART-1 stain histology image and generates a region of interest (ROI) mask for the tumor. The ROI mask is then used to locate the tumor regions in the corresponding Ki-67-stained image. The nuclei in the Ki-67 ROI are then segmented and classified using a Convolutional Neural Network (CNN), and the PI value is calculated based on the ratio of the active and the passive nuclei areas. Experimental results show that the proposed technique can robustly segment (with 94% accuracy) and classify the nuclei with a low computational complexity and the calculated PI values have an average error rate less than 5%.

### 4.1. Introduction

Skin cancer is the most common cancer type in North America, and it can be of different types such as Merkel cell carcinoma, sebaceous carcinoma, basal cell carcinoma and melanoma. Among these, the melanoma is the deadliest type with high mortality, and it can spread to any part of the body. As per recent statistics, it is estimated that about 100,350 new cases of melanoma cancer will be diagnosed resulting in about 6,850 deaths in 2020 in the United States alone [78]. Melanoma occurs when the melanocytes, located around the junction of the epidermis and the dermis layers in the skin, start growing aggressively to form malignant melanoma. The aggressive growth of melanocytes is mainly caused by the DNA replication due to the excessive exposure of the ultraviolet radiation (emitted from the sun). Once it is established that melanoma has invaded the epidermis, dermis and subcutaneous layer (in skin), doctors examine the lymph nodes closest to the tumor, known as the Sentinel Lymph Nodes (SLNs) to determine the spread. Through lymph vessels, the malignant melanoma can be drained from the skin to the SLNs and is passed on to other organs. The early detection, diagnosis, and staging of melanoma can increase the survival

rate up to 92% after five years when the cancer is found [23]. The melanoma staging is typically done by calculating the cell Proliferation Index (PI) of the tumor regions. The PI can determine the tumor evolution, which can help physicians to determine the effective treatment [78]. The PI is determined by estimating the ratio of the number of active cell nuclei and the total number of cell nuclei. During cell proliferation, the cell nuclei become active and start replicating the nuclei DNA and cytoplasm. A nuclear protein known as Ki-67 protein can be expressed strongly with cell proliferation. Doctors typically use Ki-67 markers to stain this protein to detect the positive response of cell nuclei on the tumor regions [75]. A stained skin tissue slide is digitized and diagnosed by a pathologist. In the Ki-67-stained image, the positive response of the active cells to the Ki-67 marker appears as dark brown color, whereas other cells appear as blue color (see Figure4. 1). A pathologist usually chooses the high proliferative areas in the tumor regions and manually calculates the PI values by counting the proportion of the active cells. The manual detection of the tumor regions, finding the high proliferative areas and calculating the PI values in a Whole Slide Image (WSI) can be labor and time intensive. In addition to the large size of WSIs, the manual analysis is also subjected to intra- and inter-observer variability [79]. Therefore, automated Computer-Aided Diagnosis (CAD) algorithms can provide a fast and reliable diagnosis [52]. A few techniques have been proposed in the literature to calculate the PI values in Ki-67-stained images for different types of cancers. The PI calculation is generally done by segmenting and/or detecting the nuclei (both active and passive nuclei). The nuclei segmentation and detection are difficult in Ki-67 images, as most cells lose the blob shape and have heterogeneity in color representation.

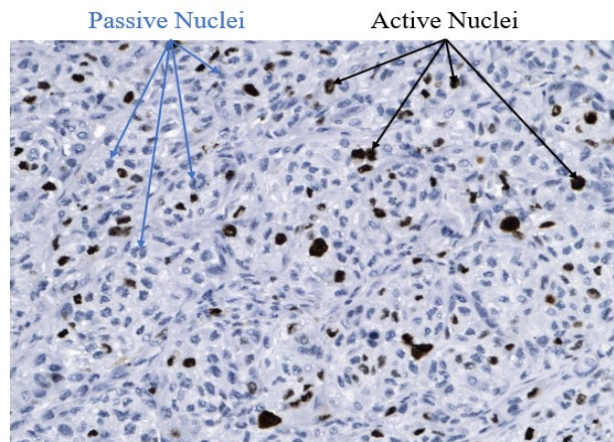


Figure 4.1. Histopathological image obtained with Ki-67 stain.

To calculate PI values, several researchers used thresholding algorithms for cells segmentation followed by a classifier. Grala et al. [60] proposed sequential thresholding to segment the cells and Support Vector Machine (SVM) to classify them into active and passive cells. Akakin et al. [61] used watershed algorithm and Laplacian-of-Gaussian filters to enhance the cell segmentation. Al-Lahham et al. [62] proposed a technique to segment and classify the cells into active/passive nuclei by applying K-means algorithm on the image pixels in  $L^*a^*b^*$  color-space. Mungle et al. [63] proposed an algorithm to segment the cells using a Fuzzy C-means (FCM) technique and then apply the K-means (KM) algorithm for classification (henceforth referred to as FCM+KM technique). Alheejawi et al. [80] proposed an automated algorithm to calculate the PI values on the tumor regions in Ki-67 images. The algorithm determined the tumor regions by mapping the segmented melanoma areas from MART-1 onto Ki-67 image. The PI values in this technique are calculated by segmenting the cells using the Otsu threshold and then classifying the active/passive nuclei using a SVM (henceforth referred to as the Otsu+SVM technique). With the recent advances in Machine Learning (ML) algorithms, the convolutional neural networks (CNN) have become popular for medical image segmentation and classification. Long et al. [66] proposed a CNN architecture for the semantic segmentation with several convolutional layers and a few max pooling layers followed by one upsampling layer. This architecture shows the segmented objects with coarse boundaries/edges due to the information lost in the pooling layers. Badrinarayanan et al. [67] proposed a CNN architecture (popularly known as SegNet) by adding several upsampling layers and enhanced them by transferring the maximum value indices of the corresponding pooling layers. Ronneberger et al. [81] proposed a CNN architecture, popularly known as UNet, to improve medical image segmentation by concatenating the upsampling layers (at the decoder side) with the corresponding features maps from the pooling layers (at the encoder side). Chen et al. [82] proposed a CNN architecture (known as DeepLabV3) for object segmentation, which contains several dilated separable convolutional layers, spatial pyramid pooling, and a few residual connections [83]. Although the DeepLab architecture has been shown to provide a good segmentation performance, it has high computational complexity due to the large number of layers. In addition, pooling layers in the DeepLab may degrade the segmented object boundaries especially in medical images. Saha et al. [84] proposed a technique (henceforth referred to as the GMM+CNN technique) to calculate PI values in breast cancer biopsy. Here, a few Ki-67 image windows with dense active nuclei are manually selected for the PI calculation. This technique uses

a Gaussian Mixture Model (GMM) with expectation-maximization algorithm to detect the nuclei seeds. Image patches around the isolated nuclei seeds are then classified into passive/active nuclei using a CNN classifier. The CNN uses 5 convolutional layers followed by two fully connected layers. In addition to the high computational complexity of the nuclei detection, the technique can calculate the PI values only for the isolated cell nuclei, which typically increases the error rate. Alheejawi et al. [85] proposed an automated technique (henceforth referred to as the PI-SegNet technique) to calculate the PI values for the melanoma regions using SegNet architecture, which contains 8 convolutional, 2 pooling, and 2 un-pooling layers followed by a softmax layer. The pooling layers can degrade the segmentation performance. In this Chapter, a fully automated CNN-based technique is proposed to calculate the PI value in a WSI. The proposed technique first generates a region of interest (ROI) mask in a MART-1 image based on color histogram analysis, and the mask is mapped onto the corresponding Ki-67 image to identify the melanoma region. The nuclei in the Ki-67 image are then segmented and classified using a CNN architecture, and PI values are calculated based on the proportion of active and passive nuclei areas. Experimental results demonstrate high accuracy and low error rate of the calculated PI values compared to the state-of-the-art techniques. The organization of the Chapter is as follows. Section 4.2. describes the dataset used to train and evaluate the proposed algorithm; Section 4.3. describes the proposed technique in detail. The performance evaluation of the proposed technique is presented in Section 4.4 followed by the conclusion in Section 4.5.

## **4.2. Data Description**

In this study, 10 pairs of histopathological images (from 10 different patients), obtained using MART-1 and Ki-67 stains, were collected from the Cross-Cancer Institute, University of Alberta, Canada in accordance with the protocol for the examination of patients with melanoma cancer. The histopathological slides were digitized under 40X magnification using biopsy scanner. The obtained WSIs are with size around 60,000×31,000 pixels (15mm x 7.75mm area with 0.25  $\mu\text{m}$ /pixel resolution). Each WSI contains several lymph nodes, and some of these lymph nodes contain 1-4 melanoma regions. Seven non overlapping windows (i.e., ROIs) with size 704x1280 color pixels are obtained from the lymph node regions of each Ki-67 stained WSI. In other words, a total of 70 windows are obtained from 10 WSIs, which form the dataset for performance evaluation. As the dataset is small, five-fold cross validation is used for performance evaluation in

this Chapter. For each fold, two WSIs are arbitrarily chosen as the testing WSIs, and 14 ROI windows from these two WSIs are used as the testing dataset. The remaining 56 ROI windows (from the other 8 WSIs) are used as the training dataset. This process is repeated five times for the five-fold cross validation, and five sets of performance measures are obtained. The average performance is reported in Section 4.4.

### 4.3. Proposed Technique

The schematic of the proposed technique is shown in Figure 4.2. The proposed technique consists of three modules: Melanoma Region Identification, CNN-based segmentation and PI calculation. The details of each module are presented in the following.

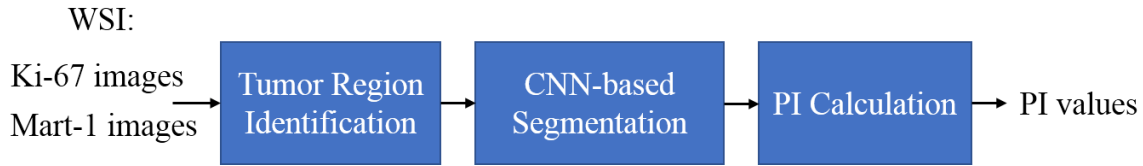


Figure 4.2. Schematic of the proposed segmentation technique.

#### 4.3.1. Tumour Region Identification

The PI values are calculated only within the melanoma regions in the Ki-67 images. The objective of this module is to identify the melanoma regions in Ki-67-stained lymph node image with the help of MART-1-stained image of a consecutive section [80]. The melanoma regions appear in brown color in MART-1 stain. These regions are segmented and superimposed on Ki-67 images to identify the tumor regions in Ki-67 images. Figure 4.3 (a) shows two lymph nodes in MART-1 and the melanoma regions appear in brown color. Figure 4.3 (b) shows the mapped melanoma regions in green contour on the Ki-67 image. Let the melanoma regions on Ki-67-stained image be denoted by  $R_i$  ( $i = 1, 2, \dots, N_{DR}$ ) where  $N_{DR}$  is the total number of disconnected melanoma regions in the lymph nodes.

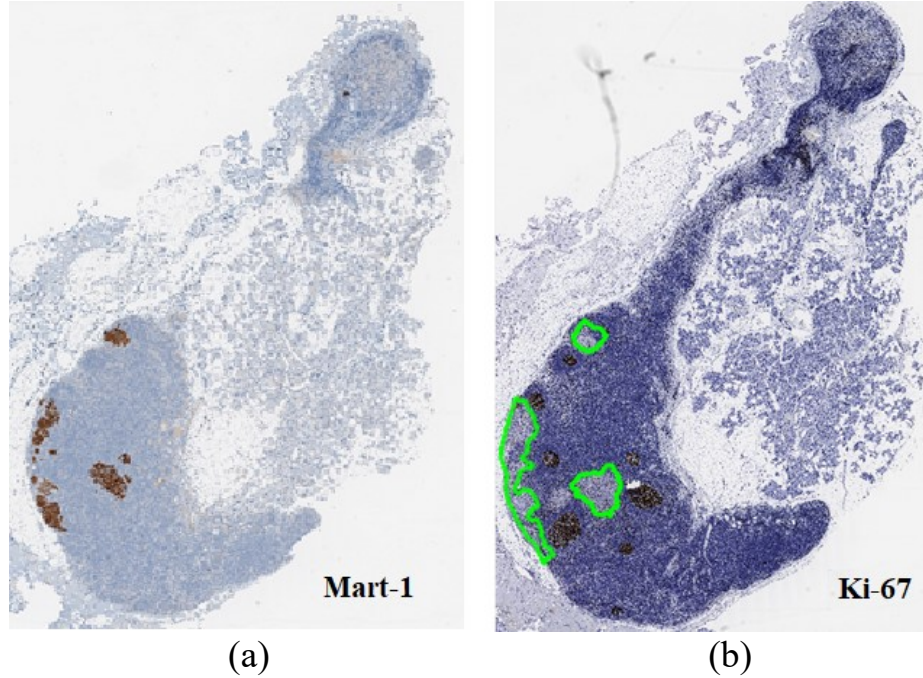


Figure 4.3. Histopathological image of two lymph nodes (a) MART-1-stained image, where melanoma appears in brown color and (b) Ki-67-stained image, where the green contour is the melanoma mask.

#### 4.3.2. CNN-based Segmentation

The objective of this module is to segment an input image window (from the detected melanoma region) into active nuclei, passive nuclei and background. In this Chapter, a new CNN architecture, as shown in Figure 4.4, is used to segment the Ki-67 images into three classes (background, passive and active nuclei). The CNN architecture consists of three paths: path A, path B and path C. The details of these three paths are listed in Table 4.1. The paths A and B have 8 and 9 convolutional layers, respectively (see Figure 4.4). Path C provides the residual connection (also known as skip connection) from the input layer to the Concatenate layer (denoted as Layer-CON in Table 4.1). The three paths start after the first convolution layer, become parallel, and meet again at the concatenate layer. This is followed by a convolutional layer, softmax and pixel classification layer. The details of these layers are explained in the following.

TABLE 4.1. Details of the Proposed architecture with 19 convolutional layers. Input image Size:  $H \times W$  pixels (color).

	Number of Channels (N)	Number of Filters	Output Image Size	Filter Size (S)
<b>Layer-I</b>	3	64	$H \times W \times 64$	<b><math>3 \times 3</math></b>
<b>Layer-A1</b>	Max-Pool, Stride [2,2]			
<b>Layer-A2</b>	64	64	$(H/2) \times (W/2) \times 64$	<b><math>3 \times 3</math></b>
<b>Layer-A3</b>	Max-Pool, Stride [2,2]			
<b>Layer-A4</b>	64	64	$(H/4) \times (W/4) \times 64$	<b><math>3 \times 3</math></b>
<b>Layer-A5</b>	Max-Pool, Stride [2,2]			
<b>Layer-A6</b>	64	64	$(H/8) \times (W/8) \times 64$	<b><math>3 \times 3</math></b>
<b>Layer-A7</b>	Max-Pool, Stride [2,2]			
<b>Layer-A8</b>	64	64	$(H/16) \times (W/16) \times 64$	<b><math>3 \times 3</math></b>
<b>Layer-A9</b>	UnPooling			
<b>Layer-A10</b>	64	64	$(H/8) \times (W/8) \times 64$	<b><math>3 \times 3</math></b>
<b>Layer-A11</b>	UnPooling			
<b>Layer-A12</b>	64	64	$(H/4) \times (W/4) \times 64$	<b><math>3 \times 3</math></b>
<b>Layer-A13</b>	UnPooling			
<b>Layer-A14</b>	64	64	$(H/2) \times (W/2) \times 64$	<b><math>3 \times 3</math></b>
<b>Layer-A15</b>	UnPooling			
<b>Layer-A16</b>	64	64	$H \times W \times 64$	<b><math>3 \times 3</math></b>
<b>Layer-B1</b>	64	3	$H \times W \times 64$	<b><math>5 \times 5</math></b>
<b>Layer-B2</b>	64	64	$H \times W \times 64$	<b><math>7 \times 7</math></b>
<b>Layer-B3</b>	64	64	$H \times W \times 64$	<b><math>9 \times 9</math></b>
<b>Layer-B4</b>	64	64	$H \times W \times 64$	<b><math>11 \times 11</math></b>
<b>Layer-B5</b>	64	64	$H \times W \times 64$	<b><math>13 \times 13</math></b>
<b>Layer-B6</b>	64	64	$H \times W \times 64$	<b><math>15 \times 15</math></b>
<b>Layer-B7</b>	64	64	$H \times W \times 64$	<b><math>17 \times 17</math></b>
<b>Layer-B8</b>	64	64	$H \times W \times 64$	<b><math>19 \times 19</math></b>
<b>Layer-B9</b>	64	64	$H \times W \times 64$	<b><math>21 \times 21</math></b>
<b>Layer-CON</b>	192		$H \times W \times 192$	
<b>Layer-O</b>	64	C	$H \times W \times C$	<b><math>3 \times 3</math></b>
<b>Softmax layer</b>	C		$H \times W \times C$	-
<b>Pixel Classification</b>	1		$H \times W$	-

1) *Convolutional layers*: The convolutional layer is similar to the neurons in a traditional neural network except that each neuron will be connected to a small neighborhood of neurons in the previous layer. Each neuron in the convolutional layer will result in a scalar value. In this Chapter, the convolutional layer performs three operations: convolution, batch normalization, and ReLU activation.



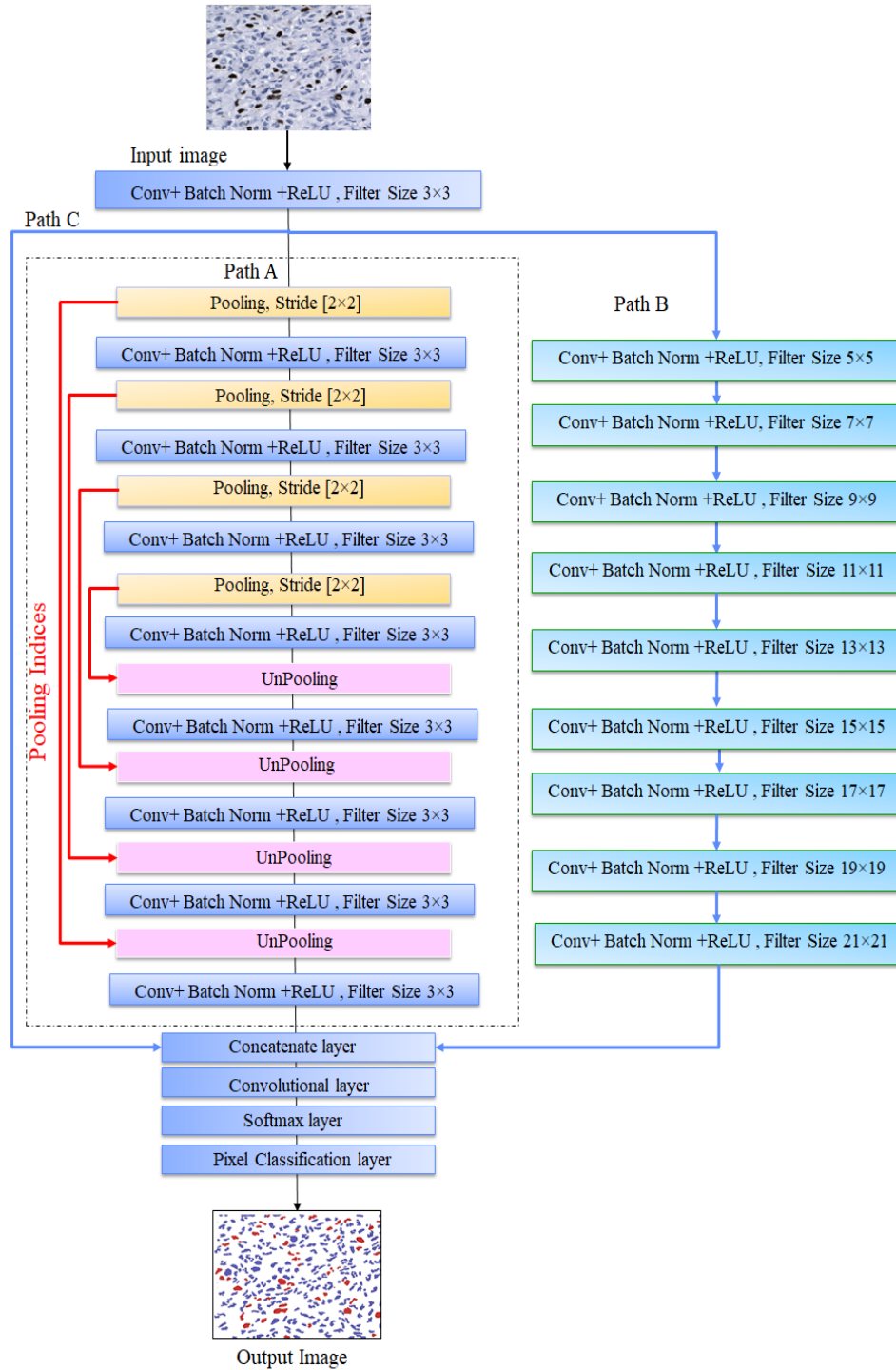


Figure 4.4. Proposed CNN architecture for nuclei segmentation (with 19 convolutional layers). Note that there are three paths after Layer I (first convolutional layer). Path A has 8 convolutional (shown in blue), 4 pooling (yellow) and 4 UnPooling (pink) layers. Path B has 9 convolutional layers. Path C is the residual connection from the output of layer I to the concatenate layer. Paths A, B and C meet at the Concatenate Layer.

(a) Let  $f_{l-1}$  denote the (3D) feature map generated in the convolutional layer  $l-1$ . In the convolution layer  $l$ , the feature map  $f_{l-1}$  is convolved with a (3D) filter  $F_j$ :

$$R_{l,j} = f_{l-1} * F_j, \quad j = 1, 2, \dots, N \quad (4.1)$$

where  $N$  is the number of filters in layer  $l$  (also known as the depth of the layer  $l$ ),  $R_{l,j}$  is the (2D) output corresponding to the  $j$ th convolution filter. Note that for the first convolution layer (i.e.,  $l=1$ ), the input image is considered as  $f_0$ . In the first convolutional layer (Layer I) of the network in Figure 4.4,  $f_0$ ,  $F_j$ , and  $R_{l,j}$  have dimensions of  $H \times W \times 3$ ,  $3 \times 3 \times 3$ , and  $H \times W \times 64$ , respectively (with the input image having  $H \times W$  pixels). In the proposed CNN, the number of filters is 64/layer (in both paths A and B) with size of  $S \times S$  (see Table 4.1). Note that  $S$  increases from 5 to 21 in subsequent layers in path B. However, it has a fixed value of 3 in all layers of path A. Note that the paths A and B provide complementary features: the path A focuses more on the coarse features whereas the path B focuses more on the fine features.

(b) Batch Normalization: During the CNN training, the convolution outputs  $R_{l,j}$  corresponding to all images in a mini batch (of  $B$  images) are considered. In this work, we have used  $B=8$ .

The  $R_{l,j}$  is made zero mean with unit variance as follows:

$$\hat{R}_{l,j} = \frac{R_{l,j} - \mu_j}{\sigma_j} \quad (4.2)$$

where  $\mu_j$  and  $\sigma_j$  are the mean and the standard deviation corresponding to the  $j$ th feature map for the layer  $l$  in a mini-batch. The normalized  $\hat{R}_{l,j}$  is scaled with  $\gamma$ , and a bias  $\beta$  is added as follows:

$$y_{l,j} = \gamma_{l,j} \hat{R}_{l,j} + \beta_{l,j} \quad (4.3)$$

Note that Eqs. 4. 2 and 4.3 are applied during both the training (with  $B=8$ ) and the testing (with  $B=1$ ). The  $\gamma$  and  $\beta$  are trainable parameters and are updated iteratively during the backpropagation.

(c) Activation: In this step, an activation function is applied on the batch normalized output  $y_j$ . In this work, the Rectified Linear Unit (ReLU) activation [86] is used as it has the advantages of speeding up the training [87] and inducing the sparsity in the hidden units [88]. In ReLU, all the negative pixel values are replaced by zeros, and the output is expressed as follows.

$$f_{l,j} = \max(0, y_{l,j}) \quad (4.4)$$

The overall output of convolutional layer  $l$ , as given below, will be passed on to the next layer.

$$f_l = \{f_{l,j}, j = 0, 1, \dots, N\}$$

Step (a)-(c) are repeated for each subsequent convolutional layer. After the ReLU module, the feature map  $f_l$  is used as the input of the next, i.e., the  $(l+1)th$ , convolutional layer.

2) *Pooling/ UnPooling Layers*: The pooling layers are used to extract the features in different image resolution, whereas the unpooling layers are used to return the extracted features with the same size as the original image ( $H \times W$ ) using bilinear interpolation. In the pooling layers, the max-pooling operations for  $[2 \times 2]$  pixels with stride  $[2 \times 2]$  are used. The indices of the maximum values in pooling layers are transferred to the corresponding unpooling layers.

3) *Concatenate Layer*: In this layer, the outputs of paths A, B and C, each with size  $H \times W \times 64$ , are concatenated to obtain an output feature map of size  $H \times W \times 192$ .

4) *Softmax*: The softmax layer is used after the last convolutional layer to generate the probability distribution of the classification results for each pixel. The output of the last convolutional layer consists of  $C$  feature maps (each of size  $H \times W$ ), where  $C$  is the number of the output classes. Let the feature map corresponding to the  $i$ th class ( $i=1,2,...C$ ) be denoted by  $\phi_i$ . The exponential summation of the feature maps,  $\Phi$ , is calculated as follows:

$$\Phi(h, w) = \sum_{i=1}^C \exp(\phi_i(h, w)) \quad 1 \leq h \leq H, 1 \leq w \leq W \quad (4.5)$$

The softmax layer calculates the class probability  $P_i$  for the pixel at location  $(h, w)$  using the following equation.

$$P_i(h, w) = \frac{\exp(\phi_i(h, w))}{\Phi(h, w)} \quad (4.6)$$

Note that the input pixels are classified into three classes (i.e.,  $C=3$ ): background, active nuclei and passive nuclei.

5) *Pixel classification*: This layer performs the classification of the image pixels using the corresponding class probability. The class with the highest probability is chosen as the pixel output classes.

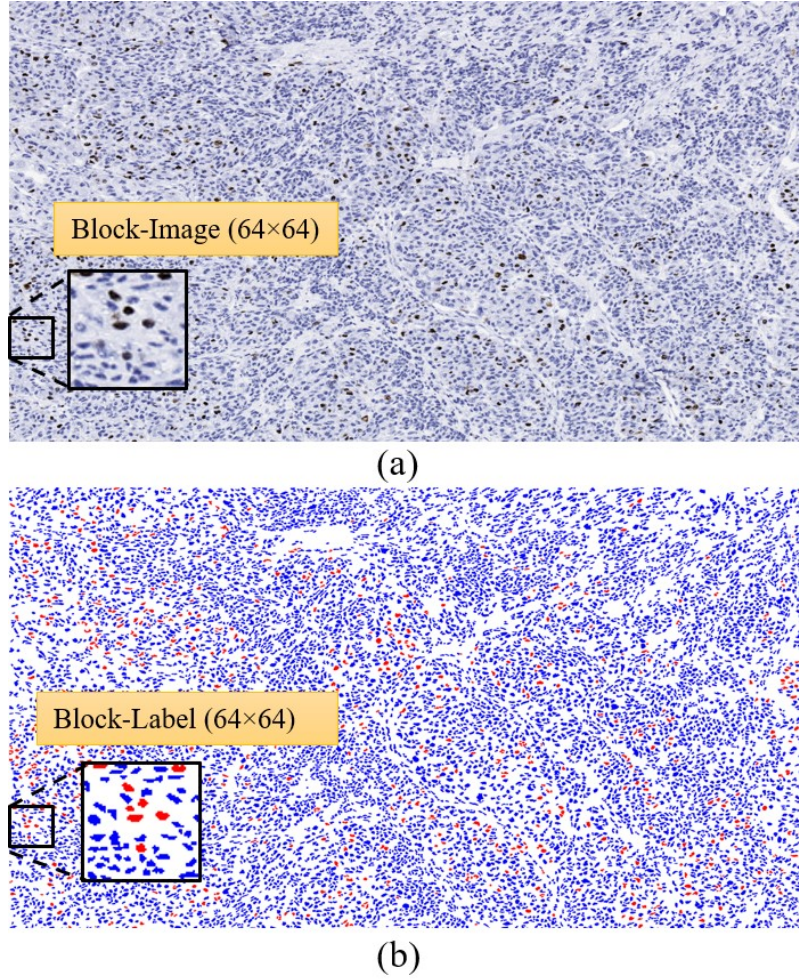


Figure 4.5. Example of (a) an original RGB Image ( $704 \times 1280$ ) and (b) the corresponding classified ground truth image, where the active and passive nuclei appear in red and blue color, respectively.

#### 4.3.3. CNN Training

There are about 7,513,247 parameters in the proposed CNN, which need to be trained. In the training phase of the CNN, 56 ROI windows (as described in section 4.2) are used. Note that each window contains thousands of nuclei (see Figure 4.5). These 56 windows are divided into training (49 windows) and validation (7 windows) datasets. As it is computationally expensive to use the whole window as input to the CNN, each window is further divided into non-overlapping blocks of  $64 \times 64$  color pixels to obtain 220 block-images (an example of a block-image is shown in Figure 5). The total number of the obtained block-images is 12,320 ( $=56 \times 220$ ).

The 12,320 images are also augmented by horizontal and vertical flipping to obtain 36,960 images (32,340 training and 4,620 for validation). The image augmentation is used to generalize the parameters of the CNN model and have better performance [89].

For CNN training, a loss function and an optimization algorithm need to be defined. In this Chapter, we use the cross-entropy loss function for multi-class classification. The loss function  $X$  for a pixel at  $(m,n)$  location is calculated as follows:

$$X(m,n) = \sum_{i=1}^C T_i(m,n) \ln P_i(m,n) \quad (4.7)$$

where  $T_i(m,n)$  is the  $i$ th-ground truth class probability and  $P_i(m,n)$  is the  $i$ th-class probability (predicted by the Softmax layer). The total loss for a mini-batch of  $B$  block-images (each with size  $H \times W$ ) is then calculated as follows:

$$E = \sum_{b=1}^B \sum_{m=1}^H \sum_{n=1}^W X_b(m,n) \quad (4.8)$$

where  $X_b$  is the loss function for the  $b$ th-block image. As the three classes of pixels have different distributions for each class, the loss function is weighted for each class differently. The weights  $\varphi_i$  for different classes are calculated as follows:

$$\varphi_i = \frac{\text{median freq}}{\text{freq}(i)} \quad 1 \leq i \leq C \quad (4.9)$$

where the class frequency  $\text{freq}(i)$  is a ratio of the number of the pixels that represent the  $i$ -class to the total number of pixels in the training dataset, and  $\text{median freq}$  is the median of the class frequencies  $\{\text{freq}(i)\}$ . To minimize the loss function  $E$ , the stochastic gradient descent with momentum (SGDM) optimizer [90] is used in the proposed technique. The SGDM accelerates stochastic gradient descent (SGD) and reduces the oscillation problem of SGD by adding the contribution from the previous iteration to the current iteration. The network parameters at the end of the  $n$ th iteration are updated as follows:

$$\theta_{n+1} = \theta_n - \alpha \nabla E(\theta_n) + \mu (\theta_n - \theta_{n-1}) \quad (4.10)$$

where  $\theta$  is the parameter vector, which includes parameters such as normalization weights, filters and biases,  $\nabla E(\theta_n)$  is the gradient of the loss function,  $\alpha$  is the learning rate, and  $\mu$  is the momentum. The learning rate  $\alpha$  is initialized to 0.01 and is reduced by a factor of 0.2 every 10

epochs. In this work, we have used  $\mu = 0.9$ , and the maximum number of epochs is set to 100. Note that the training accuracy and the loss are calculated for each individual mini-batch.

Figure 4.6 shows an example of the evolution of the training and the validation accuracy over different iterations. The validation accuracy and the loss are calculated on the validation dataset at the end of every 250 iterations. The network training is stopped when the validation loss has not decreased in the previous 5 validations. Note that each epoch performs 4,042 ( $=32,340/8$ ) iterations and the training of the CNN stopped at iteration 28,644 (at around 7th epoch) in this example.

The CNN model is trained using 56 Ki-67 ROI windows (49 for training and 7 for validation) as described in Section 4.2. As five-fold cross validation is used in this Chapter, five CNN models are trained, one for each fold.

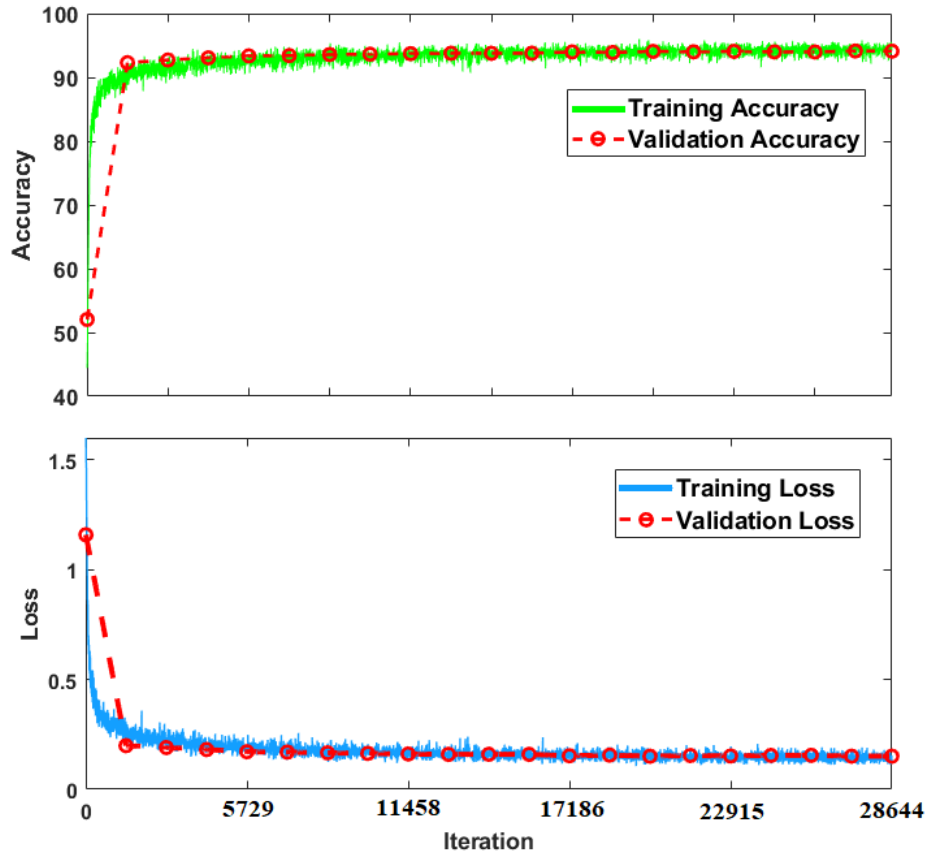


Figure 4.6. Loss and accuracy plots during the network training process.

#### 4.3.4. CNN Configuration

The CNN architecture proposed for the nuclei segmentation was shown in Figure 4.4. In this section, we evaluate the performance of the different paths and finetune the hyper parameters to

obtain the best performance. The segmentation performance is measured using: Accuracy, Intersection over Union (IoU), and *BF* score. The performance measures are calculated for each of the three pixel-classes separately. For example, when the IoU for active nuclei class is calculated, the active nuclei pixels are considered positive and both passive and background pixels are considered as negative. The performance measures for three classes are then averaged to obtain the mean accuracy, mean IoU and mean *BF* score, which are used for the overall performance comparison. To analyze the performance of each path, an ablation study is performed, and the performance of the different combinations of paths is shown in Table 4.2. It is observed that the proposed architecture, with all three paths A, B and C, provides performance superior to the other combinations: A, A+B or A+C. The Path A can efficiently detect the nuclei in different scales by applying several pooling and un-pooling layers. The Path A is therefore helpful to detect the coarse features (due to pooling) of the objects. Path B has been used with different sizes of filters and without using any pooling layers to obtain fine segmentation of the nuclei. The residual connection in path C reduces the impact of vanishing gradients problem caused by the large number of layers in paths A and B [82,91]. By combining all three paths, there will be minimal information loss and better feature extraction to segment the three classes of pixels

TABLE 4.2. Segmentation Performance of the proposed technique.

Technique:	<i>Mean Accuracy</i>	<i>Mean IoU</i>	<i>Mean BF Score</i>
<b>Path A</b>	0.86	0.80	0.70
<b>Path A+C</b>	0.90	0.83	0.71
<b>Path A+B</b>	0.91	0.85	0.74
<b>Path A+B+C</b>	0.94	0.89	0.82

Figure 4.7. shows visual examples of nuclei segmentation results, with and without Path B. It is observed that the CNN with path A+C provides the coarse segmentation boundaries. When the Path B is included in the CNN, more accurate segmentation results are obtained for both Passive (contoured in cyan) and Active (contoured in red) nuclei.

Figure 4.8. shows the nuclei segmentation performance with different numbers of convolutional layers in path B (paths A and C are considered fixed during the performance evaluation). It is observed that nine layers in path B provides the best performance. In a similar way, Path A was also evaluated (results not shown in the Chapter) to determine the optimal number of layers



(keeping paths B and C fixed). Eight convolutional layers and four pooling and four un-pooling layers in Path A were found to provide the best nuclei segmentation performance.

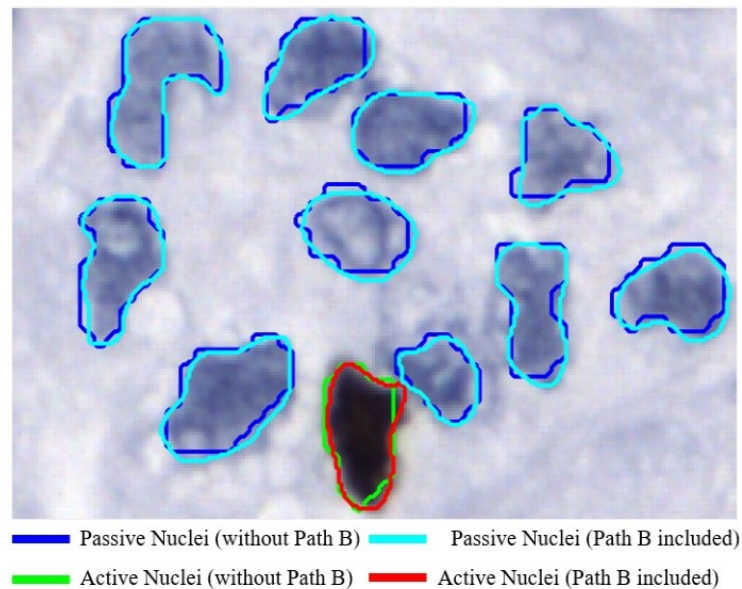


Figure 4.7. Comparison of the nuclei segmentation performance using paths A+C (i.e., without path B) and paths A+B+C.

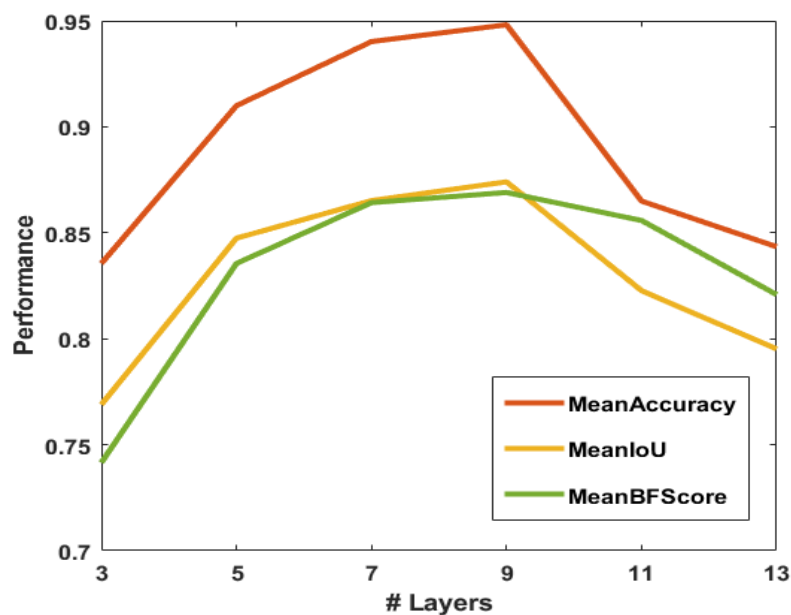


Figure 4.8. Segmentation performance evaluation with different number of layers in path B.



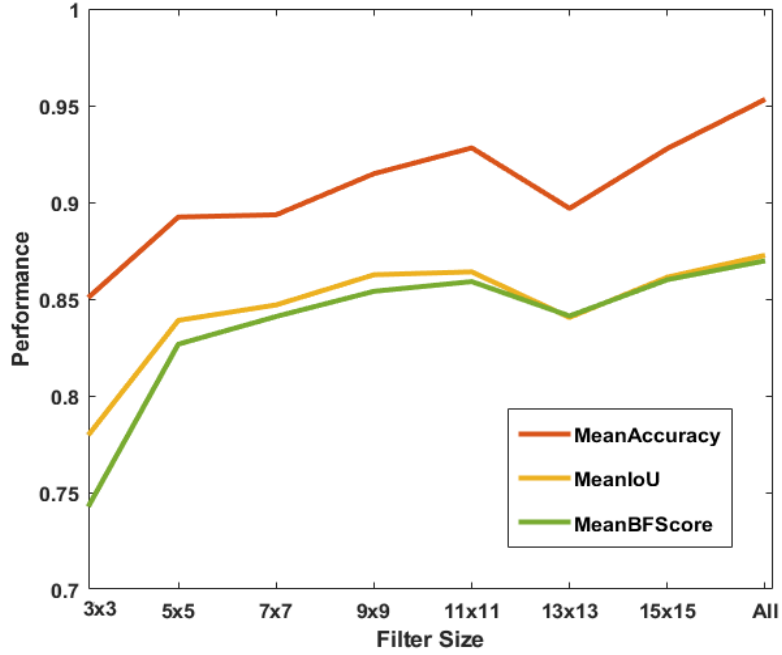


Figure 4.9. Performance evaluation with different size of filters in Path B.

Figure 4.9 shows the performance of the proposed CNN with different sizes of filters in path B. In this evaluation, eight CNN architectures are trained with 9 layers. In the first seven architectures, the filter size for all layers is kept fixed, i.e.,  $S \times S$ , where  $S=3, 5, 7, 9, 11, 13$  and  $15$  for the seven architectures. For the eighth architecture, the filter size for each layer increases from 5 to 21 in steps of 2. As observed in Figure 4.9, the eighth architecture (which includes variable filter size) provides the best segmentation performance.

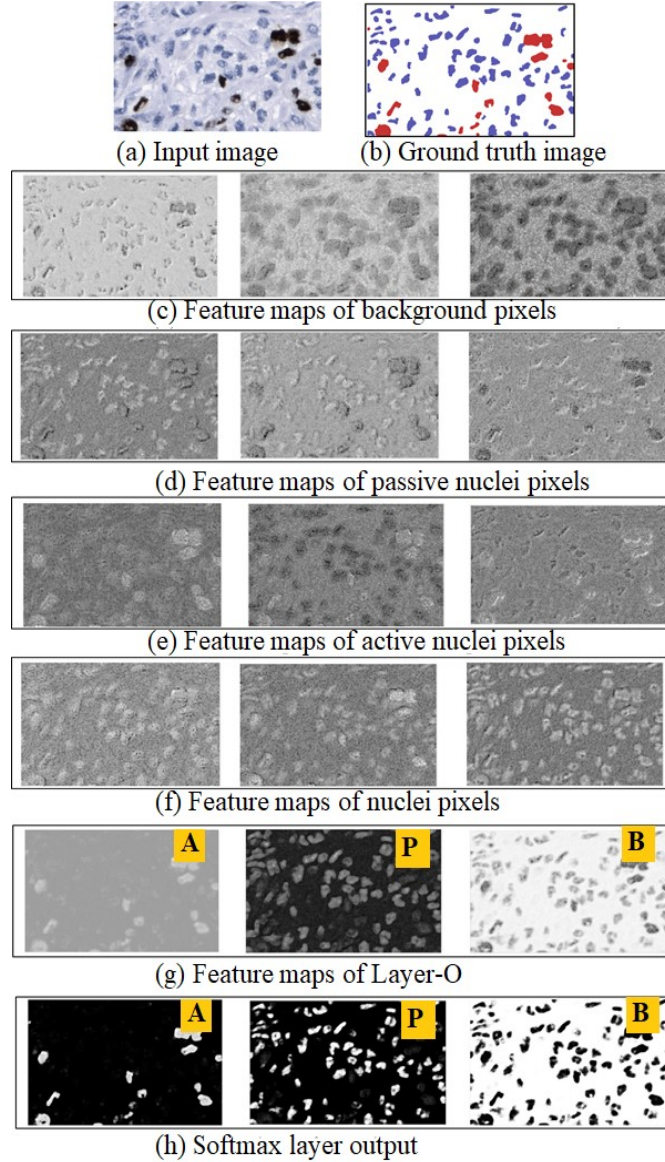


Figure 4.10. Example of the feature maps obtained from path B in the proposed CNN. (a) Ki-67 image. (b) ground truth segmented image, (c)-(f) 12 of the 64 feature maps obtained after Layer-B3. (g) Output of Layer-O. (h) Softmax layer output. A: Active nuclei, P: Passive nuclei, and B: Background feature map.

Figure 4.10. shows an example of the obtained features maps on Path B of the proposed CNN. Figure 4.10 (a) shows an input image and Figure 4.10 (b) shows the corresponding segmented ground truth image where the active, passive, and background pixels are shown in red, blue and white. As shown in Table 4.1, there are 64 feature maps at the output of convolution Layer-B3. Twelve of the 64 feature maps are shown in Figs. 4.10 (c)-(f). Figure 4.10 (g) shows the three ( $C=3$ ) channel output of Layer-O, which primarily represents the active, passive, and background

feature maps. Figure 4.10 (h) shows the output of the softmax layer: the three images showing the class probabilities (in the range  $[0,1]$ ) of each pixel. Note that for a pixel, the sum of all three probabilities (from three images) is one. As observed in Figure 4.10, there are feature maps that can represent one class as shown in (c), (d), and (e), or two as shown in (d). Note that the feature maps in (c), (d), (e), and (f) primarily detect the background, passive nuclei, active nuclei, and passive+active nuclei pixels, respectively.

#### 4.3.5. PI Calculation

After the melanoma tumor regions in a Ki-67 image is segmented into three classes, the next task is to determine the melanoma subregions (ROI) with the highest PI values. The *PI* value of an ROI is typically calculated using the following equation:

$$PI = \frac{NA}{NA + NP} \times 100 \quad (4.11)$$

where *NA* and *NP* are the number of the active and the passive nuclei in the ROI. In this Chapter, before PI values are calculated, the active and the passive nuclei are detected using the following steps.

- (i) The active and the passive nuclei pixels are determined using the CNN.
- (ii) Connected component analysis is done to form active and passive nuclei from the classified pixels. Most of the nuclei will be isolated nuclei, but some will be overlapped nuclei, also known as nuclei clump.
- (iii) Ellipse descriptor analysis is applied to separate the isolated nuclei from the nuclei clumps in the ROI (based on ellipticity parameter and size of the nuclei) [29].
- (iv) The nuclei clumps are segmented into multiple overlapped active or passive nuclei using generalized Laplacian of Gaussian (gLoG) seed detection algorithm [30].

In this Chapter, a few ROI windows ( $K \times L$  pixels) in melanoma regions with highest PI values are determined using the following steps.

- (i) In the tumor region, a moving window ( $K \times L$  pixels) is used.
- (ii) For each window, the numbers of active (*NA*) and passive (*NP*) nuclei inside the window are calculated.
- (iii) Based on the *NA* and *NP*, the PI value of a window is calculated using Eq. (4.11).
- (iv) A few windows with highest PI values are chosen for grading the tumor and further analysis.

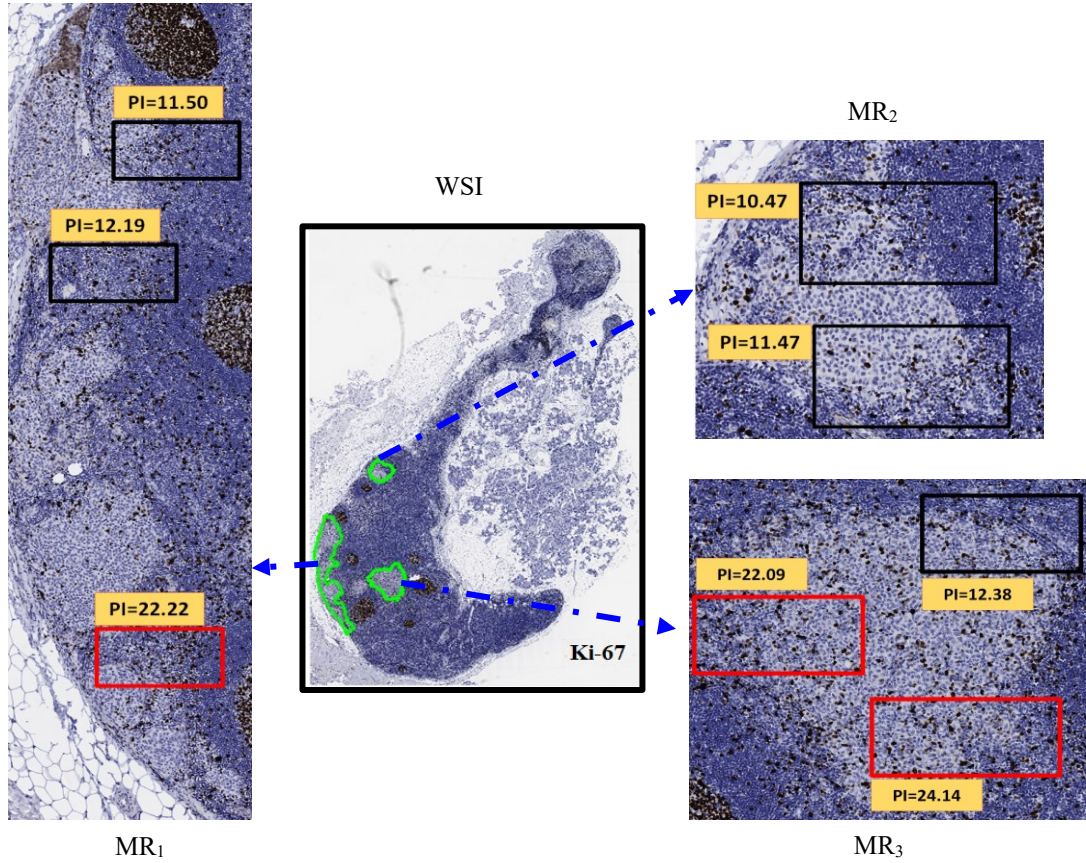


Figure 4.11. Example of PI calculation of ROIs in the three melanoma regions ( $MR_1$ ,  $MR_2$ ,  $MR_3$ ) in a WSI. The three melanoma regions in the WSI are shown with magnification. The regions  $MR_1$  and  $MR_2$  contain three blocks (with red contours) with the highest PI values: 24.14, 22.22, and 22.09. The other five blocks (with black contours) are also active areas, but the PI values are smaller.

Figure 4.11. shows the calculation of few PI values in three melanoma regions in the WSI. The window size used is  $250 \times 500$  ( $K \times L$ ) pixels. Two-three windows with highest PI values are shown in each of three regions. Finally, the three windows with overall highest PI values are shown with red contour. A magnified version of the window with the highest PI values ( $PI=24.14$ ) is shown in Figure 4.12. The active and the passive nuclei are shown as red and green + symbols. For this window, the ground truth PI value is 25.15 while the obtained PI value is 24.14.



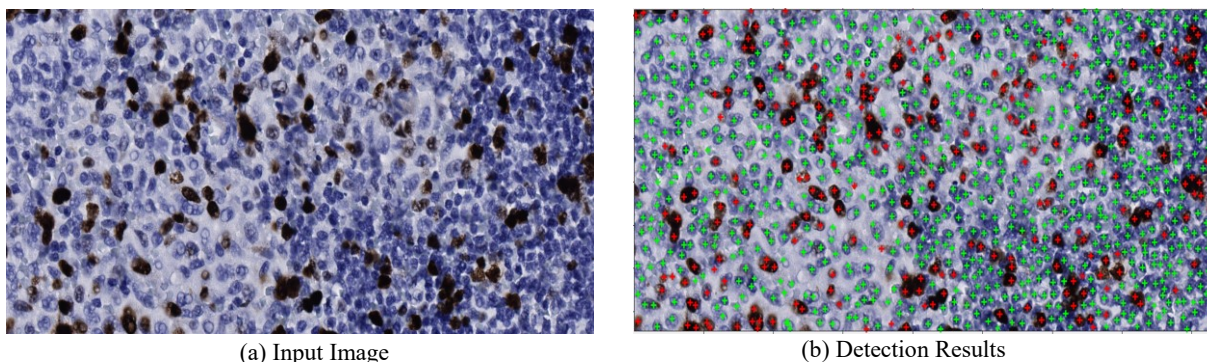


Figure 4.12. Magnified window with the highest PI value ( $PI=24.14$ ) in Figure 4.11. (a) input image (b) Detection results with 252 active and 792 passive nuclei. The ground truth  $PI=25.15$  with 252 active and 750 passive nuclei.

## 4.4. Performance Evaluation

In this section, the performance of the proposed technique is presented and compared with a few state-of the art techniques for PI calculation, namely FCM+KM [63], GMM+CNN [84], Otsu+SVM [80], PI-SegNet [85]. As UNet and DeepLab have become very popular CNN architecture, these CNN architectures have also been implemented in this work and the performance has been compared with the proposed technique. Henceforth, these techniques are referred to as PI-UNet and PI-DeepLab. In these techniques, the nuclei segmentation is done using UNet and DeepLab, and the PI calculation is done using the algorithm in Section 4.3.5. In the following, the nuclei segmentation performance is first evaluated and compared. The PI calculation performance is presented next.

Optimal parameters were used for performance evaluation of all techniques. In FCM+KM technique, two clusters (nuclei and background) were used for the FCM and two classes (active and passive) were used for the KM algorithm. In Otsu+SVM, one optimal threshold was used for nuclei and background segmentation, and the Gaussian kernel was used for the SVM. The layer configurations of the CNN architectures in the PI-SegNet, PI-UNet, PI-DeepLab, and the proposed technique are shown in Table 4.2. It is observed that the number of layers varies between 37-100 in the various CNNs. Note that the GMM+CNN is not included in the segmentation performance comparison as the technique does not perform nuclei segmentation.

Figure 4.13 (c)-(h) show visual examples (for subjective assessments) of the segmentation results of FCM+KM, Otsu+SVM, PI-SegNet, PI-UNet, PI-DeepLab and the proposed technique, respectively. In Fig 13 (c)-(g), the passive and the active nuclei are shown with blue and green

contours, respectively. A few coarse nuclei boundaries can be observed in Figure 4.13(c) and (d). In addition, a part of an active nuclei may be segmented as passive nuclei. This is because these techniques (FCM, Otsu) are based on thresholding and do not consider the shape features of the nuclei during the segmentation process. On the other hand, the PI-SegNet, PI-UNet, and PI-DeepLab techniques segment the nuclei with respect to their morphological features (see Figure 4.13 (e)-(g)), and results in higher accuracy. Note that the PI-SegNet, PI-UNet, and PI-DeepLab architectures include several pooling layers. As the pooling operation typically causes loss of morphological features (e.g., shape feature) of nuclei, it is likely to degrade the quality of the nuclei segmentation results. In addition, the PI-SegNet and PI-UNet architectures have a large number of convolutional layers at the encoder/decoder side, which may cause vanishing gradients.

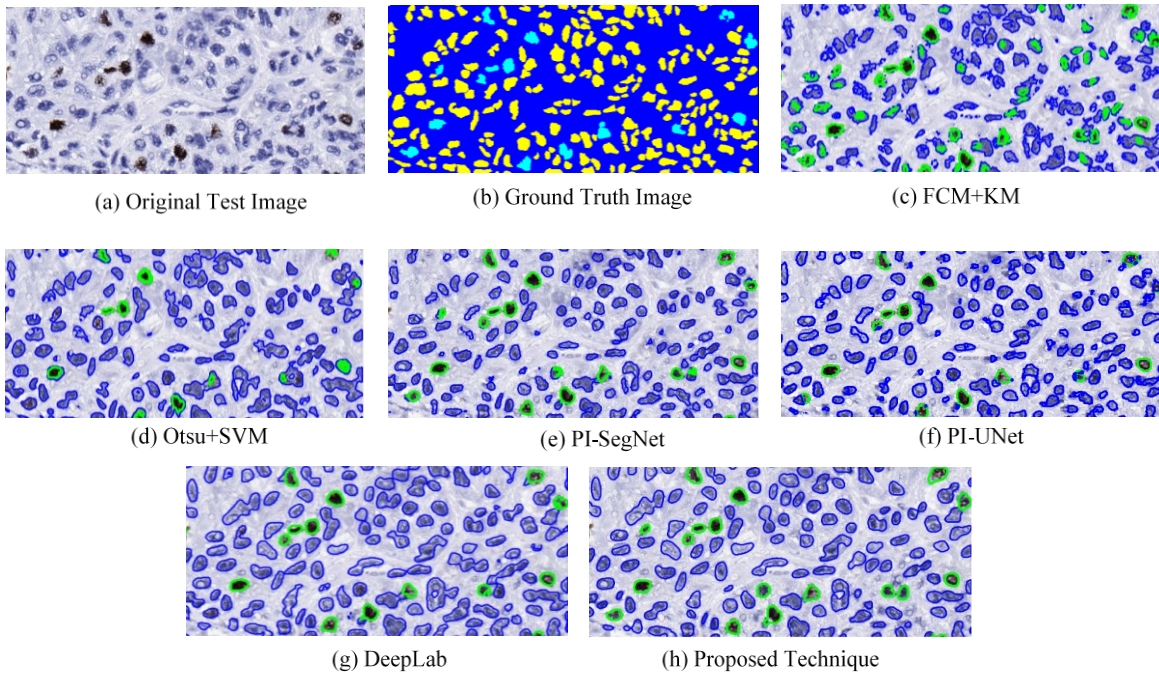


Figure 4.13. Subjective comparison of segmentation results. (a) Original test image, (b) The ground truth segmentation mask, (c)-(h) Segmentation results for FCM+KM, Otsu+SVM, PI-SegNet, PI-UNet, PI-DeepLab and the proposed technique, respectively.

Figure 4.13 (g) shows the output obtained by the proposed technique, and it is observed that the proposed architecture provides an excellent nuclei segmentation performance. Table 4.3 compares the segmentation performance of FCM+KM, Otsu+SVM, PI-UNet, PI-SegNet and PI-DeepLab techniques with the proposed technique using the testing dataset (see section 4.2). As observed in

Table 4.3, the proposed technique provides the best performance with an average 94% accuracy, 89% IoU and 82% *BF* score for five-fold cross validations. Note that the training and the testing dataset are kept completely independent to ensure an unbiased performance comparison.

TABLE 4.3. LAYER CONFIGURATION OF THE DEEP LEARNING TECHNIQUES.

Technique	No. of layers in CNN	Details of CNN architecture
PI-SegNet [85]	37	1-In,9-Conv, 8-Btch, 8-Rlu, 4-Mx, 4-Up, 1-Dth, 1-Sft,1-Px
PI-UNet	58	1-In, 19-Conv, 22-Rlu, 4-Mx, 4-Up, 2-Dr, 4-Dth,1-Sft,1-Px
PI-DeepLab	100	1-In,29-Conv, 28-Btch, 25-Rlu, 2-Cr, 1-Mx, 2-Up, 8-Ad, 2-Dth, 1-Sft,1-Px
Proposed Technique	67	1-In, 19-Conv, 18-Rlu, 18-Btch, 4-Mx, 4-Up, 1-Dth,1-Sft,1-Px
Notations		
In: Input image normalization Layer Mx: Max pooling layer Up: Up-sampling layer Dr: Dropout layer Px: Pixel classification layer Ad: Addition layer		Conv: Convolutional Layer Btch: Batch normalization Layer Rlu: ReLU Layer Dth: Depth concatenate layer Sft: Softmax layer Cr: Crop layer

Table 4.4. SEGMENTATION PERFORMANCE OF THE PROPOSED TECHNIQUE.

Technique:	Accuracy	IoU	BF Score
FCM+KM [63]	0.74	0.73	0.72
Otsu+SVM [80]	0.78	0.76	0.78
PI-SegNet [85]	0.86	0.80	0.70
PI-UNet	0.84	0.75	0.71
PI-DeepLab <sup>1</sup>	0.88	0.82	0.71
Proposed Technique	0.94	0.89	0.82

<sup>1</sup>Segmentation performance obtained using DeepLabV3[83]

The PI calculation performance of the proposed technique is now evaluated. The Mean Absolute Error (*MAE*), and the Mean Percentage Error (*MPE*) are used as the performance measures, which are defined as follows:

$$MAE = \frac{1}{K} \sum_{k=1}^K |G(k) - B(k)| \quad (4.12)$$

$$MPE = \frac{1}{K} \sum_{k=1}^K \left| \frac{G(k) - B(k)}{G(k)} \right| \times 100\% \quad (4.13)$$

where  $G(k)$  and  $B(k)$  are the ground truth and the obtained PI values for the  $k$ th test image, and  $K$  is the number of images.

The PI calculation performance of the proposed technique is compared with the state-of-the-art techniques in Table 4.5. For each testing set, the  $MAE$  and  $MPE$  values are calculated using Eqs. 12 and 13 for 14 ROI windows. For five-fold cross-validation, 5 sets of  $MAE$  and  $MPE$  values are obtained, and the average  $MAE$  and  $MPE$  values are shown in Table 4.5. It is observed that the FCM+KM technique calculates PI values with highest error (i.e.,  $MAE$  and  $MPE$  values). This is perhaps because, in the FCM+KM technique, the active and the passive nuclei pixels are separated using the K-Means algorithm, which may have low accuracy due to the intensity variation of the pixels. The GMM+CNN technique provides performance better than FCM+KM, although the  $MAE$  and  $MPE$  values are still high. This is perhaps because this technique does not perform nuclei segmentation. Instead, it generates patches around the detected nuclei seeds and classifies the patches as active or passive. The CNN classifier cannot reliably classify a patch that contains both the active and the passive nuclei, resulting in a lower performance.

TABLE 4.5. COMPARISON OF PI CALCULATION PERFORMANCE.

Technique	MAE	MPE	Execution time (in s)
FCM+KM [63]	3.76	31.34	90
Otsu+SVM [80]	0.89	7.37	16
GMM+CNN [84]	2.45	18.89	130
PI-SegNet [85]	0.68	5.35	14
PI-UNet	0.71	5.55	16
PI-DeepLab	0.61	4.59	20
Proposed Technique	0.52	3.92	18

The PI-SegNet and PI-UNet provide a better and somewhat comparable performance. The PI-DeepLab provides improved results compared to SegNet and UNet. The proposed technique provides the best performance (i.e., lowest error rate).

The computational complexity of various CNN-based techniques, in terms of execution time, is now presented. All techniques were implemented using MATLAB R2020a, and CNNs were implemented using the Deep Network Designer Toolbox. All experiments are performed on a Windows 10 computer with Intel i7-4790 CPU, 12 GB RAM, and NVIDIA GeForce GTX 745 graphic card. The average execution time (for both segmentation and PI calculation) for a WSI in testing mode is shown in the last column of Table 4.6. It is observed that the GMM+CNN requires



the highest execution time. Note that in this technique the GMM (for nuclei detection) takes about 90% of the overall execution time. FCM+KM technique also requires long execution time due to the FCM and KM algorithms. The other techniques use trained models, are fast in testing mode, and the execution times are comparable. It is observed that the proposed technique has an average of execution time of about 18 seconds per image.

Table 4.5 compares the training time required by the CNN architectures (GMM+CNN, PI-SegNet, PI-UNet, PI-DeepLab and the proposed architecture). All four CNN architectures are trained using an NVIDIA GeForce GTX 745 graphic card. Column 2 and 3 show the training time and the required number of training epochs. The proposed architecture typically finishes the training at around the 7<sup>th</sup> epoch, and the overall training time is comparable with other architectures.

TABLE 4.6. TRAINING TIME OF CNN MODELS.

Technique	Training time (in M)	Training epochs	No. of Training Parameters
GMM+CNN [84]	129	7	189,341
PI-SegNet [85]	141	14	225,987
PI-UNet	180	16	29,379,955
PI-DeepLab	175	6	20,661,638
Proposed Technique	155	7	7,513,247

## 4.5. Conclusions

This Chapter proposes an automated technique for proliferative index calculation in lymph node histopathological images. The PI value has been calculated for melanoma regions in the lymph nodes image. The technique uses CNN technique to segment and classify the Ki-67-stained image into three classes (i.e., background, active and passive nuclei). The proposed CNN architecture is used for the segmentation and classification purposes. Experimental results show that the proposed technique provides an excellent performance in terms of segmentation results (with 94% accuracy) and average PI error (mean error of 0.52).

# Chapter 5

## Melanoma Cell Detection in Lymph Node Histopathological Images Using Deep Learning

Histopathological images are widely used to diagnose diseases including skin cancer. As digital histopathological images are typically of very large size, in the order of several billion pixels, automated identification of all abnormal cell nuclei and their distribution within multiple tissue sections would assist rapid comprehensive diagnostic assessment. In this Chapter, we propose a technique, using deep learning algorithms, to segment the cell nuclei in Hematoxylin and Eosin (H&E) stained images and detect the abnormal melanocytes within histopathological images. The Nuclear segmentation is done by using a Convolutional Neural Network (CNN) and hand-crafted features are extracted for each nucleus. The segmented nuclei are then classified into normal and abnormal nuclei using a Support Vector Machine classifier. Experimental results show that the CNN can segment the nuclei with more than 90% accuracy. The proposed technique has a low computational complexity.

### 5.1. Introduction

Primary cutaneous melanomas include a range of potentially lethal melanocytic neoplasms which most often present in skin as an archetypical macular growth phase lesion consisting of an in-situ component plus a papillary dermal component of similar cytomorphology. The diagnosis depends upon the histomorphological identification of abnormal melanocytes forming radial and vertical growth phase neoplastic cellular infiltrates which by invasion and widespread metastasis can secondarily involve regional lymph nodes and ultimately any other part of the body. As per recent statistics, it is estimated that about 100,350 new cases of melanoma cancer will be diagnosed in the United States alone in 2020, which will result in about 6,850 deaths [91]. The early diagnosis of melanoma is very important as it helps to increase the chances of successful treatment and the survival rate. The Computer-aided diagnosis (CAD) techniques can effectively help doctors to diagnose and detect the melanoma in early stages [92]. The digitized histopathological slides, which are typically obtained by staining and scanning the biopsy slides of the skin tissue, can provide the cell morphological features with a high resolution. The digitized slides are known as

Whole Slide Images (WSIs) and with help of CAD techniques that will permit the pathologist for precise diagnosis [26]. Pathologists usually use H&E-stained images, because the morphological features of the melanocytes and other cells become vividly clear. In H&E-stained image, the cell nuclei contain chromatin and that can be observed in blue shade while the cytoplasm and other connective tissues are observed with varying shades of pink.

Figure 5.1 shows an H&E-stained histopathological image of malignant melanoma within regional lymph nodes (amidst adjacent salivary gland). The Lymph node cross-sections in the image are contoured with black color, and malignant are contoured in green color. Note that in this image the malignant melanoma are contoured manually by morphology. In the zoomed patch, it is observed that the abnormal melanocytes appear with irregularity in shape and color intensity [9,10].

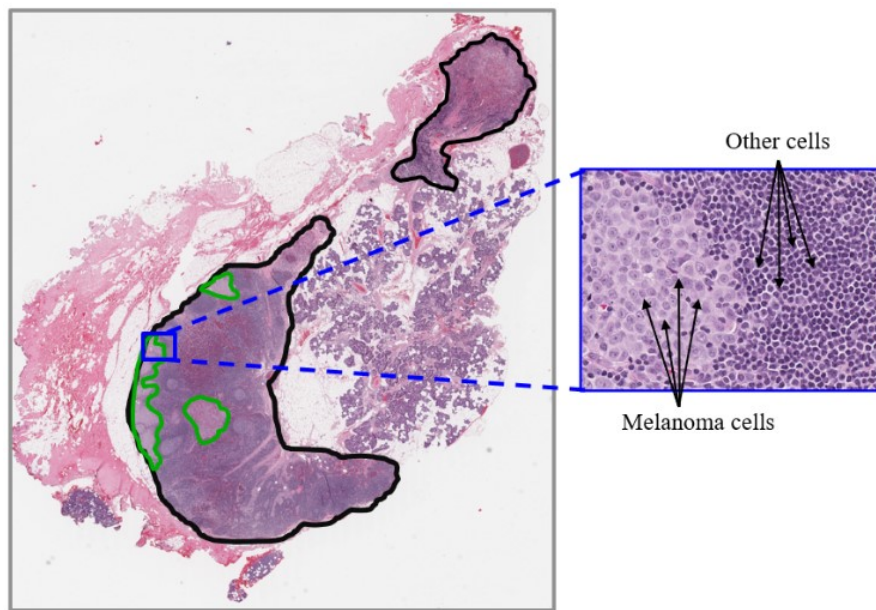


Figure 5.1. Example of an H&E-stained lymph node tissue image. The lymph node tissue is contoured in black, and malignant melanoma deposits are contoured in green.

Several techniques have been proposed to segment the cell nuclei in histopathological images [5,44,93-96]. Xu et al. [44] proposed an automated technique (henceforth referred to as the Watershed+Voting technique) to segment the cell nuclei in H&E-stained images. The technique detects the nuclei seeds by using voting areas and segments the nuclei cells using a watershed algorithm. The technique provides a good performance with high computational complexity due

the seed detection algorithm. Xu et al. [96] also proposed cell nuclei segmentation technique (henceforth referred to as the gLoG+mRLS technique) using generalized Laplacian of Gaussian (gLoG) filters to detect the seeds nuclei and multiple Radial Lines Scanning (mRLS) algorithm to segment the cells. The mRLS uses high gradient pixel locations and shape information to accurately segment the cell nuclei.

The techniques [5,44,93-96] mentioned above are generally based on extracted hand-crafted features that require significant time to calculate. The deep learning algorithms using CNN have recently been used successfully in medical image analysis. The CNN models can train the feature extraction process to provide high performance with low computational complexity in many different tasks (e.g. classification, detection or segmentation [66,97]). Basrinarayanan et al. [67] proposed the SegNet architecture for object segmentation. The architecture uses a number of sampling and upsampling layers for extracting the features in hierarchical levels. Ronneberger et al. [81] proposed the U-Net architecture for biomedical image segmentation. The U-Net architecture has encoder and decoder sides with a number of sampling and upsampling layers, respectively. The upsampling layer outputs are enhanced by concatenating them with features from the encoder side.

In this Chapter, we propose an automated technique to segment the cell nuclei and differentiate melanoma from non-melanoma cells using a Support Vector Machine (SVM) classifier. The technique uses a CNN architecture to segment the cell nuclei in H&E-stained images. The proposed CNN used several convolutional layers with different sizes of filters. Experimental results demonstrate high accuracy and low computational complexity of the proposed technique compared to the state-of-the-art techniques.

The organization of the Chapter is as follows. Section 5.2 describes the dataset used to train and evaluate the proposed technique. Section 5.3 describes the proposed technique in detail. Section 5.4 presents the performance evaluation, followed by the conclusion in Section 5.5.

## **5.2. Data Description**

In this section, we present the details of the training and testing dataset to evaluate the performance of the proposed nuclei segmentation and cell classification technique. The digitized biopsies were collected at the Cross Cancer Institute, University of Alberta, Edmonton, Canada in accordance with the protocol for the examination of specimens with skin melanoma. Standard Neutral

Buffered formalin-fixed paraffin-embedded tissue blocks of these biopsies were cut into thin slices (e.g., 4 $\mu$ m for light microscope). These slices were then mounted to glass slides and stained using H&E stain [93]. The WSIs were obtained by scanning the H&E slides using aperio scanscope scanning system under 40X magnification. The size of a WSI is typically around 40,000 $\times$ 60,000 pixels (in color) and each WSI contains thousands of cell nuclei. The image dataset consists of 9 WSIs of lymph node tissue.

### 5.3. Proposed Technique

The schematic of the proposed technique is shown in Figure 5.2 which consists of two modules: CNN-based nuclei segmentation and nuclei classification. The details of each module are presented in the following.

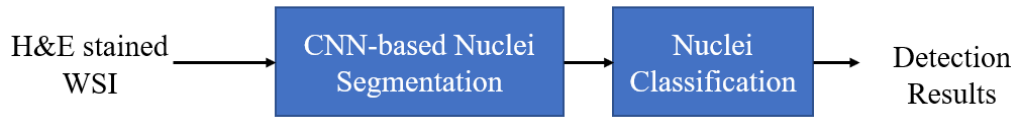


Figure 5.2. Schematic of the proposed melanoma detection technique.

#### 5.3.1. CNN-based Nuclei Segmentation

In this module, the input H&E-stained images are segmented into cell nuclei and background. The nuclei segmentation is done by using the proposed CNN architecture, henceforth referred to as the NS-Net architecture (Nuclei Segmentation Net). The NS-Net architecture, shown in Figure 5.3, consists of five convolutional layers (shown in gray color) and one softmax (shown in pink) followed by the pixel classification layer (shown in blue). The convolutional layer in the NS-architecture consists of three operations: convolution, batch normalization [98], and activation [86]. A brief description of each operation is presented in the following:

- (i) Convolution: Let  $f_{l-1}$  denote the (3D) feature map generated in the convolutional layer  $l-1$ . In the convolution layer  $l$ , the feature map  $f_{l-1}$  is convolved with a (3D) filter  $F_j$ :

$$R_{l,j} = f_{l-1} * F_j, \quad j = 1, 2, \dots, N \quad (5.1)$$

where  $N$  is the number of filters (which is also known as the depth of the layer  $l$ ),  $R_{l,j}$  is the (2D) output corresponding to the  $j$ th convolution filter. Note that for the first convolution layer ( $l=1$ ), the input image is considered as  $f_0$ .

- (ii) Batch normalization: During the CNN training, the convolution outputs  $R_{l,j}$  corresponding to all images in a mini batch (of  $S$  images) are considered. In this work, we have used  $S=8$ . The  $R_{l,j}$  is made zero mean with unit variance as follows:

$$\hat{R}_{l,j} = \frac{R_{l,j} - \mu}{\sigma} \quad (5.2)$$

where  $\mu$  and  $\sigma$  are the mean and standard deviation of all  $\{R_{l,j}\}$  in a mini-batch.

The normalized  $\hat{R}_{l,j}$  is scaled with  $\gamma$ , and a bias  $\beta$  is added as follows:

$$y_{l,j} = \gamma \hat{R}_{l,j} + \beta \quad (5.3)$$

Note that Eqs. 5.2 and 5.3 are applied in both training and testing modes. Eq. (5.2) is applied with  $S=8$  (the mini-batch size) and  $S=1$ , in training and testing mode, respectively. The  $\gamma$  and  $\beta$  are trainable parameters and are updated iteratively during the backpropagation.

- (iii) Activation: In this step, an activation function is applied on the batch normalized output  $y_j$ . In this work, the Rectified Linear Unit (ReLU) activation is used. The output of the ReLU activation function  $f_{l,j}$  can be expressed as follows.

$$f_{l,j} = \max(0, y_{l,j}) \quad (5.4)$$

The overall output of convolutional layer  $l$ , which will be passed on to the next layer is as follows:

$$f_l = \{f_{l,j}, j = 0, 1, \dots, N\}$$

In this architecture, the features are extracted in hierarchical levels by using convolutional filters of different sizes. The change on the convolutional filters can precisely locate the object boundaries that need to be segmented. Most existing CNN architectures include pooling layers. In our experiment, it has been found that the pooling leads to loss of the spatial information that carries important texture and shape features of the nuclei. Therefore, the pooling layer has been omitted in the proposed architecture. Table 5.1 shows the number and the size of filters in each layer of the NS-Net architecture. The NS-Net architecture is trained and evaluated using a dataset of 24 high resolution H&E-stained image patches (each with  $1920 \times 2500$  color pixels) obtained from the WSI dataset described in Section 5.2. Each image patch is divided into overlapping blocks of  $64 \times 64$  color pixels to obtain 458 block-images. The total number of block-images will be 10,992 (i.e.  $24 \times 458$ ) and it is divided into 70% for training, 15% for validation and 15% for testing. The entropy loss function with the stochastic gradient descent with momentum (SGDM) optimizer is

used to train the NS-Net architecture [90]. Figure 5.4 (a) shows an input H&E-stained image and (b) shows the masked nuclei image obtained using the NS-Net architecture.

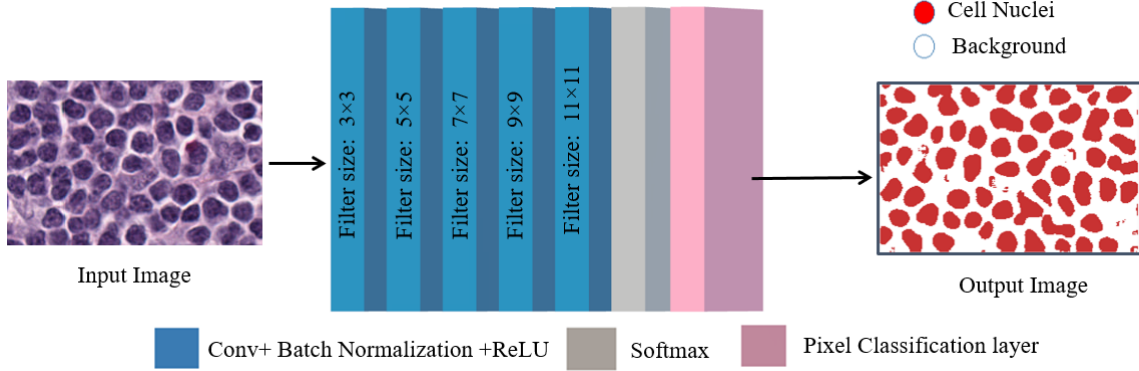


Figure 5.3. The proposed NS-Net architecture for nuclei segmentation.

TABLE 5.1. DETAILS OF THE NS-NET ARCHITECTURE WITH 5 CONVOLUTIONAL LAYERS.

INPUT IMAGE SIZE:  $M \times N$  PIXELS (COLOR). NUMBER OF CLASSES:  $C$ .

	Number of Filters	Number of Channels	Output Image size	Filter size
<b>Layer-1</b>	64	3	$M \times N \times 64$	<b>3×3</b>
<b>Layer-2</b>	64	64	$M \times N \times 64$	<b>5×5</b>
<b>Layer-3</b>	64	64	$M \times N \times 64$	<b>7×7</b>
<b>Layer-4</b>	64	64	$M \times N \times 64$	<b>9×9</b>
<b>Layer-5</b>	$C$	64	$M \times N \times C$	<b>11×11</b>
<b>Softmax layer</b>	-	$C$	$M \times N \times C$	

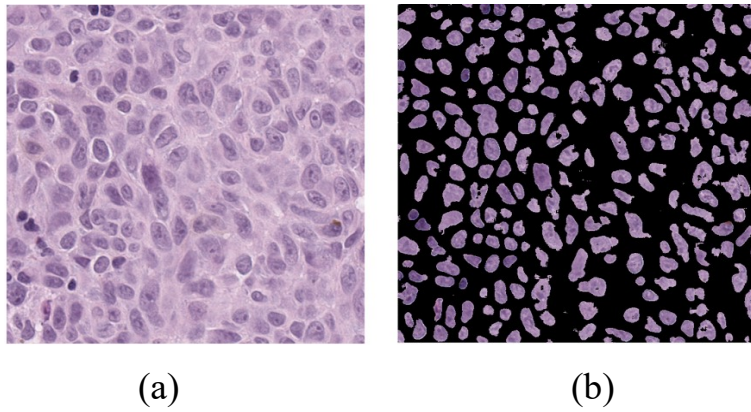


Figure 5.4. Segmentation results. (a) An input image patch (b) the segmented image patch obtained using the NS-Net architecture.

### 5.3.2. Nuclei Classification

In this module, the segmented nuclei obtained using the NS-Net architecture is classified into two classes based on hand-crafted features. The feature vector consists of 18 first-order features, 9 Histogram of Oriented Gradient features, 24 Haralick texture features and 3 Morphological features. The features are extracted for each pre-segmented cell nuclei and described briefly as follows:

- (i) First-order features: it includes six histogram-based features: mean, standard deviation, third moment, smoothness, entropy, and uniformity for 3-channels (R, G and B) to obtain 18 features ( $6 \times 3$ ).
- (ii) Histogram of Oriented Gradient (HOG) features: it measures the gradient of 9 orientations in localized portions of the segmented nuclei image. A  $1 \times 9$  HOG Feature Vector (HOGFVb) is computed for each non-overlapping block of  $8 \times 8$  pixels (from the 64 gradient values). Each segmented cell, depending on the cell size, may contain several HOGFVs. The HOGFVb's from different blocks corresponding to a cell are summed and an overall  $1 \times 9$  HOGFVn is obtained for a cell nucleus. Figure 5.5 shows an example of HOG feature extraction of a cell nucleus. Note that melanoma cells having larger size (compared to other cells) typically contain more HOGFVb's than other cells, and this can result in a large magnitude of HOGFVn's. Also, the HOGFVn's corresponding to the melanoma cells tend to have non-uniform distribution compared to other cells which typically have uniform distribution.
- (iii) Haralick texture features: is calculated from a Gray Level Co-occurrence Matrix, (GLCM). It includes GLCM features such as the correlation, energy, homogeneity, contrast, entropy, and dissimilarity in 4 directions (i.e.,  $0^\circ$ ,  $45^\circ$ ,  $90^\circ$  and  $135^\circ$ ) to obtain 24 features ( $6 \times 4$ ).
- (iv) Morphological features: it includes the eccentricity, solidity, and the ratio of major and minor axes of the cell nuclei to obtain (3) features.



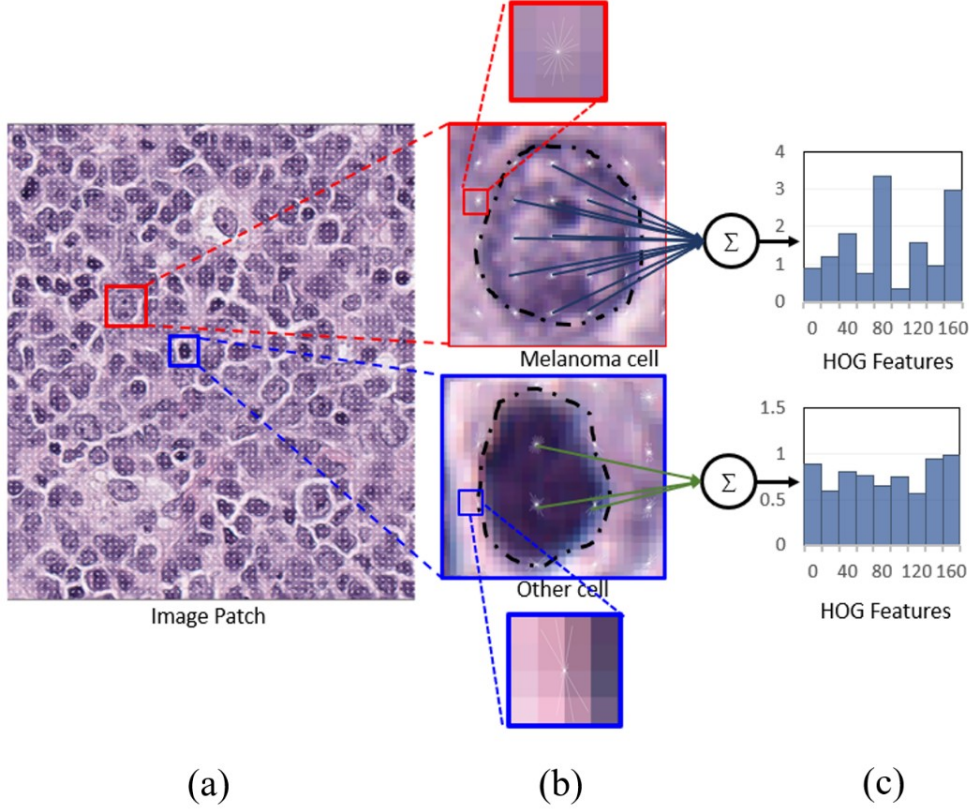


Figure 5.5. Example of HOG feature extraction for a cell nucleus. (a) An image patch with segmented cell nuclei and overlapped gradient orientation. (b) Blown-up of image of two nuclei (melanoma and other cells). (c) The 1x9 HOGFVn's of the cell nuclei.

The extracted feature vectors (with dimension  $1 \times 54$ ) of each cell nuclei are then classified into normal and melanoma using an SVM classifier [54,55]. The SVM is a very efficient supervised classifier that can handle even non-linearly separable features and create hyperplane to separate abnormal features from the normal ones. In the proposed technique, the SVM model is trained and tested on 1,388 cell nuclei (70% for training and 30% for testing) obtained from 9 H&E stained WSI of lymph nodes.

## 5.4. Results and Discussions

In this section, we present the performance of the proposed nuclei segmentation and classification technique. The performance of the segmentation technique is presented first followed by the performance of the classification technique.

#### 5.4.1. Segmentation Performance

The details of the NS-Net training were presented in Section 3.1. The segmentation performance is evaluated using 1,649 H&E-stained lymph node block images (each with 64×64 color pixels). The segmentation performance of the proposed technique is evaluated and compared with handcrafted feature-based algorithms: gLoG+mRLS and Voting+Watershed techniques as well as CNN-based techniques using SegNet and U-Net architectures. The segmentation performance is evaluated using the *Precision*, *Accuracy* and *BF-score* [59] measures defined as follows:

$$Precision = \frac{TP}{TP + FP} \times 100\%$$

$$Accuracy = \frac{TP + TN}{TP + FP + FN + TN} \times 100\%$$

$$BF\ Score = \frac{2 \times TP \times TN}{TP \times TN + 2TN \times FP + TN \times FN} \times 100\%$$

where *TP*, *TN*, *FN* and *FP* denote the number of true positives, true negatives, false negatives and false positives, respectively. Table 5.2 shows the segmentation performance of different techniques. It is observed that the deep learning algorithms provide excellent performance compared to the classical feature-based algorithms. This is because the classical features are less sensitive to the diversity of the cell nuclei in the skin tissue. For example, the melanoma cells tend to have light and inhomogeneous color (see Figure 5.1) and that causes miss detection of the melanoma cells in the gLoG+mRLS and Voting+Watershed techniques.

TABLE 5.2. SEGMENTATION PERFORMANCE OF THE DEEP LEARNING ALGORITHMS AND THE CLASSICAL FEATURE-BASED ALGORITHMS.

Technique:	Precision	Accuracy	BF-Score	Execution time (in s)
Voting+Watershed [44]	78.24	83.64	81.31	143.71
gLoG+mRLS [96]	79.27	76.67	68.46	128.57
SegNet [67]	84.16	87.84	85.81	15.37
U-Net [81]	87.41	78.79	69.63	20.82
NS-Net (proposed)	87.20	90.21	88.52	14.27

In this work, the NS-Net, SegNet and U-Net architectures are trained with the same number of training images. The NS-Net architecture is also evaluated with CNN architecture in terms of the required parameters that need to be trained as shown in Table 5.3.

Figure 5.6 (b)-(f) show the subjective comparison of Voting+Watershed, gLoG+mRLS, SegNet, U-Net and the proposed NS-Net architecture, respectively. It is observed that the NS-Net architecture provides excellent nuclei segmentation, whereas gLoG+mRLS, Voting+Watershed techniques miss a few cell nuclei due to the inhomogeneity in the cell nuclei color. It is also observed that the U-Net architecture does not perform well compared to the other techniques because the overfitting due the large number of the filters that are used in the cell nuclei segmentation.

TABLE 5.3. PROPERTIES OF CNN ARCHITECTURES USED IN PERFORMANCE EVALUATION.

CNN Architecture	Convolutional layers	No. of Trained parameters	Filter size	No. of Filters
SegNet [67]	8	225,542	$3 \times 3$	64
U-Net [81]	11	905,472	$3 \times 3$	(64, 128, 256)
NS-Net	5	150,336	$(3 \times 3)$ - $(11 \times 11)$	64

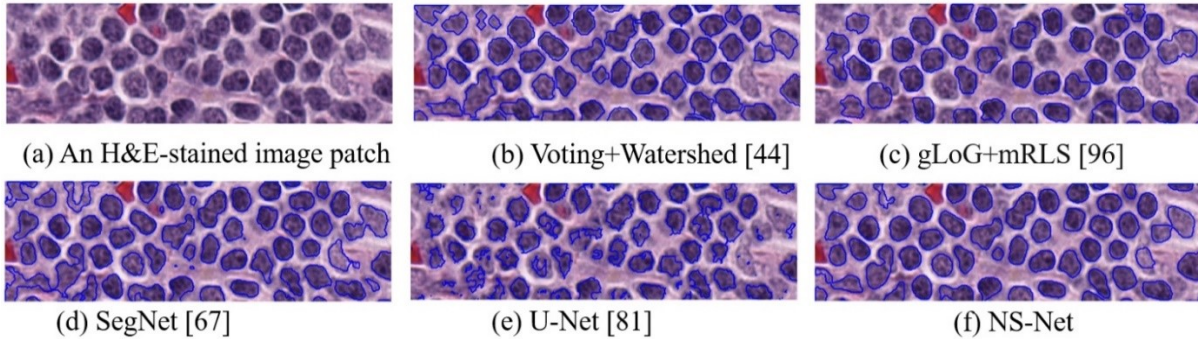


Figure 5.6. Subjective comparison of cell nuclei segmentation results (contoured in blue color) (a) original test image, (b)-(f) Segmentation results for Voting+Watershed, gLoG+mRLS, SegNet, U-Net and NS-Net techniques, respectively.

#### 5.4.2. Classification Performance

The classification performance is evaluated using 240 H&E-stained lymph node nuclei. As explained in Section 3.2, a  $1 \times 54$  size feature vector is obtained for each nucleus. The obtained

1×54 feature vectors include 18 first-order features, 9 Histogram of Oriented Gradient features, 24 Haralick texture features and 3 Morphological features. A nucleus is classified based on its feature vector using the SVM model.

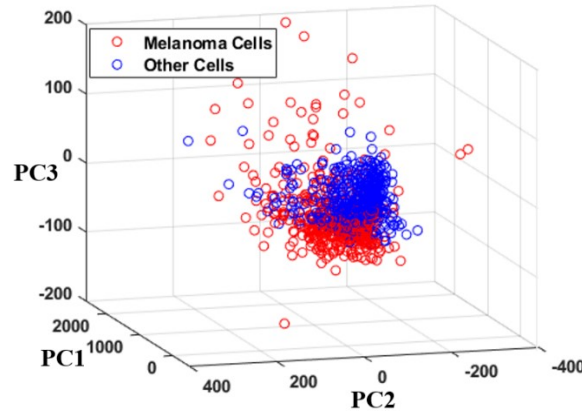


Figure 5.7. Three principal components (PC-1, PC-2, and PC-3) of the 1×54 features.

To demonstrate the discrimination ability of the features, the obtained features are analyzed using Principal Component Analysis (PCA) to capture the data and features variations. The PCA technique is applied on the training cells nuclei (972 cell nuclei: 486 Melanoma and 486 other nuclei). Figure 5.7 visualizes the feature variance of melanoma and other cells with respect to three principal components that are extracted from the nuclei features. Analyzing the feature vectors and the principal components, it has been found that the first principal component (PC1) has high positive association with some of the first order and Haralick features, whereas the second and third principal components have positive association with some of the histogram and morphological features. In this experiment, the first, second and third principal components capture 82% of feature variance. The remaining (51) dimensions add 18% of feature variance. In this work, all 54 features are used for the SVM classification.

TABLE 5.4. PERFORMANCE OF THE NUCLEI CLASSIFICATION USING DIFFERENT SVM KERNELS.

Evaluation Measures	SVM Kernel		
	Linear	Polynomial	Gaussian
Precision	77.43	57.28	80.04
Recall	93.14	96.65	97.42
Accuracy	80.52	57.28	85.72



The classification performance is evaluated in terms of the Precision, Recall and Accuracy defined in Section 5.1. The results are shown in Table 5.4. The SVM classifier has been evaluated with linear, polynomial and Gaussian kernels [90]. It is observed that the SVM classifier with Gaussian kernel provides a superior performance over the other two kernels. Figure 5.8 shows the nuclei classification results obtained using the Gaussian kernel, where the melanoma and non-melanoma nuclei are contoured in red and blue colors, respectively.

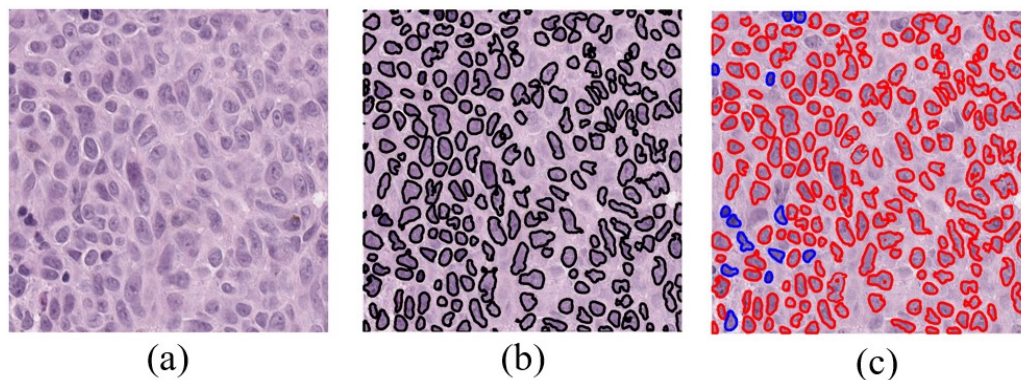


Figure 5.8. Example of classification results. (a) NS-Net input image, (b) NS-Net segmented output image, (c) Classified image obtained using an SVM classifier, where melanocytes and other cell nuclei are contoured with red and blue colors, respectively.

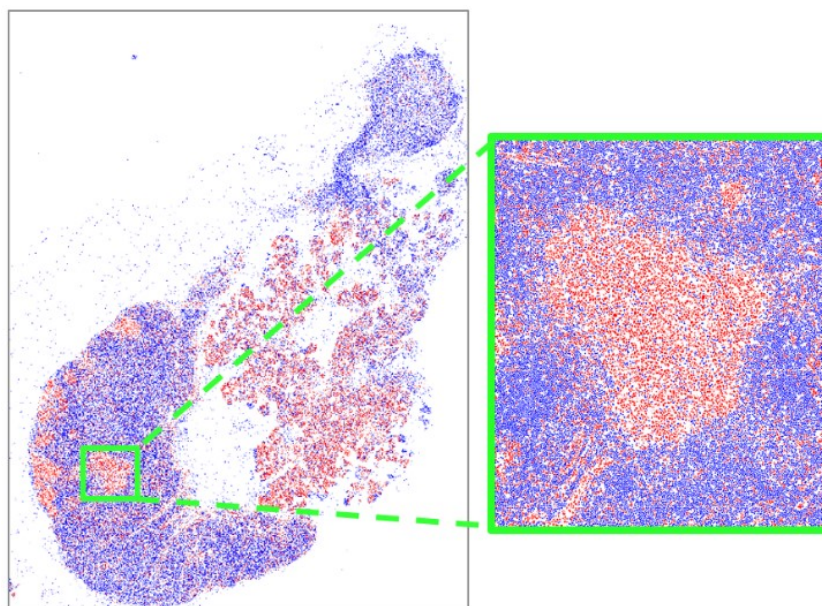


Figure 5.9. Visual example of nuclei segmentation and classification obtained by the proposed technique). The classified melanoma cells are shown in red color, whereas the non-melanoma cells are shown in blue color.

Figure 5.9 shows the segmentation and classification results of the proposed technique for the lymph nodes in Figure 5.1. It is observed that the melanoma cells (in red color) are dense on the melanoma metastasises, whereas the other cells are dense on the normal tissue of the lymph nodes. The dense areas of the melanoma cells can be used to mask the melanoma regions on the lymph node tissue. It is also noticed that there are some areas out of the lymph node tissue containing melanoma cells that can be processed by applying an initial lymph node segmentation technique [80].

## **5.5. Conclusions**

This Chapter proposes an automated technique to detect melanoma nuclei in lymph node histopathological images. The technique segments the cell nuclei in H&E-stained images using a deep learning NS-Net architecture. The NS-Net architecture segments the image into background and cell nuclei regions. The segmented nuclei are then classified into melanoma and other cell nuclei using an SVM classifier with Gaussian kernel. The proposed CNN architecture provides an excellent segmentation performance with a low computational complexity. The future work includes identifying the region of interest (ROI) with clusters of melanoma nuclei and deriving prognostic information such as proliferation index.

# Chapter 6

## Detection of Malignant Melanoma in H&E-stained Images Using Deep Learning Techniques

Histopathological images are widely used to diagnose diseases including skin cancer. As digital histopathological images are typically of very large size, in the order of several billion pixels, automated identification of all abnormal cell nuclei and their distribution within multiple tissue sections would assist rapid comprehensive diagnostic assessment. In this Chapter, we propose a deep learning-based technique to segment the melanoma regions in Hematoxylin and Eosin (H&E) stained histopathological images. In this technique, the nuclei in the image is first segmented using a Convolutional Neural Network (CNN). The segmented nuclei are then used to generate melanoma region masks. Experimental results show that the proposed method can segment the nuclei with more than 90% accuracy and segment the melanoma regions around 96%. The proposed technique has also a low computational complexity.

### 6.1. Introduction

Cutaneous Malignant Melanoma (CMM) is an aggressive type of skin cancer. The early diagnosis of melanoma is very important as it helps to increase the chances of successful treatment and may increase survival rate [1]. The gold standard of the diagnosis is through the examination of histopathological images. The digitized histopathological slides, which are typically obtained by staining and scanning the biopsy slides of the skin tissue, can provide the cell morphological features with a high resolution. The digitized slides are known as Whole Slide Images (WSIs) and with help of computer aided diagnosis techniques that will be useful for the pathologist for diagnosis [2]. Pathologists generally use H&E-stained images, because the morphological features of the melanocytes and other cells become vividly clear. In H&E-stained image, the cell nuclei contain chromatin and that can be observed in the blue shade while the cytoplasm and other connective tissues are observed with the varying shades of pink. Fig. 1 shows an H&E-stained histopathological image of CMM within a cross section of skin tissue. The epidermis layer in the Fig. 6.1 is contoured with green color, and CMM are contoured in brown color. Note that in this

image the CMM are contoured manually by morphology. The skin tissues diagnosed with melanoma typically contain regions of inflammatory cells (as shown in blue contour) near the CMM regions.

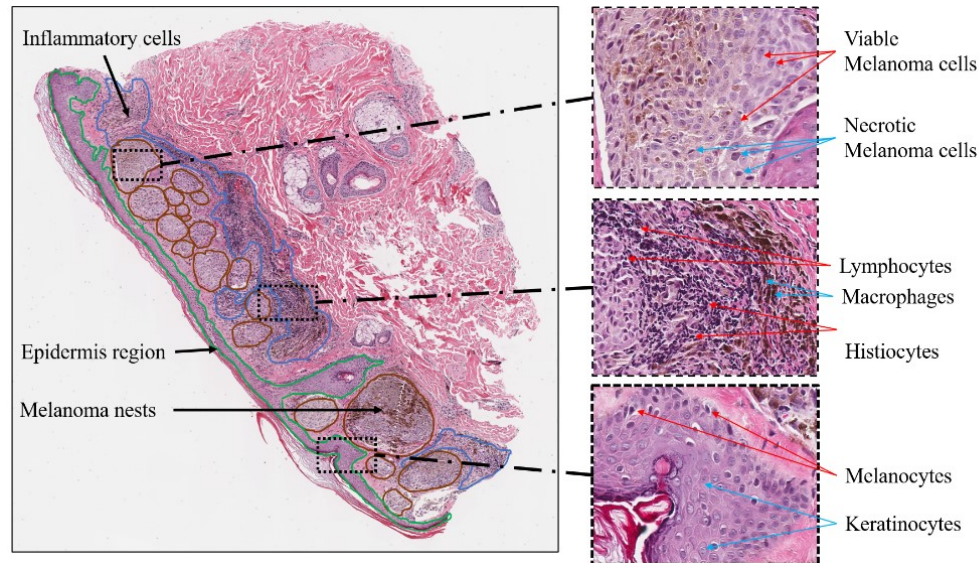


Figure 6.1. Histopathological image of a skin tissue with cutaneous malignant melanoma. The epidermis region, the melanoma nests and inflammatory cells are contoured in green, brown and blue colors, respectively.

TABLE 6.1. CELLS TYPES AND FEATURES ON SKIN TISSUE DIAGNOSED WITH MELANOMA

Cells		Features
<b>Melanoma nests</b>	Viable melanoma cells	Large size*, small dark nucleus inside, irregular boundaries, and light color intensity.
	Necrotic melanoma cells	Small size, large dark nucleus inside, irregular boundaries, and dark color intensity.
<b>Inflammatory cells</b>	Lymphocytes	Small size, large dark nucleus, and elliptical boundaries.
	Histiocytes/ Macrophages	Large size, with dark nucleus, and irregular boundaries. Macrophages work to devour leaking melanin and tend to have dark brown color.
<b>Epidermis cells</b>	Melanocytes	Large size, large dark nucleus, and elliptical boundaries (location: mostly around the Dermis-Epidermic junction).
	Keratinocytes, Langerhans and Merkel	Large size, large dark nucleus, and granular shape.

\* Cells having diameter larger than 15 microns.



In the enlarged patch, it is observed that the abnormal melanocytes appear with irregularity in shape and color intensity [9,10] whereas the inflammatory cells mainly appear in dark color with dense nuclei. Table 6.1 shows cells features in detail that can be shown in skin tissue diagnosed with melanoma. Some research works have been reported for melanoma diagnosis based on histopathological image analysis [27,44,100,101]. These works are focused on detection of nuclei [27], detection of melanocytes [100], and melanoma classification of whole slide images [101]. Xu et al. [44] proposed an automated technique (henceforth referred to as the Watershed+Voting technique) to segment the cell nuclei in H&E-stained images. The technique detects the nuclei seeds by using voting areas and segments the nuclei cells using a watershed algorithm. The technique has been shown to provide a good performance, but it has high computational complexity due the seed detection algorithm. Xu et al. [96] proposed another cell nuclei segmentation technique (henceforth referred to as the gLoG+mRLS technique). This technique first detects the nuclei seeds using the generalized Laplacian of Gaussian (gLoG) filters and then segments the cells using multiple Radial Lines Scanning (mRLS) algorithm. The mRLS uses high gradient pixel locations and shape information to accurately segment the cell nuclei [102].

The nuclei detection techniques [44, 96] mentioned above are generally based on the extracted hand-crafted features that require significant time to calculate. The deep learning algorithms using Convolutional Neural Network (CNN) have recently been used successfully in medical image analysis. Basrinarayanan et al. [67] proposed the SegNet architecture for object segmentation. Ronneberger et al. [81] proposed the U-Net architecture for biomedical image segmentation. Alheejawi et al. [103] proposed a technique (henceforth referred to as the NS-Net+FC technique) to segment and classify the cell nuclei in H&E-stained images. The segmentation is performed by using NS-Net architecture that contain 5 convolutional layers with different filter size. From each segmented nucleus, 54 features are extracted, and these feature vectors are fed to a Support Vector Machine (SVM) for nuclei classification (melanoma or non-melanoma nuclei). Patrik et al. [104] proposed to perform patch-based segmentation of the H&E-stained whole slide image (WSI) for diagnosing colorectal cancer. The proposed patch-based segmentation technique (henceforth referred to as the PBS-ResNet technique) divides a WSI into non overlapping patches of size 64x64 pixels. During training these patches are labelled into 8 classes (e.g., stroma, complex stroma, normal). The ResNet-50 architecture is then trained to classify the patches. Although the patch-based segmentation is fast [104, 105], the technique might generate many false positive patches.

In this Chapter, we propose an automated technique to generate melanoma region masks in H&E-stained images. In the proposed technique, the nuclei are first segmented into melanoma and non-melanoma classes using a CNN architecture. The malignant melanoma regions are then generated by applying a series of morphological operations on the melanoma cells.

The organization of the Chapter is as follows. Section 6.2 describes the dataset used to train and evaluate the proposed technique. Section 6.3 describes the proposed technique in detail. Section 6.4 presents the performance evaluation, followed by the conclusion in Section 6.5.

## 6.2. Data Description

In this section, we present the details of the training and testing dataset to evaluate the performance of the proposed nuclei segmentation and cell classification technique. The digitized biopsies were collected at the Cross Cancer Institute, University of Alberta, Edmonton, Canada in accordance with the protocol for the examination of specimens with skin melanoma. Standard Neutral Buffered formalin-fixed paraffin-embedded tissue blocks of these biopsies were cut into thin slices (e.g., 4 $\mu$ m for light microscope). These slices were then mounted to glass slides and stained using H&E stain [93]. The WSIs were obtained by scanning the H&E slides using aperio scanscope scanning system under 40X magnification. The size of a WSI is typically around 40,000 $\times$ 60,000 pixels (0.25  $\mu$ m/pixel resolution) and each WSI contains thousands of cell nuclei. The image dataset consists of 100 H&E-stained images with size (1000 x 1000 RGB) extracted from 4 WSIs of skin tissue.

## 6.3. Proposed Technique

The schematic of the proposed technique is shown in Figure 6.2 which consists of two modules: CNN-based nuclei segmentation and melanoma region segmentation. The details of these two modules are presented in the following.

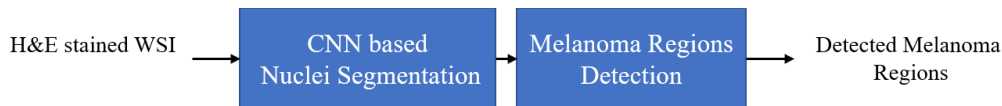


Figure 6.2. Schematic of the proposed melanoma detection technique.

### 6.3.1. CNN-based Nuclei Segmentation

In this module, the H&E-stained image is segmented into three regions: melanoma nuclei, non-melanoma nuclei and background regions. The segmentation is done by using the proposed CNN architecture shown in Figure 6.3. The CNN architecture has 25 convolution layers instead of 5 layers in the NS-Net [103] architecture used for nuclei segmentation. The proposed architecture, henceforth referred to as the improved NS-Net (INS-Net), consists of two paths: path A and path B. Out of 25 layers, 13 layers are in the path A, and 12 layers are in path B. Note that there are five Skip Connections (Skip Conn) in the proposed INS-Net to reduce the gradient vanishing impact. There are 6 types of layers in INS-Net architecture and the details of these layers are explained in the following.

1. C-BN-R layer: This layer includes three operations: Convolution, Batch Normalization, and ReLU activation using the following equations [90,97,98].
2. C-BN-R-P layer: This layer consists of a C-BN-R layer followed by the Pooling operation to reduce the size (width x height) of the feature maps by selecting a pooling window and a stride value. In this Chapter, we have used MAX pooling, window size of 2x2 and a stride of 2x2. Note that the index of the maximum value is sent to the corresponding C-BN-R-UnP layer.
3. C-BN-R-UnP layer: This layer consists of a C-BN-R layer followed by the UnPooling operation to upsample the feature map size (width x height). In this Chapter, an upsampling factor of 2x2 is used. The upsampling is done using the bilinear interpolation. The corresponding index from the C-BN-R-P layer is used to determine the location of the pixel that needs to be upsampled.
4. Concatenate layer: This layer combines the feature maps (of same size) from two or more input layers. The depth of the output layer is equal to the sum of depths of the input layers. In Figure 3 (b), this layer concatenates the output of paths A, B, and C.
5. SoftMax layer: This layer finds the probability values of each pixel for  $K$  classes. Note that each pixel will have  $K$  probability values (In this Chapter,  $K=3$ ) [90].
6. Pixel classification layer: This layer selects the class with the highest value of SoftMax output for each pixel.

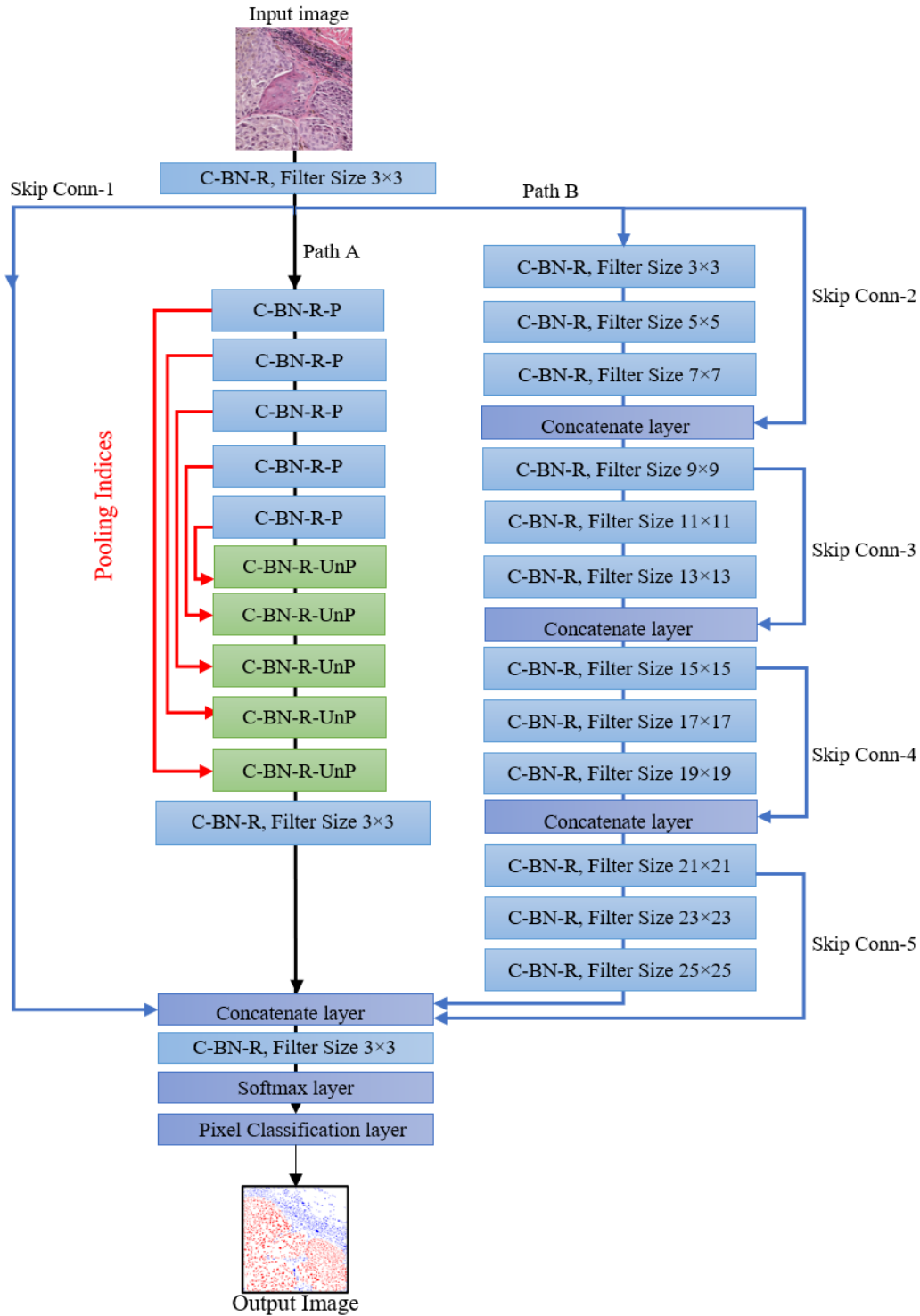


Figure 6.3. The proposed CNN architecture: INS-Net. Note that the output image presents the melanoma, non-melanoma nuclei, and background in red, blue and white colors, respectively.

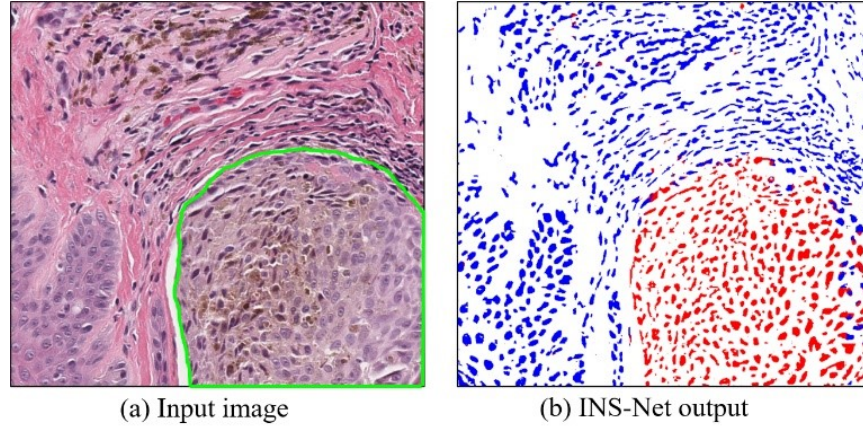


Figure 6.4. Example of (a) an Original RGB Image and (b) the corresponding INS-Net (segmented) output. The melanoma nuclei, non-melanoma nuclei, and the background pixels appear in red, blue and white colors, respectively.

Figure 6.3 shows the proposed CNN-based architecture used to classify the pixels of an H&E-stained image into melanoma nuclei, non-melanoma nuclei, and background pixels. It is observed that Path B is similar to the NS-Net and it is used to extract fine features of the cells and the background, whereas the Path A is used to extract coarse features of the cells and background regions. In this Chapter, the INS-Net architecture is used to segment the H&E-stained image pixels into melanoma nuclei, non-melanoma nuclei, and background pixels.

Figure 6.4 (a) shows an input H&E-stained image and melanoma regions are contoured manually in green contour. The Nuclei Segmentation (NS) mask obtained by using the INS-Net architecture is shown in Figure 6.4 (b). The nuclei segmentation results are very important to determine melanoma regions mask in H&E-stained images. Generally, doctors can determine the depth of melanoma invasion and grade the melanoma based on the melanoma regions. In the next section, we will use the nuclei segmentation results to determine the melanoma regions mask.

### 6.3.2. Melanoma Region Detection (MRD)

This module is used to determine the melanoma regions (MR) from the NS mask obtained using the INS-Net architecture. The MR detection consists of several morphological operations applied on the melanoma nuclei mask (see Figure 6.5 (a)). Note that the melanoma nuclei mask is a binary mask representing the melanoma nuclei class obtained from the NS mask (see the red pixels in Figure 6.4 (b)). The MR detection is done using the following steps.

1. The isolated melanoma nuclei (considered as foreground) in a neighbourhood are merged using the binary *morphological dilation* operation. In this work, a disc structuring element with 7 pixels radius is used. An example output is shown in Figure 6.5(c). The merged regions will include the melanoma nuclei and its neighboring background pixels.
2. Sometimes, there are small, isolated background pixels inside the merged melanoma regions, which can be considered as noise. An *image fill* operation is performed to change these isolated background pixels to foreground pixels.
3. To nullify the effect of size increase, due to the dilation operation, of the melanoma regions in step 1, an *erosion* operation is performed. A disc structuring element with 7 pixels radius is used.
4. Connected melanoma regions with small areas are removed using an *area thresholding* method. In this Chapter, an area threshold of 600 pixels (equivalent to  $150 \mu\text{m}^2$  area) has been used.

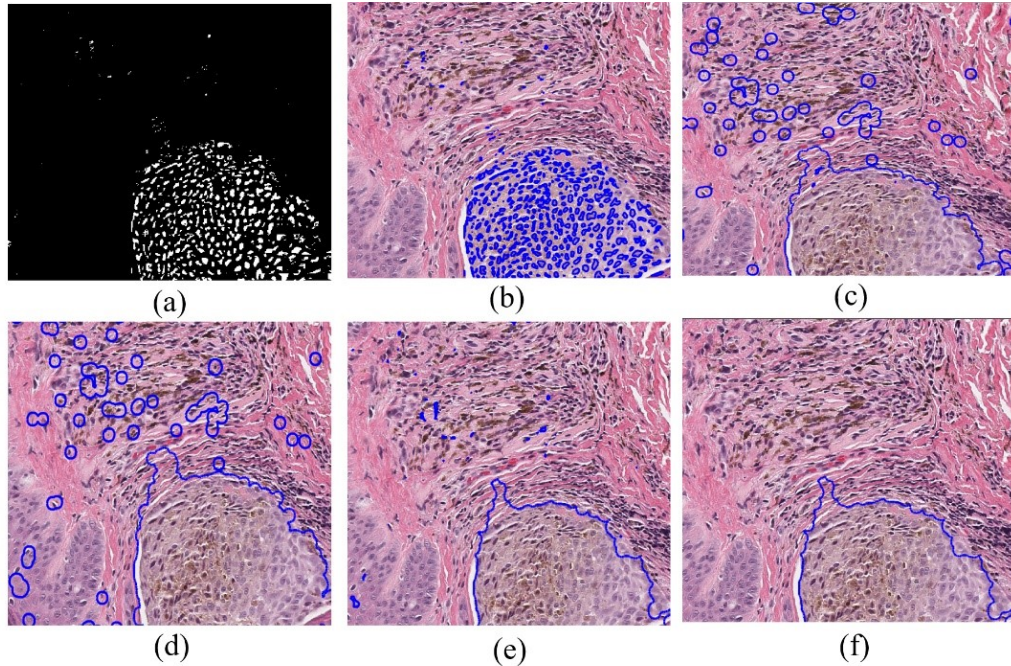


Figure 6.5. Example of intermediate output images of the MRD module. Melanoma nuclei mask (a) obtained using the proposed CNN, (b) melanoma nuclei mask (in blue) superimposed on the original H&E image (c) after *dilation*, (d) after *image fill*, (e) after *erosion*, and (f) after *area thresholding* operations. In Figs. (b)-(f), the intermediate melanoma masks are superimposed on the H&E image to show more insights.

Figure 6.5 shows examples of the intermediate results obtained by the above operations. It is observed that the output of the MRD module shows an excellent melanoma region segmentation compared with the ground truth image shown in Figure 6.4 (a). Note that we also implemented an MR generation technique by applying image closing followed by image fill and area threshold. But the overall performance is not as good as the MRD module.

## 6.4. Results and Discussion

In this section, we present the performance of the proposed technique and compare it with state-of-the-art techniques. The performance of the Nuclei Segmentation module is presented first followed by the performance of MRM module.

### 6.4.1. Nuclei segmentation performance

In this section, the nuclei segmentation mask obtained by the INS-Net will be evaluated. The segmentation performance is evaluated using 30 H&E-stained block images, each with 1000×1000 color pixels. The segmentation performance of the INS-Net is evaluated and compared with handcrafted feature-based algorithms: gLoG+mRLS and Voting+Watershed techniques as well as CNN-based techniques using SegNet, U-Net and NS-Net architectures. The segmentation performance is evaluated using the *Accuracy*, *Precision*, *Recall* (also known as *Sensitivity*), and *Dice score* [59] measures defined as follows:

$$Accuracy = \frac{TP + TN}{TP + FP + FN + TN} \times 100\%$$

$$Precision = \frac{TP}{TP + FP} \times 100\%$$

$$Recall = \frac{TP}{TP + FN} \times 100\%$$

$$Dice\ Score = \frac{2Recall \times Precision}{Recall + Precision} \times 100\%$$

where  $TP$ ,  $TN$ ,  $FN$  and  $FP$  denote the number of true positive, true negative, false negative and false positive pixels, respectively. Table 6.2 shows the segmentation performance of different techniques. It is observed that the deep learning algorithms provide excellent performance compared to the classical feature-based algorithms. This is because the classical features are less sensitive to the diversity of the cell nuclei in the skin tissue. For example, the melanoma cells tend



to have light and inhomogeneous color (see Figure 6.1) and that causes miss detection of the melanoma cells in the gLoG+mRLS and Voting+Watershed techniques.

TABLE 6.2. NUCLEI SEGMENTATION PERFORMANCE ON H&E-STAINED IMAGES.

Techniques	Accuracy	Precision	Recall	Dice score
Voting+Watershed [44]	83.64	78.24	84.64	81.31
gLoG+mRLS [96]	76.67	79.27	60.25	68.46
SegNet [67]	87.84	84.16	87.53	85.81
U-Net [81]	78.79	87.41	57.87	69.63
NS-Net [103]	90.21	87.20	89.90	88.52
INS-Net (proposed)	94.12	90.32	88.05	89.17

In this work, the SegNet, U-Net and NS-Net and the proposed INS-Net architectures are trained with the same number of training images. The configuration of the CNN architectures is shown in Table 6.3. Figure 6.6 shows the subjective comparison of Voting+Watershed, gLoG+mRLS, SegNet, U-Net, NS-Net and the proposed INS-Net architecture. It is observed that the INS-Net architecture provides an excellent nuclei segmentation performance, whereas gLoG+mRLS, Voting+Watershed techniques miss a few cell nuclei due to the inhomogeneity in the cell nuclei color. It is also observed that the U-Net architecture does not perform well compared to the other techniques because the overfitting due the large number of the filters that are used in the cell nuclei segmentation.

TABLE 6.3. CONFIGURATION OF THE CNN ARCHITECTURES USED IN PERFORMANCE EVALUATION. NOTE THAT PBS-RESNET DOES PATCH-BASED SEGMENTATION DIRECTLY AND DOES NOT PERFORM NUCLEI SEGMENTATION.

CNN Architecture	Convolutional layers	No. of Trained parameters	Filter size	No. of Filters per layer
SegNet [67]	8	225,542	3×3	64
U-Net [81]	11	905,472	3×3	(64, 128, 256)
NS-Net [103]	5	150,336	(3×3)- (11×11)	64
PBS-ResNet [104]	53	22676052	(1×1)- (7×7)	(64, 128, 256, 512, 1024, 2048)
INS-Net	18	225,987	(3×3)- (21×21)	64



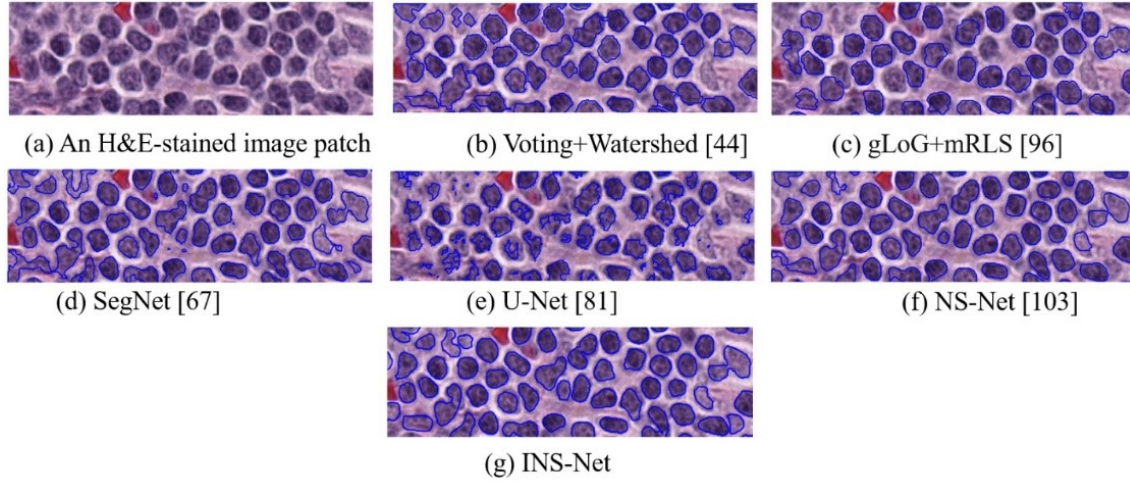


Figure 6.6. Subjective comparison of cell nuclei segmentation results (contoured in blue color) (a) original test image, (b)-(g) Segmentation results for Voting+Watershed, gLoG+mRLS, SegNet, U-Net, NS-Net and the proposed INS-Net techniques, respectively.

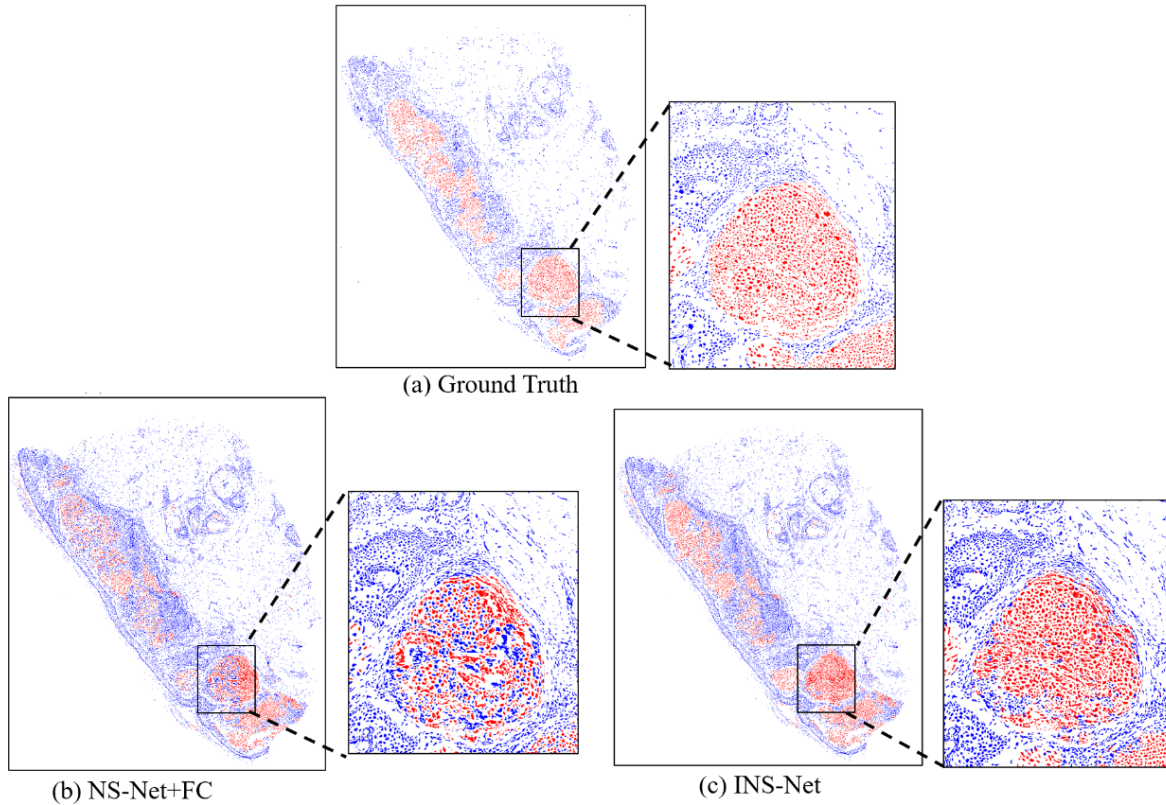


Figure 6.7. Subjective comparison of nuclei classification results of H&E-stained image shown in Figure 5.1. (a) The ground truth image, nuclei classification results of (b) NS-Net+FC, and (c) the proposed INS-Net.

Figure 6.7 shows visual examples of melanoma nuclei classification results using the NS-Net+FC, and the proposed INS-Net compared with ground truth image. In Figure 6.7 (c), it is observed that the INS-Net has better nuclei classification results compared to the NS-Net+FC outputs shown in Figure 6.7 (b). The mis-classification results of the melanoma nuclei can impact negatively on the obtained melanoma regions detected by the MRD module. Note that accurate melanoma nuclei classification results are important to obtain a good MR detection performance by the MRD module.

#### 6.4.2. Melanoma Region Detection performance

In this section, the intermediate output images of the MRD module are evaluated after each operation. The melanoma segmentation performance of the proposed INS-Net+MRD is then compared with output of PBS-ResNet [104] and NS-Net+FC+MRD techniques.

The subjective comparison of the MRD module in the NS-Net+FC+MRD technique and the proposed INS-Net+MRD technique are shown in Figure 6.8. It is observed that the overall melanoma region detection performance of the proposed technique is superior to that obtained by the NS-Net+FC+MRD technique. This is primarily because the accuracy of the melanoma nuclei classification of the NS-Net+FC technique is not very high.

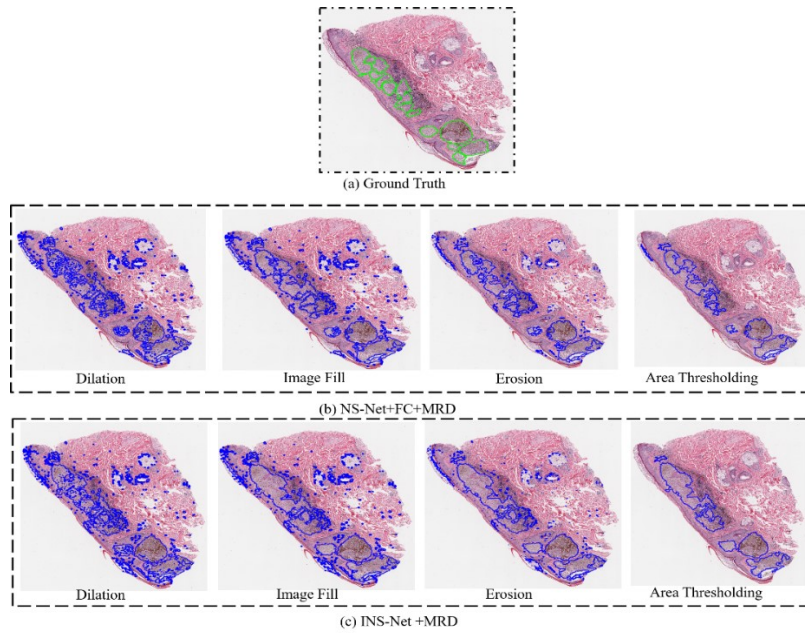


Figure 6.8. Subjective comparison of MRD results (a) The ground truth image (b) Melanoma detection using NS-Net+FC+MRD technique and (c) Melanoma detection using INS-Net+MRD technique.

The MRD module is now objectively evaluated in terms of Accuracy, Precision, Recall, and Dice score. Table 6.4 shows the ablation study of different steps for the melanoma segmentation performance of the MRD module. It is observed that the performance improves with each added step. The overall performance of the MRD module (with all four steps) is shown in the last row of the table. It is observed that the Dice score of 83.81% is achieved by the MRD module.

TABLE 6.4. MELANOMA SEGMENTATION PERFORMANCE OF VARIOUS STEPS OF THE MRD MODULE.

Steps	Accuracy	Precision	Recall	Dice Coefficient
Dilation	95.14	80.27	49.87	61.55
Dilation+Image Fill	94.66	69.88	88.25	78.00
Dilation+ImageFill+Erosion	95.80	76.35	85.97	80.88
Dilation+ImageFill+Erosion+AreaThresh	97.70	83.22	87.08	85.10

The melanoma regions detected by the proposed INS-Net+MRD technique are now compared with those obtained by the state-of-the-art techniques: PBS-ResNet [104] and NS-Net+FC+MRD. In the PBS-ResNet, the H&E whole slide image is first divided into non-overlapping blocks of size 64x64 (RGB) pixels. Each block is then classified into melanoma, non-melanoma, and background blocks using the ResNet-50 CNN classifier. The ResNet-50 CNN classifier has been trained with 19,016 images for each of the three classes. In the NS-Net+FC+MRD technique, the melanoma nuclei in a H&E whole slide image are detected using the NS-Net+FC technique [103], which uses NS-Net for the nuclei segmentation followed by nuclei classification (to detect the melanoma nuclei) using SVM. The detected melanoma nuclei are then passed through the MRD module to obtain the melanoma regions.

Figure 6.9 shows a visual example of the melanoma region detection on the H&E skin whole slide image shown in Figure 6.1. The PBS-ResNet generates a significant number of FP and FN regions throughout the image due to the misclassification of patches (of size 64x64). The NS-Net+FC+MRD generates a significant number of FP and FN pixels due to the misclassification of melanoma nuclei. On the other hand, it is observed that the INS-Net+MRD provides a superior segmentation performance. This is because the technique first classifies the melanoma nuclei and builds the melanoma region by merging the detected nuclei, resulting in a superior performance.

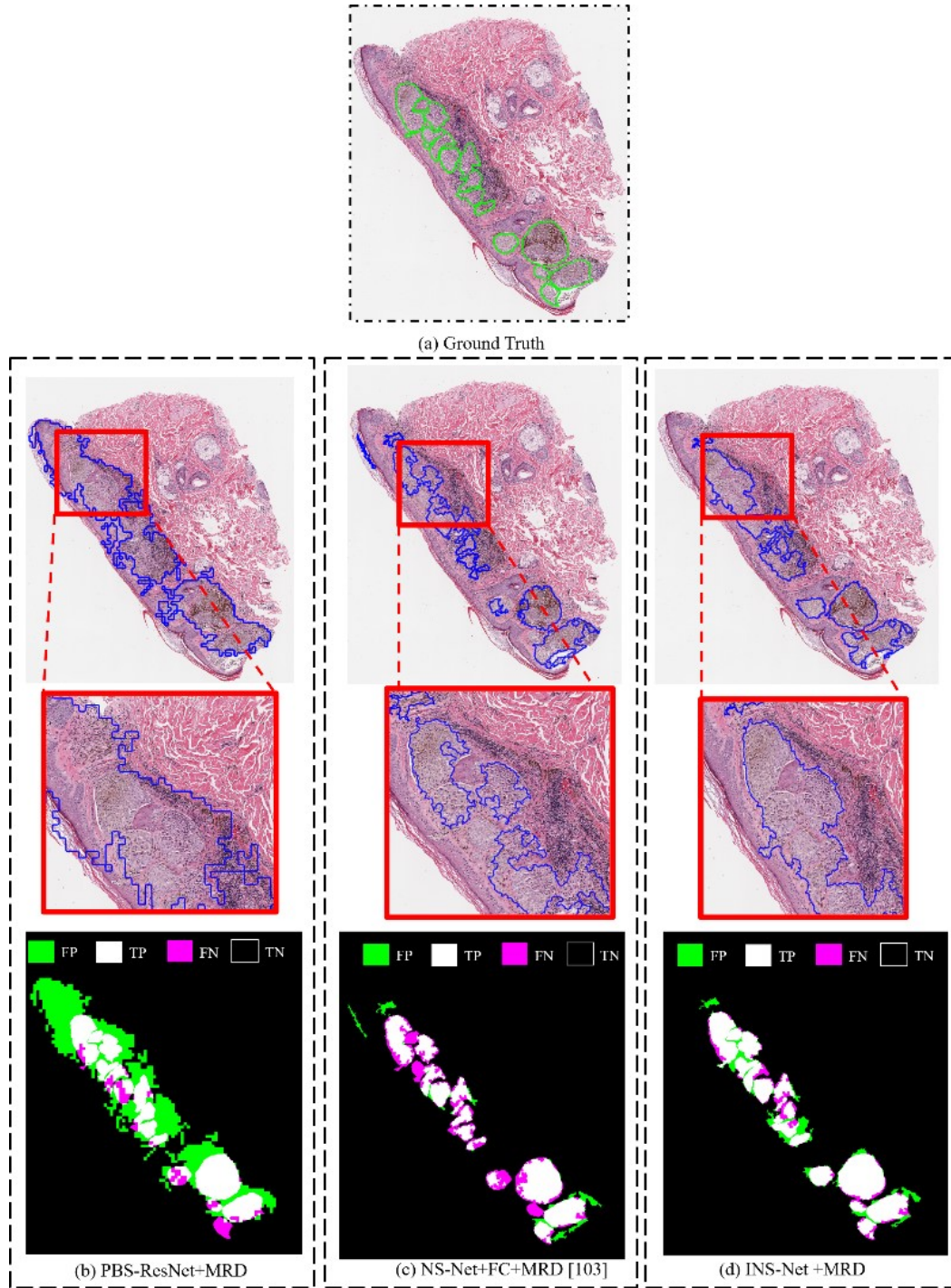


Figure 6.9. Subjective comparison of the detected melanoma regions. (a) The ground truth segmentation mask (green contour), melanoma regions detected by (b) PBS-ResNet, (c) NS-Net+FC+MRD, and (d) INS-Net+MRD. The melanoma regions are shown with blue contour. The last row shows the FP (green), TP (white), FN (red) and TN (black) regions.



The segmentation performance is now compared objectively with respect to accuracy, precision, recall, Dice score (defined before) as well as Jaccard index as defined below.

$$Jaccard\ Score = \frac{TP}{TP + FP + FN} \times 100\%$$

Table 6.5 shows the melanoma segmentation performance of the proposed technique and two state of the art techniques. It is observed that the proposed INS-Net+ MRD has superior results in terms of Precision, and Accuracy compared with the PBS-ResNet and NS-Net +FC+ MRD techniques. The INS-Net+MRD shows the best performance compared with the PBS-ResNet and NS-Net+FC+MRD techniques. The computational complexity of various melanoma region detection techniques is now compared in terms of the execution time as shown in the last column of Table 6.4. The average execution time (for both nuclei segmentation and melanoma detection) for a WSI in testing mode is calculated. In this Chapter, all techniques were implemented using MATLAB R2020a and run on a Windows 10 workstation with Intel i7-6700K CPU, 12 GB RAM, and NVIDIA GeForce GTX 745 graphic card. Note that the CNNs were implemented using the Deep Network Designer Toolbox.

The PBS-ResNet [24] requires the lowest execution time (about 184 seconds) as it classifies the patches directly. On the other hand, the NS-Net+FC+MRD [103] requires the highest execution time (about 1034 seconds). Note that in this technique the FC (for Feature extraction and Classification) takes about 50% of the overall execution time. The CNN segmentation architecture requires more time compared with the CNN classifiers as the CNN segmentation classifies each pixel in the image instead of classifying the whole patch. The proposed INS-Net+MRD technique also requires a long execution time (about 402 seconds) due to the nuclei-based segmentation. However, an increase in the computational complexity is offset by the superior melanoma region detection performance of the proposed technique.

TABLE 6.5. MELANOMA REGION DETECTION PERFORMANCE.

Technique	Accuracy	Precision	Recall	Dice score	Jaccard score	Exec time (in s)
PBS-ResNet+MRD [104]	89.78	68.14	83.88	75.19	66.26	184
NS-Net+FC+MRD <sup>1</sup> [103]	95.521	80.11	84.36	81.95	70.21	1034
INS-Net+MRD (proposed)	<b>97.70</b>	<b>83.22</b>	<b>87.08</b>	<b>85.10</b>	<b>74.07</b>	402

<sup>1</sup>MRD has been added to [103] for generating the melanoma regions.

## **6.5. Conclusions**

This Chapter proposes an automated technique to detect melanoma regions in skin tissue image stained with H&E. The technique segments the cell nuclei in H&E-stained image using a deep learning INS-Net architecture. The INS-Net architecture segments the image into melanoma nuclei, non-melanoma nuclei and background regions. The segmented melanoma nuclei are then used to generate a melanoma mask using the MRD module. The proposed technique provides an excellent segmentation performance with a low computational complexity. The future work includes measuring the melanoma depth on skin tissue on H&E-stained images.

# Chapter 7

## Conclusions and Future Research Directions

In recent decades, image analysis and machine learning techniques have been very useful tools for assisting pathologists to grade and diagnose different diseases. In this thesis, several techniques have been proposed to grade and detect skin cancer in histopathological images. These techniques can provide a quantitative analysis of skin and lymph biopsy images. In this chapter, we summarize the main contributions in this thesis and discuss a few future research directions.

### 7.1. Main Contributions

Four CAIA systems are proposed to detect and grade melanoma regions in skin and lymph node histopathological images. The contributions of this thesis are summarized in the following.

Chapter 3 presented the first CAIA system to grade melanoma by calculating the PI values on lymph node tissue. The proposed technique segments the lymph nodes on biopsy images generated with different stains. It also detects the melanoma regions on a MART-1 stained image. The segmented melanoma region is then mapped on the corresponding Ki-67-stained image. The PI values are calculated by applying the Otsu threshold to segment the nuclei in the melanoma region on Ki-67 images. The segmented nuclei regions are then classified into passive and active nuclei using a SVM classifier. The proposed CAIA system shows an excellent performance compared with ground truth data.

Chapter 4 presented an automated technique to calculate the PI using a CNN based algorithm. The proposed CNN segments Ki-67-stained images into three classes: active nuclei, passive nuclei and background regions. The proposed CNN consists of three Paths: Path A, Path B and Path C. The Path A is used to extract fine features of nuclei, whereas the Path B is used to extract coarse segmentation of nuclei. The proposed technique achieves a superior performance compared with state-of-the-art techniques such as PI-SegNet, PI-UNet and DeepLab.

Chapter 5 presented a technique to classify the nuclei in H&E-stained lymph node images into melanoma and non-melanoma nuclei. The proposed technique used a CNN followed by an SVM classifier. The CNN architecture segments an H&E-stained image into two regions: nuclei and

background regions. The SVM classifier then classifies each nuclei region into melanoma and non-melanoma. Experimental results show that the CNN can segment the nuclei with more than 90% accuracy. The proposed technique has a low computational complexity.

Chapter 6 presented a technique to detect the melanoma regions on H&E-stained skin images. The technique used a CNN followed by an MRD module to detect melanoma regions. The CNN architecture is used to segment the H&E-stained images into three classes: melanoma nuclei, non-melanoma, and background regions. The MRD module is then used to detect the melanoma regions by applying a series of morphological operations. Experimental results show that the proposed method can segment the nuclei with more than 90% accuracy and detecting the melanoma regions with around 96% accuracy.

## **7.2. Future Research Directions**

Although this thesis has developed several key techniques for automated analysis of skin biopsy images, there are many research directions in which this work can be extended to assist pathologists in real clinical settings. A few future research directions are presented in the following.

### **Detection of Melanocytes in H&E-Stained Image**

It is difficult to detect melanoma in a H&E-stained image as melanocytes visually look like any other keratinocytes in the WSI. That is why to confirm melanoma, pathologists use MART-1-stained image as MART-1 can detect melanocytes with high specificity. Unfortunately, MART-1 staining is not available everywhere and is also costly. It would be helpful to develop machine learning techniques to detect melanocytes accurately in H&E-stained image.

### **Proliferation Index Calculation using H&E and Ki-67 stains**

After an efficient machine learning technique is developed to detect melanocytes in H&E-stained image, the next task will be to develop a technique for calculating proliferation index values by analyzing H&E and Ki-67 stained WSI. This will simplify the techniques proposed in Chapters 3 and 4 and reduce the cost as well. The technique will be able to detect melanoma even in the presence of nevus.



### **Grading of Melanoma using PD-L1 score**

The immune system consists of bone marrow, spleen, thymus and lymph nodes (see Figure 1.5 in Chapter 1). The PD-L1 score, calculated by analyzing active T-cells, is often used by the doctors to determine the immune therapeutic response of a patient. The future research can develop a technique to calculate the ratio of melanoma cells that generate PD-L1 protein to the total number of cells in the tissue using PD-L1 WSI. This would help the doctors to determine the immune therapeutic response of a patient.

### **Anomaly detection**

The anomaly detection can be a very useful tool in clinical practice to help doctors to pay more attention to anomaly (or abnormality) present in histopathological images. This can be carried out in two stages. In the first stage, an efficient machine learning technique can be developed to detect the anomaly patterns, textures, and suspicious shapes in histopathological images. Once an anomalous histopathological slide is detected, doctors can use the developed techniques in the second stage to obtain quantitative analysis of the tissue.

# References

- [1] American Cancer Society “Cancer Facts and Figures 2018” [Online]. Available: <https://www.cancer.org/content/dam/cancer-org/research/cancer-facts-and-statistics/annual-cancer-facts-and-figures/2018/cancer-facts-and-figures-2018.pdf>.
- [2] I. Maglogiannis and C. Doukas, “Overview of advanced computer vision systems for skin lesions characterization,” *IEEE Transactions on Information Technology in Biomedicine*, vol. 13, no. 5, pp. 721–733, 2009.
- [3] R. Rubin, D. S. Strayer, E. Rubin et al., *Rubin’s pathology: clinicopathologic foundations of medicine*. Lippincott Williams & Wilkins, 2008.
- [4] F. Dick, S. VanLier, P. Banks, G. Frizzera, G. Wittrak, R. Gibson, G. Everett, L. Schuman, P. Isacson, G. O’Conor et al., “Use of the working formulation for non-hodgkin’s lymphoma in epidemiologic studies: agreement between reported diagnoses and a panel of experienced pathologists,” *Journal of the National Cancer Institute*, vol. 78, no. 6, pp. 1137–1144, 1987.
- [5] O. Sertel, “Image analysis for computer-aided histopathology,” Ph.D. dissertation, The Ohio State University, 2012.
- [6] I. Wikimedia Foundation, “Wikipedia, the free encyclopedia,” website, June 2015. [Online]. Available: <https://en.wikipedia.org/?title=Histology>
- [7] D. E. Chandler and R. W. Roberson, *Bioimaging: current concepts in light and electron microscopy*. Jones & Bartlett Publishers, 2009.
- [8] I. Wikimedia Foundation, “Wikipedia, the free encyclopedia,” website, June 2015. [Online]. Available: <https://en.wikipedia.org/wiki/Histopathology>
- [9] M. G. Rojo, A. M. Castro, and L. Goncalves, “Cost action eurotelepath: digital pathology integration in electronic health record, including primary care centres,” *Diagnostic Pathology*, vol. 6, no. Suppl 1, pp. S1–6, 2011.
- [10] R. S. Weinstein, A. R. Graham, L. C. Richter, G. P. Barker, E. A. Krupinski, A. M. Lopez, K. A. Erps, A. K. Bhattacharyya, Y. Yagi, and J. R. Gilbertson, “Overview of telepathology, virtual microscopy, and whole slide imaging: prospects for the future,” *Human pathology*, vol. 40, no. 8, pp. 1057–1069, 2009.

- [11] R.J. Friedman, D.S. Rigel, A.W. Kopf. "Early detection of malignant melanoma: the role of physician examination and self-examination of the skin". CA Cancer J Clin. 1985; 35:130–151.
- [12] D. ADRIANA. Online, "You go on holiday? Protect yourself from skin cancer!" Website, June 2017. [Online]. Available: <https://www.topdoctors.mx>.
- [13] N. V. Online, "Skin anatomy,"Website, June 2015. [Online]. Available: <http://www.cancer.gov>
- [14] L. U. Chicago, "Introduction to the skin," Website, 1996. [Online]. Available: <http://www.meddean.luc.edu/lumen/MedEd/medicine/dermatology/melton/skinlsn/sknlsn.htm>
- [15] N. Noroozi and A. Zakerolhosseini, "Computerized measurement of melanocytic tumor depth in skin histopathological images," Micron, vol. 77, pp. 44–56, 2015.
- [16] H. Xu and M. Mandal. "Epidermis segmentation in skin histopathological images based on thickness measurement and k-means algorithm", EURASIP Journal on Image and Video Processing, vol.2015, no.1, pp.1-14, 2015.
- [17] H. Xu, R. Berendt, N. Jha and M. Mandal, "Automatic measurement of melanoma depth of invasion in skin histopathological images", Micron, vol.97, pp.56-67, 2017.
- [18] G. Pocock, C.D. Richards, and D. A. Richards (2006). Human physiology: the basis of medicine (3rd ed.). Oxford: Oxford University Press. pp. 252–253. ISBN 978-0-19-856878-0.
- [19] "Lymph Nodes Directory". [www.webmd.com](http://www.webmd.com).
- [20] C. Balch, J. Gershenwald, M. Atkins, A. Buzaid, N. Cascinelli, A. Cochran et al. Melanoma of the skin. In: S. Edge, D. Byrd, C. Compton, A. Fritz, F. Greene, A. Trotti, editors, "AJCC cancer staging manual". 7th ed. New York: Springer; 2010. pp. 325–344.
- [21] A. Giuliano, D. Kirgan, J. Guenther, et al. "Lymphatic mapping and sentinel lymphadenectomy for breast cancer". Annals of Surgery, vol. 220, no. 3, pp. 391-401, Sep. 1994.
- [22] K. Nawaz, M. Khaja and R. Nazriya, "Reliability of sentinel lymph node biopsy in head and neck squamous cell carcinoma", International Journal of Otorhinolaryngology and Head and Neck Surgery, vol. 2, no. 2, pp. 105-109. 2016.
- [23] D. Hanahan, and R. Weinberg, "Hallmarks of Cancer: The Next Generation". Cell, vol. 144, no. 5, pp. 646-674, 2011.
- [24] S. Bruno, and Z. Darzynkiewicz "Cell cycle dependent expression and stability of the nuclear protein detected by Ki-67 antibody in HL-60 cells". Cell Proliferation, vol. 25, no. 1, pp. 31-40, Jan. 1992.

- [25] M. Mokhtari, M. Rezaeian, S. Gharibzadeh, and V. Malekian, "Computer aided measurement of melanoma depth of invasion in microscopic images," *Micron*, vol. 61, pp. 40–48, 2014.
- [26] C. Lu, M. Mahmood, N. Jha, and M. Mandal, "Automated segmentation of the melanocytes in skin histopathological images," *IEEE Journal of Biomedical and Health Informatics*, vol. 17, no. 2, pp. 284–296, 2013.
- [27] C. Lu, M. Mahmood, N. Jha, and M. Mandal, "A robust automatic nuclei segmentation technique for quantitative histopathological image analysis," *Analytical and Quantitative Cytology and Histology*, vol. 34, pp. 296–308, 2012.
- [28] S. Ismail, A. Colclough, J. Dinnen, D. Eakins, D. Evans, E. Gradwell, et al. "Observer variation in histopathological diagnosis and grading of cervical intraepithelial neoplasia," *BMJ: Br. Med. J.* vol. 298, no. 6675, pp. 707-710, Mar. 18, 1989.
- [29] H. Ahmady, D. Goldgof and L. Hall "Nucleus Segmentation in Histology Images with Hierarchical Multilevel Thresholding" Conference: SPIE Medical Imaging, 23 March 2016.
- [30] N. Otsu, "A threshold selection method from gray-level histograms," *Systems, Man and Cybernetics*, *IEEE Transactions on* 9, 62–66 (Jan 1979).
- [31] P. Liao, T. Chen and P. Chung "A Fast Algorithm for Multilevel Thresholding". *J. Inf. Sci. Eng.* 17 (5): 713–727 (2001).
- [32] M. Kass, A. Witkin, D. Terzopoulos "Snakes: Active contour models". *International Journal of Computer Vision.* 1 (4): 321 (1988).
- [33] C. Xu and J.L. Prince, "Gradient Vector Flow: A New External Force for Snakes," *Proc. IEEE Conf. on Comp. Vis. Patt. Recog. (CVPR)*, Los Alamitos: Comp. Soc. Press, pp. 66–71, June 1997.
- [34] D. Cremers, C. Schnorr, J. Weickert, "Diffusion-snakes: combining statistical shape knowledge and image information in a variational framework". *Proceedings. IEEE Workshop on.* 50: 137–144.
- [35] X. Qi, F. Xing, D. J. Foran, and L. Yang, "Robust segmentation of overlapping cells in histopathology specimens using parallel seed detection and repulsive level set," *IEEE Transactions on Biomedical Engineering*, vol. 59, no. 3, pp. 754–765, 2012.
- [36] S. Ali and A. Madabhushi, "An integrated region-, boundary-, shape-based active contour for multiple objects overlap resolution in histological imagery," *IEEE Transactions on Medical Imaging*, vol. 31, no. 7, pp. 1448– 1460, 2012.

- [37] H. Fatakdawala, J. Xu, A. Basavanthally, G. Bhanot, S. Ganesan, M. Feldman, J. Tomaszewski, A. Madabhushi, "Expectation Maximization driven Geodesic Active Contour with Overlap Resolution (EMaGACOR): Application to Lymphocyte Segmentation on Breast Cancer Histopathology," *Biomedical Engineering, IEEE Transactions on*, vol.57(7), pp. 1676-1689, 2010.
- [38] A. Hafiane, F. Bunyak and K. Palaniappan, "Clustering initiated multiphase active contours and robust separation of nuclei groups for tissue segmentation," 2008 19th International Conference on Pattern Recognition, Tampa, FL, 2008, pp. 1-4.
- [39] K. Yadanar Win, S. Choomchuay and K. Hamamoto, "K mean clustering based automated segmentation of overlapping cell nuclei in pleural effusion cytology images," 2017 International Conference on Advanced Technologies for Communications (ATC), Quy Nhon, 2017, pp. 265-269.
- [40] A. S. Abdul Nasir, M. Y. Mashor and H. Rosline, "Unsupervised colour segmentation of white blood cell for acute leukaemia images," 2011 IEEE International Conference on Imaging Systems and Techniques, Penang, 2011, pp. 142-145.
- [41] P. Shi, J. Zhong, J., and J. Hong "Automated ki-67 quantification of immunohistochemical staining image of human nasopharyngeal carcinoma xenografts" *Scientific Reports* 6 (2016).
- [42] H. Z. Al-Lahham, R. S. Alomari, H. Hiary, and V. Chaudhary "Automating proliferation rate estimation from ki-67 histology images" In *SPIE Medical Imaging 83152A–83152A* (International Society for Optics and Photonics, 2012).
- [43] O. Sertel, J. Kong, U. V. Catalyurek, G. Lozanski, J. H. Saltz, and M. N. Gurcan, "Histopathological image analysis using model-based intermediate representations and color texture: Follicular lymphoma grading," *Journal of Signal Processing Systems for Signal Image and Video Technology*, vol. 55, no. 1-3, pp. 169–183, 2009.
- [44] H. Xu, C. Lu, and M. Mandal, "An efficient technique for nuclei segmentation based on ellipse descriptor analysis and improved seed detection algorithm," *IEEE Journal of Biomedical and Health Informatics*, vol.18, no.5, pp.1729-1741, 2014.
- [45] R. Edulapuram, R. Stanley, R. Long, S. Antani, G. Thoma, R. Zuna, W. Stoecker and J. Hagerty "Nuclei Segmentation using a Level Set Active Contour Method and Spatial Fuzzy C-means Clustering" 12th International Joint Conference on Computer Vision, Imaging and Computer Graphics Theory and Applications (VISIGRAPP 2017), pages 195-202.

- [46] M. Datar, N. Immorlica, P. Indyk, V.S. Mirrokni. SoCG. ACM; 2004. Locality-sensitive hashing scheme based on p-stable distributions. pp. 253–262.
- [47] L. Wei, Q. Gan & Tao Ji “Cervical cancer histology image identification method based on texture and lesion area features”, *Computer Assisted Surgery*, 22:sup1, 186-199, 2017.
- [48] V. Ojansivu, J. Heikkilä Blur insensitive texture classification using local phase quantization *Proceedings of the International Conference on Image and Signal Processing (ICISP 08)*, Springer Press (2008) pp. 236–243.
- [49] S. Korkmaz, H. Binol, Classification of molecular structure images by using ANN, RF, LBP, HOG, and size reduction methods for early stomach cancer detection, *Journal of Molecular Structure*, Volume 1156, 2018, Pages 255-263.
- [50] R. L. Graham, “An efficient algorithm for determining the convex hull of a finite planar set,” *Information processing letters*, vol. 1, no. 4, pp. 132–133, 1972.
- [51] M. Fitzgibbon, A.W. and Pilu and R. B. Fisher, “Direct least-squares fitting of ellipses,” *IEEE Transactions on Pattern Analysis and Machine Intelligence*, vol. 21, no. 5, pp. 476–480, May 1999.
- [52] Y. Wang, D. Crookes, O. S. Eldin, S. Wang, P. Hamilton, and J. Diamond, “Assisted diagnosis of cervical intraepithelial neoplasia (cin),” *IEEE Journal of Selected Topics in Signal Processing*, vol. 3, no. 1, pp. 112– 121, 2009.
- [53] J. Miedema, J. S. Marron, M. Niethammer, D. Borland, J. Woosley, J. Coposky, S. Wei, H. Reisner, and N. E. Thomas, “Image and statistical analysis of melanocytic histology,” *Histopathology*, vol. 61, no. 3, pp. 436–444, 2012.
- [54] A. Ben-Hur, D. Horn, H. Siegelmann, and V. Vapnik, "Support vector clustering," *Journal of Machine Learning Research*, vol. 2, pp. 125-137, 2001.
- [55] C. Bishop, “Pattern Recognition and Machine Learning”, Appendix E, Springer, 2006. S.Y. Kung, M.W. Mak and S.H. Lin, *Biometric Authentication: A Machine Learning Approach*, Prentice Hall, 2005, Chapter 4.
- [56] W. McCulloch, P. Walter (1943). "A Logical Calculus of Ideas Immanent in Nervous Activity". *Bulletin of Mathematical Biophysics*. 5 (4): 115–133.
- [57] F. Rosenblatt (1958). "The Perceptron: A Probabilistic Model for Information Storage and Organization in The Brain". *Psychological Review*. 65 (6): 386–408.

- [58] J. Schmidhuber, (2015). "Deep Learning in Neural Networks: An Overview". *Neural Networks*. 61: 85–117.
- [59] G. Csurka, D. Larlus, and F. Perronnin. "What is a good evaluation measure for semantic segmentation?" *Proceedings of the British Machine Vision Conference*, 2013, pp. 32.1-32.11.
- [60] B. Grala, T. Markiewicz, W. Kozłowski, S. Osowski, J. Słodkowska, W. Papierz "New automated image analysis method for the assessment of ki-67 labeling index in meningiomas" *Folia histochemica et cytochemica*, vol. 47, pp. 587–592, 2009.
- [61] H. Akakin, H. Kong, C. Elkins, J. Hemminger, B. Miller, J. Ming, E. Plocharczyk, R. Roth, M. Weinberg, R. Ziegler, G. Lozanski, M. Gurcan "Automated detection of cells from immunohistochemically-stained tissues: application to ki-67 nuclei staining", *SPIE Medical Imaging*, vol. 8315 (International Society for Optics and Photonics, 2012.
- [62] H. Al-Lahham, R. Alomari, H. Hiary, V. Chaudhary, "Automating proliferation rate estimation from ki-67 histology images" In *SPIE Medical Imaging 8315* (International Society for Optics and Photonics, 2012.
- [63] T. Mungle, S. Tewary, et al., "Automated characterization and counting of Ki-67 protein for breast cancer prognosis: A quantitative immunohistochemistry approach," *Computer Methods and Programs in Biomedicine*, vol. 139, pp. 149-161, 2017.
- [64] S. Monjoy, C. Chakraborty et. Al., "An Advanced Deep Learning Approach for Ki-67-Stained Hotspot Detection and Proliferation Rate Scoring for Prognostic Evaluation of Breast Cancer" *Scientific Reports* vol. 7, 2017.
- [65] D. Ciresan, A. Giusti, L. Gambardella, and J. Schmidhuber "Deep neural networks segment neuronal membranes in electron microscopy images", *NIPS*, pp. 2852–2860, 2012.
- [66] J. Long, E. Shelhamer, and T. Darrell, "Fully convolutional networks for semantic segmentation," in *CVPR*, pp. 3431–3440, 2015.
- [67] V. Badrinarayanan, A. Kendall, R. Cipolla. "Segnet: A Deep Convolutional Encoder-Decoder Architecture for Image Segmentation." *arXiv. Preprint arXiv: 1511.0051*, 2015.
- [68] International Agency for Research on Cancer, "World Cancer Report 2014" World Health Organization, Geneva, Switzerland. Chapter 2.8. pp. 146-147, 2014.
- [69] American Cancer Society "Cancer Facts and Figures 2017" [Online]. Available: <http://www.cancer.org/acs/groups/content/@editorial/documents/document/acspc-048738.pdf>. Accessed on: May 31, 2018.

- [70] S. Petushi, F. Garcia, M. Haber, C. Katsinis, A. Tozeren, "Large-scale computations on histology images reveal grade-differentiating parameters for breast cancer," *BMC Med. Imaging*, vol. 6 no.14, pp. 1-11, 2006.
- [71] H. Wu, J. Phan, A. Bhatia, B. Shehata, M. Wang "Detection of blur artifacts in histopathological whole-slide images of endomyocardial biopsies" in *Proc. 37th Annual International Conference of the IEEE Engineering in Medicine and Biology Society* (2015), Milan, Italy, pp. 727-730.
- [72] S. Kothari, J. Phan, and M. Wang "Eliminating tissue-fold artifacts in histopathological whole-slide images for improved image-based prediction of cancer grade" *Journal of Pathology Informatic*, 4.22, 2013.
- [73] S. Steger, D. Ebert and M. Erdt, "Lymph node segmentation in CT slices using dynamic programming," 2011 IEEE International Symposium on Biomedical Imaging: From Nano to Macro, Chicago, IL, pp. 1990-1993, 2011.
- [74] Y. Zhang, M. T. C. Ying, L. Yang, A. T. Ahuja and D. Z. Chen, "Coarse-to-Fine Stacked Fully Convolutional Nets for lymph node segmentation in ultrasound images," 2016 IEEE International Conference on Bioinformatics and Biomedicine (BIBM), Shenzhen, pp. 443-448, 2016.
- [75] A. Bánkfalvi "Comparative methodological analysis of erbB-2/HER-2 gene dosage, chromosomal copy number and protein overexpression in breast carcinoma tissues for diagnostic use". *Histopathology*, vol. 37, no. 5, pp. 411-419, November 2000.
- [76] H. Alturkistani, F. Tashkandi, and Z. Mohammed, "Histological stains: A literature review and case study," *Global Journal of Health Science*, vol. 8, no. 3, pp. 72-79, 2016.
- [77] C. Xu and J. Prince, "Snakes, shapes, and gradient vector flow," *IEEE Transactions on image processing*, vol. 7, no. 3, pp. 359-369, 1998.
- [78] R. L. Siegel, K. D. Miller, A. Jemal, 2020. *Cancer Statistics, 2020*. CA: A Cancer Journal for Clinicians, vol. 70, No. 1, pp.7–30, Jan/Feb 2020.
- [79] M. Reid, P. Bagci, N. Ohike, B. Saka, et al., 2015. Calculation of the Ki67 index in pancreatic neuroendocrine tumors: a comparative analysis of four counting methodologies. *Modern Pathology*, vol. 28, pp. 686–694, 2015.
- [80] S. Alheejawi, H. Xu, M. Mandal, "Novel lymph node segmentation and proliferation index measurement for skin melanoma biopsy images" submitted to *Computerized Medical Imaging and Graphics CMIG*, 2018.



- [81] O. Ronneberger, P. Fischer, T. Brox, 2015. U-Net: Convolutional Networks for Biomedical Image Segmentation. International Conference on Medical Image Computing and Computer-Assisted Intervention (MICCAI). Vol. 9351, pp. 234–241, Munich, Germany, Oct 5-9.
- [82] L. C. Chen et al., 2018. DeepLab: Semantic image segmentation with deep convolutional nets, atrous convolution and fully connected CRFs. *IEEE Trans. on Pattern Analysis and Machine Intelligence*, Vol. 40, Issue 4, pp. 834-848.
- [83] H. Kaiming, X. Zhang, S. Ren, J. Sun, 2016. Deep residual learning for image recognition. *IEEE conference on Computer Vision and Pattern Recognition (CVPR)*, pp. 770-778, Las Vegas, USA, June 27-30.
- [84] M. Saha, C. Chakraborty I. Arun, R. Ahmed, S. Chatterjee, 2017. An Advanced Deep Learning Approach for Ki-67-Stained Hotspot Detection and Proliferation Rate Scoring for Prognostic Evaluation of Breast Cancer. *Scientific Reports*, Vol. 7, Article number: 3213.
- [85] S. Alheejawi, R. Berendt, N. Jha, M. Mandal, 2019. Automated Melanoma Staging in Lymph Node Biopsy Image Using Deep Learning. *32nd IEEE Canadian Conference on Electrical and Computer Engineering (CCECE)*, Edmonton, Canada, May 6-8.
- [86] V. Nair, G. E. Hinton, 2010. Rectified linear units improve restricted Boltzmann machines,” 27th International Conference on Machine Learning (ICML), pp. 807–814, Haifa, Israel, June 21-24.
- [87] A. Krizhevsky, I. Sutskever, G. Hinton, 2012. Image net classification with deep convolutional neural networks,” *Advances in Neural Information Processing Systems (NIPS)*, pp. 1097–1105, Lake Tahoe, Nevada, USA, Dec 3-6.
- [88] X. Glorot, A. Bordes, Y. Bengio, 2011. Deep sparse rectifier neural networks. 14th International Conference on Artificial Intelligence and Statistics, pp. 315–323, Ft. Lauderdale, Florida, USA, April 11-13.
- [89] J. Shijie, W. Ping, J. Peiyi, H. Siping, 2017. Research on data augmentation for image classification based on convolution neural networks. 2017 Chinese Automation Congress (CAC), pp. 4165-4170, Jinan, China, Oct 20-22.
- [90] C. Robert, “Machine learning, a probabilistic perspective,” *CHANCE*, vol. 27, no. 2, pp. 62–63, 2014. (Book review) Kevin P. Murphy, *Machine Learning, a Probabilistic Perspective*, MIT Press, 2012.
- [91] L. Rebecca Siegel, D. Kimberly Miller and Ahmedin Jemal, (2020), "Cancer Statistics, 2020," *CA: A Cancer Journal for Clinicians*, vol. 70, No. 1, pp.7–30.

- [92] L. Brochez, E. Verhaeghe, and E. Grosshans, (2002), "Inter-observer variation in the histopathological diagnosis of clinically suspicious pigmented skin lesions". *J. Pathol.* 196(4), pp.459–466.
- [93] J. M. Haggerty, X. N. Wang, A. Dickinson, C. Malley, and E. B. Martin, (2014), "Segmentation of epidermal tissue with histopathological damage in images of haematoxylin and eosin-stained human skin". *BMC Med. Imaging.* 14(1), pp. 7.
- [94] J. Cheng, J. C. Rajapakse, (2009), "Segmentation of clustered nuclei with shape markers and marking function," *IEEE Transactions on Biomedical Engineering*, vol. 56, no. 3, pp. 741–748.
- [95] B. Parvin, Q. Yang, J. Han, H. Chang, B. Rydberg, and M. Helen (2007), "Iterative voting for inference of structural saliency and characterization of subcellular events," *IEEE Transactions on Image Processing*, vol. 16, no. 3, pp. 615–623.
- [96] H. Xu, C. Lu, R. Berendt, N. Jha and M. Mandal, (2017), "Automatic nuclei detection based on generalized Laplacian of Gaussian filters," *IEEE Journal of Biomedical and Health Informatics (JBHI)*, vol.21, no.3, pp.826-837.
- [97] D. Eigen, and R. Fergus, (2015) "Predicting depth, surface normals and semantic labels with a common multi-scale convolutional architecture", in *Proceedings of the International Conference on Computer Vision*, pp. 2650–2658.
- [98] S. Ioffe, and C. Szegedy, (2015), "Batch normalization: accelerating deep network training by reducing internal covariate shift," *arXiv preprint arXiv:1502.03167*.
- [99] C. Lu, M. Mahmood, N. Jha, Mandal M. A robust automatic nuclei segmentation technique for quantitative histopathological image analysis. *Anal Quant Cytopathol Histopathol.* 2012 Dec;34(6):296-308.
- [100] C. Lu, M. Mahmood, N. Jha, M. Mandal. "Detection of Melanocytes in Skin Histopathological Images using Radial Line Scanning", *Pattern Recognition*. Volume 46, Issue 2, February 2013, P. 509-518.
- [101] C. Lu and M. Mandal. 2015. Automated analysis and diagnosis of skin melanoma on whole slide histopathological images. *Pattern Recogn.* 48, 8 (August 2015), 2738–2750.
- [102] H. Xu, C. Lu, R. Berendt, N. Jha and M. Mandal, "Automatic Nuclear Segmentation Using Multi-Scale Radial Line Scanning with Dynamic Programming", *IEEE Transactions on Biomedical Engineering*, vol. 64, no. 10, pp. 2475-2485, Oct 2017.

- [103] S. Alheejawi, Richard Berendt, Naresh Jha & Mrinal Mandal, “Melanoma Cell Detection in Lymph Nodes Histopathological Images using Deep Learning” (2020). *Signal & Image Processing: An International Journal (SIPIJ)* Vol.11, No.4, August 2020.
- [104] P. Sabol, P. Sinčák, P. Hartono, P. Kočan, Z. Benetinová, A. Blichárová, L. Verbóová, E. Štammová, A. Sabolová-Fabianová, A. Jašková, “Explainable classifier for improving the accountability in decision-making for colorectal cancer diagnosis from histopathological images”, *Journal of Biomedical Informatics*, Volume 109, 2020, 103523.
- [105] M. Gadermayr, A. Dombrowski, B. Klinkhammer, P. Boor, D. Merhof, “CNN cascades for segmenting sparse objects in gigapixel whole slide images”, *Computerized Medical Imaging and Graphics*, Volume 71, 2019, Pages 40-48.
- [106] H.O. Alsaab, S. Sau, and R. Alzhrani “Pd-1 and pd-l1 checkpoint signaling inhibition for cancer immunotherapy: Mechanism, combinations, and clinical outcome”. *Front Pharmacol* 2017;8;561.
- [107] S.L. Topalian, C.G. Drake, and D.M. Pardoll “Immune checkpoint blockade: A common denominator approach to cancer therapy”. *Cancer Cell* 2015;27;450-461.

# Appendix A

## A.1 Dataset used in Chapter 3

Figure A.1 shows the dataset used in Chapter 3. In this study, 10 pairs of histopathological images obtained using MART-1 and Ki-67 stains were collected from the Cross-Cancer Institute, University of Alberta, Canada in accordance with the protocol for the examination of patients with melanoma cancer. The histopathological slides were digitized under 40X magnification using aperio scanscope slide scanner. The obtained WSIs are with size around 60,000×31,000 pixels (0.25  $\mu\text{m}$ /pixel resolution) and each WSI contains several lymph nodes. Each of these lymph nodes typically contain 2-4 melanoma regions.

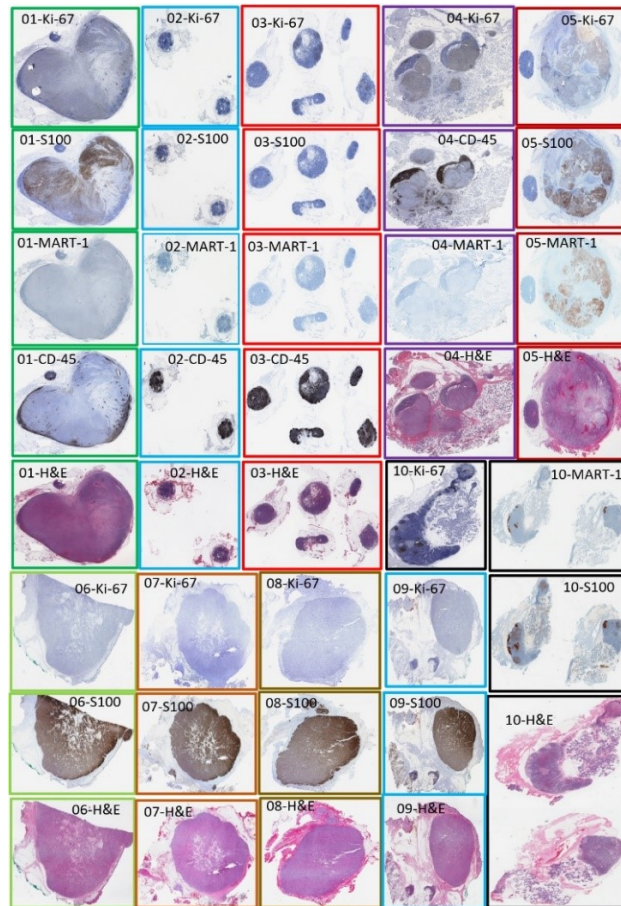


Figure A.1. Lymph node histopathological tissue image dataset. A total of 39 SLN images from 10 tissue sections (from 10 patients). Note that the WSI images with same color contour belong to the same lymph node tissue, but consecutive sections, stained with different stains (H&E, MART-1, Ki-67, CD-45, and S100).

## A.2 Dataset used in Chapter 4

In this study, 10 pairs of histopathological images obtained using MART-1 and Ki-67 stains were used. The images are a subset of images described in Appendix A.1. Each of the lymph nodes typically contain 2-4 melanoma regions. A total of 70 ROI (Region of Interest) windows with size  $1280 \times 704$  pixels (in Ki-67 images) are cropped from the lymph nodes of the 10 Ki-67 images (from both tumor and non-tumor regions) and are used as the training and testing sets. These ROI images are shown in Fig. A.3. The melanoma and non-melanoma regions in the Ki-67 images are determined by using the corresponding MART-1 images. Note that each window contains a large number of cell nuclei (active and passive cells).

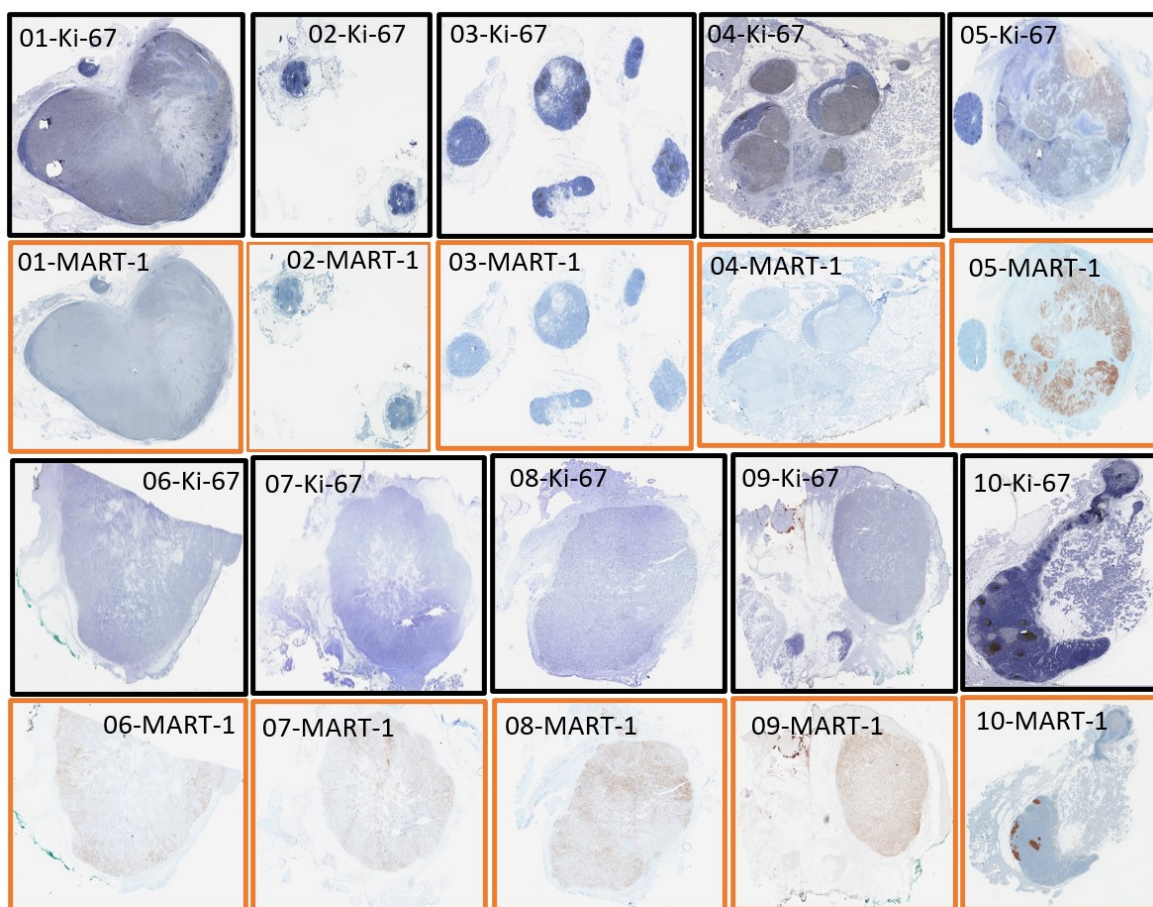


Figure A.2. Ten pairs of Histopathological Images obtained using the MART-1 and Ki-67 stains.



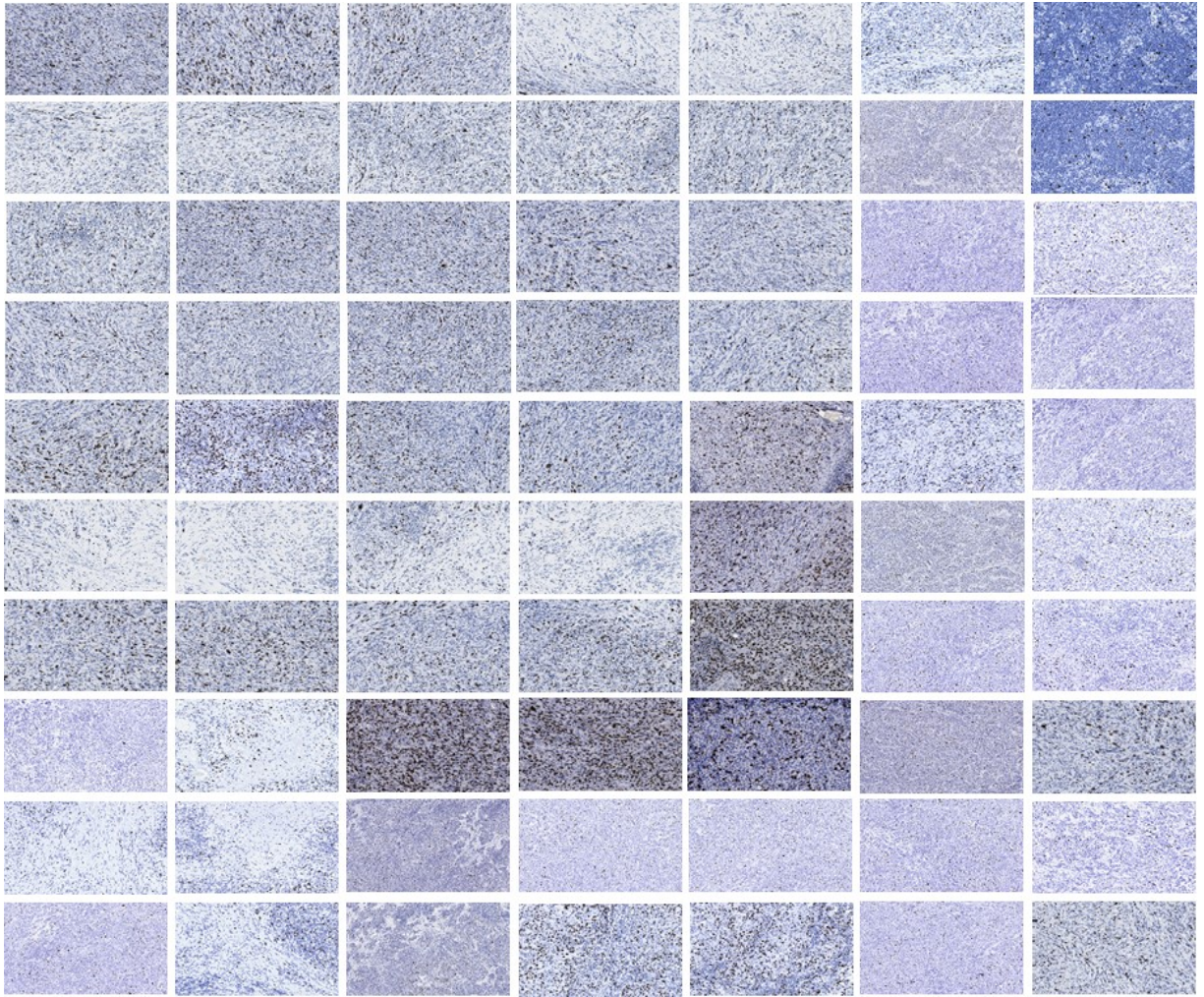


Figure A.3. Seventy ROI windows, each with size 704x1280 pixels, used for the PI calculation. Note that the seven images in a row belong to the same patient.

### A.3 Datasets used in Chapter 5 and Chapter 6

In this study, 4 pairs of whole slide histopathological images, shown in Fig. A.3, obtained using MART-1 and H&E stains were used. These images MART -1 and H&E stains were collected from the Cross-Cancer Institute, University of Alberta, Canada in accordance with the protocol for the examination of patients with melanoma cancer. The histopathological slides were digitized under 40X magnification using Aperio scanscope slide scanner. The images are obtained from skin tissue slides and it been diagnosed with melanoma, which appears with brown regions in MART-1 slides. The goal of this study is to segment the melanoma regions in H&E-stained images. The ground truth melanoma regions in a H&E-stained image were generated from the corresponding sequential MART-1-stained image.

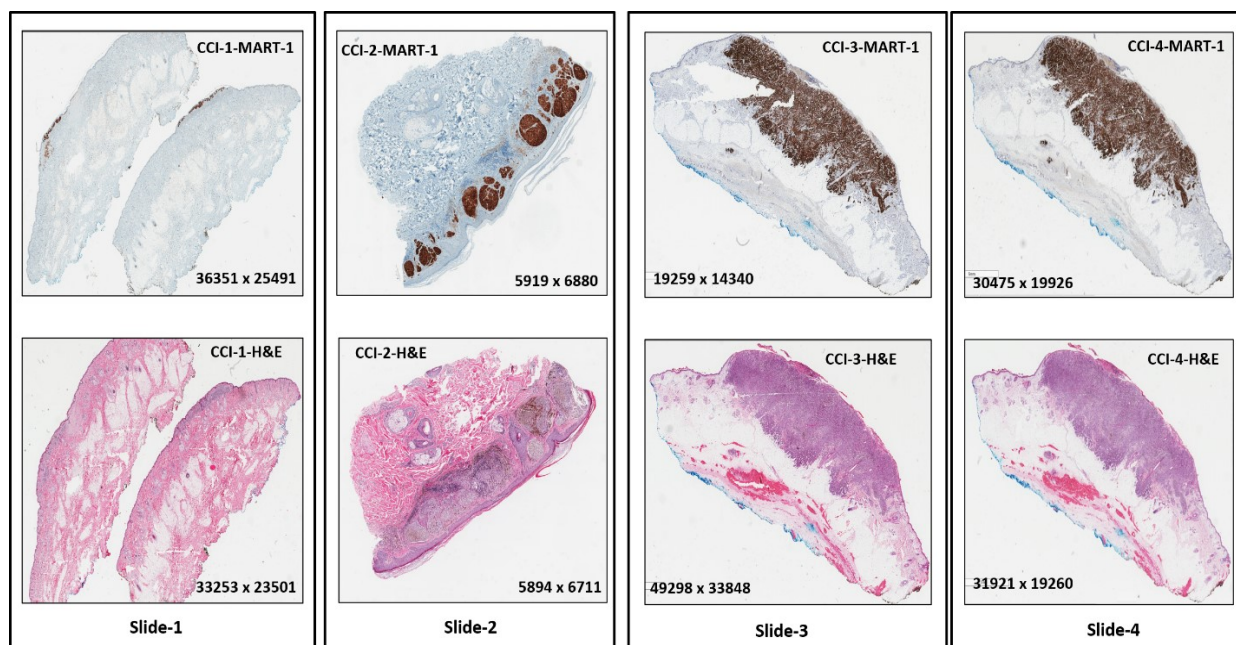


Figure A.4. Four pairs of Histopathological Images (WSI) with MART-1 and H&E stains.



## H&E Blocks with the corresponding MART-1 Blocks

Figure A.5 shows the extracted H&E blocks on the first row (inside a black rectangular contour) with corresponding MART-1 blocks on the second row and so on.

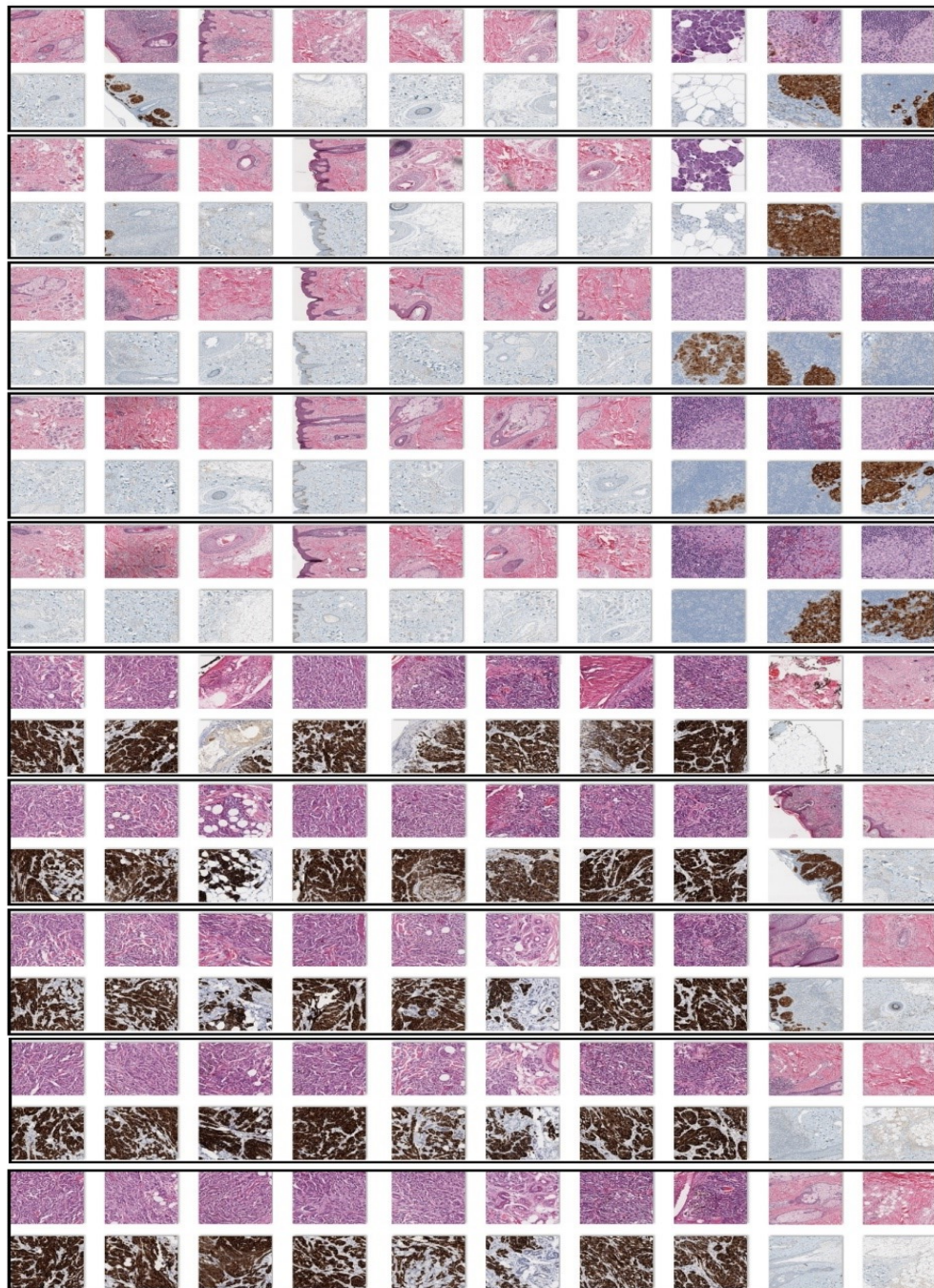


Figure A.5. Two hundred ROI windows, each with a size of 1000x1000 pixels, extracted from the four slides in Figure A.3. Note that the first row in each row-pair (inside a black rectangular contour) shows the H&E-stained blocks and the second row shows the corresponding MART-1 blocks.



## H&E Blocks with corresponding Nuclei Ground Truth Segmentation Masks

Figure A.6 shows the extracted H&E blocks on the first row with the corresponding nuclei ground truth segmentation masks on the second row (inside the black rectangular blocks).

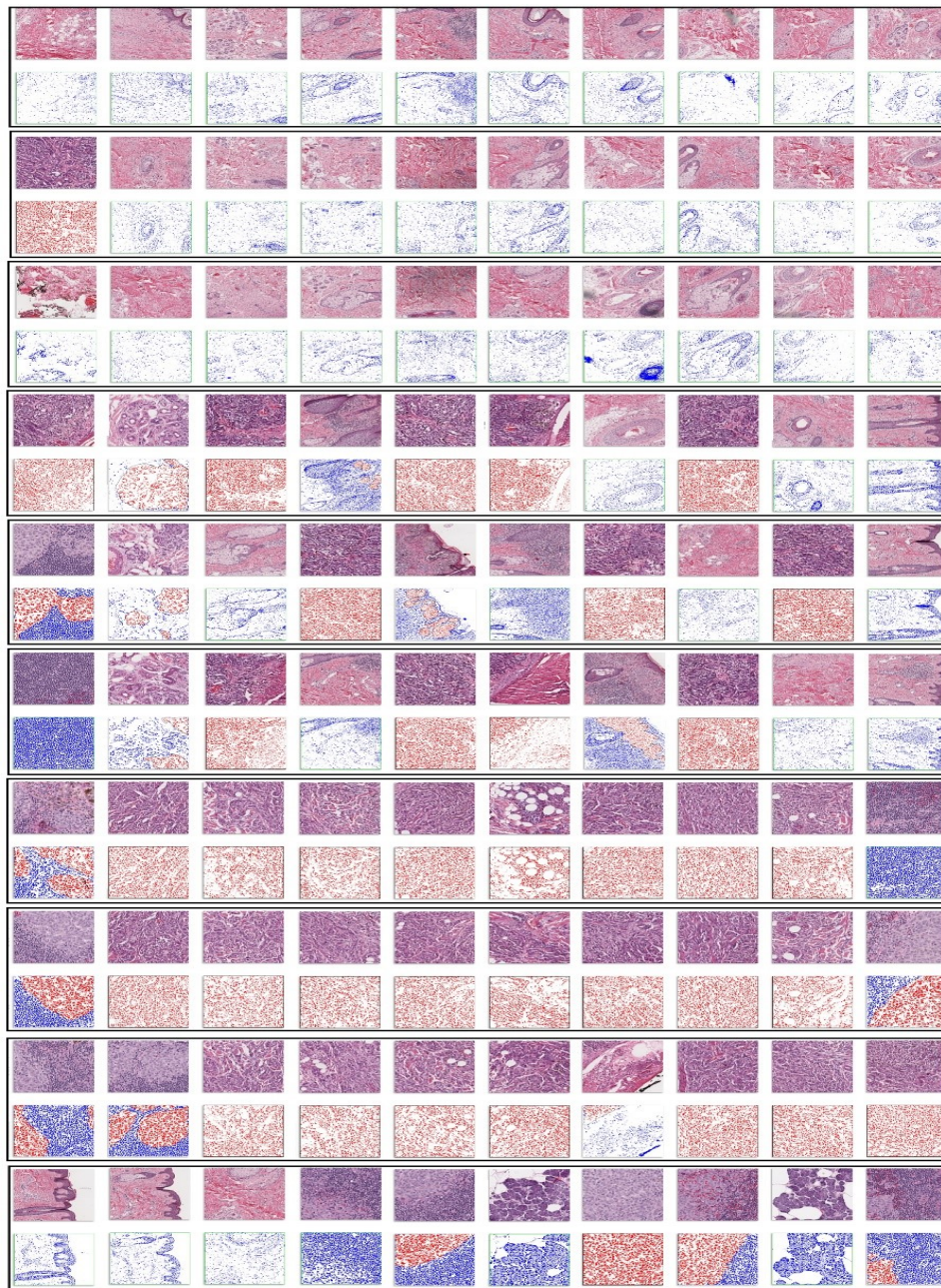


Figure A.6. The H&E-stained blocks in Fig. A.4 with the corresponding ground truth segmentation masks shown in the first and second rows (inside a black rectangular contour), respectively. Note that the melanoma nuclei, non-melanoma nuclei and background pixels are shown in red, blue, and white color, respectively.